

## Optics and Quantum Electronics

### Academic Staff

Prof. James G. Fujimoto, Prof. Erich P. Ippen, Professor Franz X. Kärtner

### Research Staff, Visiting Scientists and Affiliates

Dr. Guoqing Chang, Dr. Yueli Chen, Dr. Yu Chen, Prof. Helder Crespo, Dr. Carole Diederichs, Dr. Edilson Falcao-Filho, Dr. Peter Fendel, Dr. Vasileios Gkortsas, Dr. Iwona Gorczynska, Dr. Mikhail Gubin, Dr. Katherine Hall, Prof. T.W. Hansch, Dr. Kyung-Han Hong, Dr. R. Holzwarth, Dr. Robert Huber, Dr. Taegeun Kim, Dr. Florian Loehl, Dr. Frank Ludwig, Prof. Uwe Morgner, Dr. Jeffrey Moses, Dr. Amir Nejadmalayeri, Dr. David Phillips, Dr. Milos Popovic, Dr. Benjamin Potsaid, Dr. Dominik Pudo, Dr. Peter Rakich, Dr. Daniel Ripin, Dr. Luciano Socci, Dr. Hideyuki Sotobayoshi, Dr. Dimitri Tyurikov, Dr. Tobias Wilden, Prof. Ronald Walsworth, Prof. Zhigang Zhang, Dr. Guirong Zhou, Dr. Chao Zhou

### Graduate Students

Desmond Adler, Mohammed Araghchini, Andrew Benedick, Siddharth Bhardwaj, Jonathan Birge, Hyunil Byun, David Chao, Jeff Chen, Li-Jin Chen, Jung-Ho Chung, Giovanni Cirmi, Jonathan Cox, Marcus Dahlem, Umit Demirbas, Yu Gu, Shu-Wei Huang, Anatoly Khilo, Jung-Won Kim, Jonathan Liu, Jonathan Morse, Ali Motamedi, Michelle Sander, Hanfei Shen, Jason Sickler, Aleem Siddiqui, Vivek Srinivasan, Tsung-Han Tsai, Jade Wang

### Technical and Support Staff

Dorothy A. Fleischer, Donna L. Gale

## Research Areas and Projects

### Ultrashort Pulse Laser Technology

1. Sub-Two-Cycle Ti:Sapphire Laser with Nonintrusive Carrier Envelope Phase Stabilization Using Engineered Chirped Mirrors
2. Analysis and Stimulation of Systematic Errors in Spectral Shearing Interferometry of Single-Cycle Pulses
3. Robust Optimization of Dispersion Compensating Mirrors
4. Fundamentally Mode-locked 3GHz Femtosecond Erbium Fiber Laser
5. Low-cost and Highly Efficient Femtosecond Lasers
6. Multiphoton Microscopy Using a Low Cost Femtosecond Cr:LiCAF Laser

### Femtosecond Laser Frequency Combs, Optical Clocks and Phase Control

7. 2-GHz Octave-Spanning Ti:sapphire Laser
8. HeNe-CH<sub>4</sub> based Frequency Combs and Clocks using 1 GHz Repetition Rate Octave Spanning Ti:sapphire Lasers
9. Ti:Sapphire frequency Combs for High-Precision Radial Velocity Measurements in Astrophysics
10. Drift-Free Microwave Signal Synthesis from Mode-Locked Lasers with Sub-10 fs Residual Timing Jitter
11. Sub-10 femtosecond Precision, Long-term Stable Timing distribution Over Multiple Fiber Links
12. Optical Arbitrary Waveform Generation in the 1-2  $\mu\text{m}$  Wavelength Regime
13. A High Repetition Rate Fundamentally Modelocked Sigma Erbium Fiber Laser

### Ultrafast Phenomena and Quantum Electronics

14. Stable Mode-Locked Pulses from Mid-Infrared Quantum Cascade Lasers

## Chapter 32. Optics and Quantum Electronics

- 15. Ultrafast Nonlinear Optical Dynamics of High-power Slab-coupled Semiconductor Optical Waveguide Amplifiers
- 16. Femtosecond Laser Fabrication

### **Attosecond Science**

- 17. Broadband Optical Parametric Chirped Pulse Amplification
- 18. Generation of High-Average-Power Picosecond Pulse Trains from Cryogenically-cooled Yb:YAG Amplifiers
- 19. High-Harmonic Generation with Long Wavelength Driver Pulses

### **Photonic Analog-to-Digital Conversion**

- 20. Photonic Analog to Digital Conversion
- 21. High-Resolution Timing Jitter Characterization of Mode-Locked Lasers
- 22. High-Resolution Photonic Downconverting Analog-to-Digital Converter
- 23. High-Speed, Broadband, Silicon Electro-Optic Dual Output Modulators
- 24. Accuracy of Photonic Analog to Digital Converters
- 25. Integrated, Low Jitter, 400 MHz Femtosecond Waveguide Laser

### **Nanophotonics**

- 26. Widely-Tunable Silicon Nanophotonic Circuits for Telecom Applications
- 27. Loop-Coupled Resonators Enabling Optimally Sharp, Dispersionless Optical Filters and "Slow-Light" Delay Times
- 28. Low-Loss Bloch Waves in Open Guided-Wave Structures for Efficient Nanophotonic Waveguide Crossings
- 29. Super-Collimation in a 2-D Silicon Rod-Based Photonic Crystal

### **Frequency Swept Lasers**

- 30. Frequency Swept Lasers and Fourier Domain Mode Locking (FDML)

### **Publications, Presentations, Thesis and Books**

## Sub-Two-Cycle Ti:Sapphire Laser with Nonintrusive Carrier Envelope Phase Stabilization Using Engineered Chirped Mirrors

### Sponsors

Air Force Office of Scientific Research (AFOSR) FA9550-07-1-0014

Office of Naval Research (ONR) N00014-02-1-0717

National Science Foundation ECS-0501478

### Project Staff

Jonathan R. Birge, Prof. Helder M. Crespo, E. L. Falcao-Filho, Andrew Benedick, Michelle Sander, and Prof. Franz X. Kärtner

Nonlinear f-to-2f interferometry [1] is a well established technique for carrier-envelope phase (CEP) locking of ultrashort pulse lasers. The nonlinear nature of the process requires significant optical power, and a significant portion of the laser output is typically dedicated to the interferometer so as to achieve sufficient signal to noise of the RF beat signal. While this method allows for extremely stable CEP-locking, previously resulting in jitters below 40 attoseconds, it comes at the expense of sacrificing a significant portion of the useful output of the laser.

We have developed a solution to this problem by designing specially optimized [2] double-chirped mirrors that directly out-couple just those wavelengths used in the f-to-2f scheme. We demonstrate the use of these mirrors in a ring laser. In Figure 1(a), a schematic of the demonstration ring laser [3], mirror M3 has a reflectivity profile that allows bands centered at 1140 and 570 nm to pass through at half the intracavity power, with little dispersion. These wavelengths are sent directly into a standard f-to-2f interferometer for CEP-locking [4]. The phase stabilized pulse train is output to another port using a near-Brewster angle 2% output coupler created by a multilayer coating on a fused silica wedge (OC). The full output power from the laser is available for experimental use.

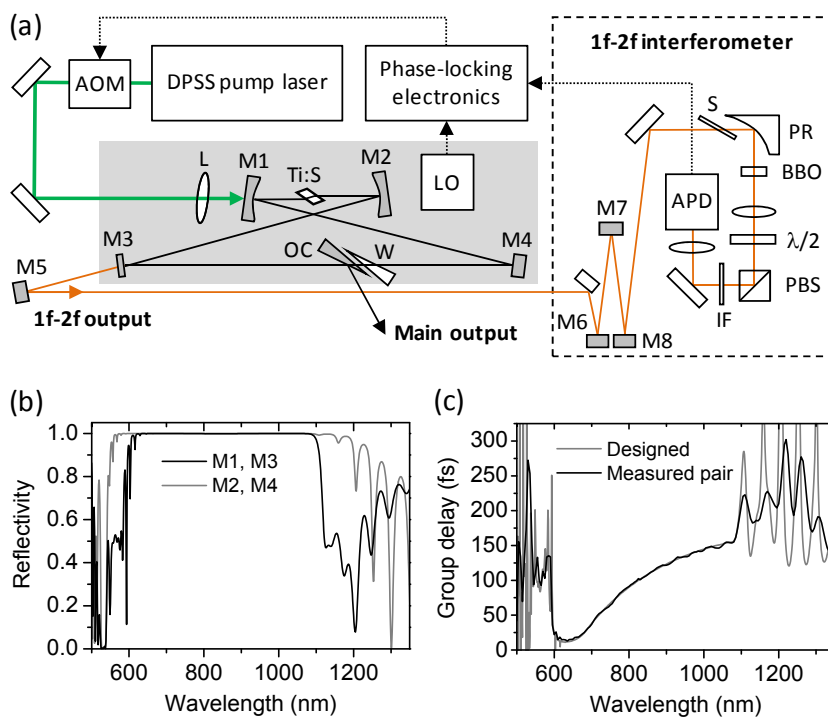


**Fig. 1.** (a) Schematic of ring laser and f-2f interferometer. (b) Theoretical reflectivity of double chirped mirror pair. (c) Measured and theoretical spectral group delay of DCM pair.

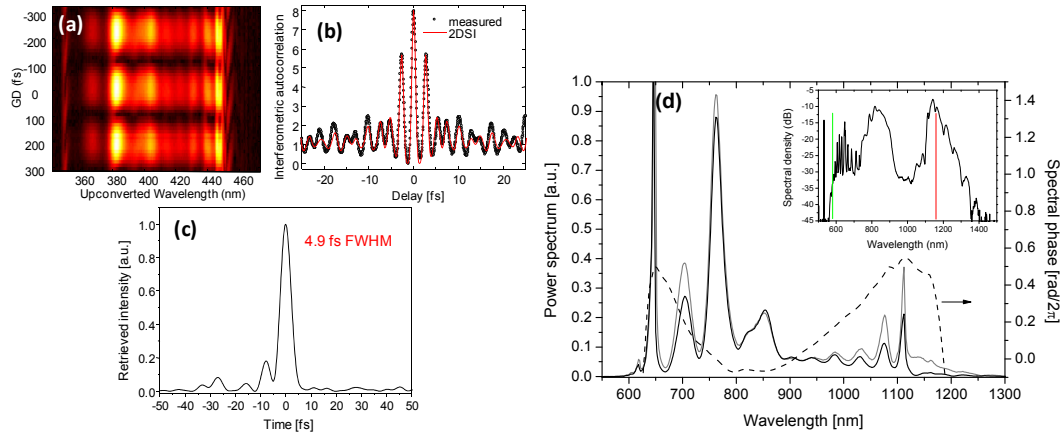


**Fig. 2.** (a) Raw 2DSI interferogram. (b) Measured and retrieved interferometric autocorrelations. (c) Recovered pulse intensity in the time domain. (d) Power spectral density of laser output, with extracted spectral phase overlaid.

Mode-locking is self-starting and unidirectional, and the laser generates 0.35–0.65W (depending on intracavity dispersion) when pumped with 6.5W from a DPSS laser, with an output spectrum exceeding an octave as measured on a linear scale (see Fig. 2). The oscillations in the spectrum match the residual oscillations in the GD of the double-chirped mirror pairs, as measured by a home-built white light interferometer (Fig. 1c). The oscillations are due to manufacturing errors, and will be improved in future coating runs. Second-harmonic generation in the BBO crystal generates an  $f$ - $2f$  beat signal with  $\sim 50$  dB SNR measured in a 100 kHz bandwidth directly from the avalanche photodiode output.

To confirm the generation of sub-two-cycle pulses, the pulses were characterized using both broadband SHG interferometric autocorrelation (IAC) and two-dimensional spectral shearing interferometry (2DSI) [5], which yielded the trace given in Fig. 2a. The retrieved spectral phase is shown in Fig. 2d. The measured and retrieved IAC traces (Fig. 2c) exhibit very good agreement, lending credence to the measurement. The retrieved sub-two-cycle pulse (Fig. 2b) has a FWHM duration of 4.9 femtoseconds.

To estimate the phase jitter of the CEP lock, an in-loop noise measurement was performed, the results of which are shown in Fig. 4. A relatively large source of phase noise turned out to be 60 Hz interference (and its harmonics) from the power supply. The total error (including the interference) integrated from 10 KHz to 10 MHz yields a timing jitter of only 33 attoseconds.

## References

- [1] L. Xu, C. Spielmann, A. Poppe, T. Brabec, F. Krausz, and T. W. Hansch, "Route to phase control of ultrashort light pulses," *Opt. Lett.* 21(24): 2008-2010 (1996).
- [2] H. M. Crespo, J. R. Birge, E. L. Falcão-Filho, M. Y. Sander, A. Benedick, and F. X. Kärtner, "Nonintrusive phase stabilization of sub-two-cycle pulses from a prismless octave-spanning Ti:sapphire laser," *Opt. Lett.* 33(8): 833-835 (2008).
- [3] J. R. Birge and F. X. Kärtner, "Efficient optimization of multilayer coatings for ultrafast optics using analytic gradients of dispersion," *Appl. Opt.* 46(14): 2656-2662 (2007).
- [4] O. Mücke, R. Ell, A. Winter, J. -W. Kim, J. Birge, L. Matos, and F. Kärtner, "Self-Referenced 200 MHz Octave-Spanning Ti:Sapphire Laser with 50 Attosecond Carrier-Envelope Phase Jitter," *Opt. Express* 13(13): 5163-5169 (2005).
- [5] J. R. Birge, R. Ell, and F. X. Kärtner, "Two-dimensional spectral shearing interferometry for few-cycle pulse characterization," *Opt. Lett.* 31(13): 2063-2065 (2006).

## Analysis and Simulation of Systematic Errors in Spectral Shearing Interferometry of Single-Cycle Pulses

### Sponsors

Office of Naval Research (ONR) N00014-02-1-0717  
National Science Foundation ECS-0501478

### Project Staff

Jonathan R. Birge and Prof. Franz X. Kärtner

As few- and single-cycle optical pulses have become more common, SPIDER [1] has emerged as a preferred method for determining the phase of such pulses [2]. However, there are a few issues with SPIDER that occur when dealing with such large bandwidths. First, the delay  $\tau$  between the pulse copies must be calibrated and maintained to within superinterferometric precision: in any spectral interferometry, the pulse width error for a given delay error  $\delta\tau$  is approximately

$$\delta t \approx \delta\tau \left( \frac{\Delta\omega}{\Omega} \right) \quad (1)$$

where  $\Delta\omega$  is the pulse bandwidth and  $\Omega$  is the shear [3]. For a single-cycle pulse, the term within parenthesis is typically between 10 and 100 and thus the delay  $\tau$  must be known to within 3–30 attoseconds to achieve 10% accuracy in the measured pulse width. Such calibration accuracy is difficult for delays on the order of picoseconds as it requires frequency determination on the order of one part in 100,000. Furthermore, it implies mechanical stability requirements of roughly 1–10 nanometers from calibration to measurement. This is difficult to achieve given inevitable changes in beam alignment during calibration or subsequent optimization. Starting with perfect alignment 30 attoseconds of delay will be introduced with only 6 milliradians of beam deviation. Unfortunately, there is no self-consistency check available in SPIDER, so any error in  $\tau$  simply manifests as an additive quadratic phase, potentially resulting in underestimation of pulse width. In cases where SPIDER is used to iteratively optimize a laser, it is possible that small beam pointing changes during optimization or thermal shifts in the setup will lead to perturbation of  $\tau$ , yielding a false optimization, unless care is taken to recalibrate after every change.

We simulated the effects of a spurious delay  $\delta\tau$  on a standard SPIDER measurement of a sub-two-cycle pulse, using spectral data from a sub-two-cycle ring laser in our lab as characterized by Two-dimensional spectral Shearing Interferometry (2DSI) [4]. Using the spectral phase measured by 2DSI, we simulated the case where a standard SPIDER measurement shows a very slightly chirped pulse of 4.94 fs FWHM. This is nearly as compressed as can be achieved by bulk material compensation. We then computed what the actual pulse was assuming a worst-case interpulse delay error due to several lengths of extra path length. The envelopes were computed using a padded FFT of the complex spectrum, neglecting any carrier offset (since we are only interested in the pulse envelope). The pulse RMS width (over a 40 fs window) and the FWHM were computed. The resulting pulses are shown in Fig. 1.

Note that it only took an extra delay of 100 as (30 nm) to cause an error over 5%. Furthermore, this example was actually conservative in that the measured pulse was well compressed and thus the nonlinear relation of the FWHM width to dispersion helped; the same data also imply that had the actual pulse been 12.8 fs long, only 30 nm of spurious delay would've appeared to be only 5.25 fs long. The point here is that if spectral shearing is used to measure pulses that are intentionally chirped (as in the case of pulses used in coherent control or those precompensated for material dispersion) the measurement will be maximally sensitive, such that (1) is an accurate estimate.

In Fig. 2, we show the error as simulated for a range of delays between zero and 60 nanometers, and compare it with that predicted by (1), taking the  $1/e^2$  half width to be 138 THz (about half of

the full range of the measured spectrum). After enough dispersion, the FWHM behaves severely nonlinear as subpulses grow past 50%. As anticipated by the fact that this pulse is nearly transform limited, the linear scaling law overestimates the errors. However, the error is not large, and it is generally within a factor of two of the RMS width.

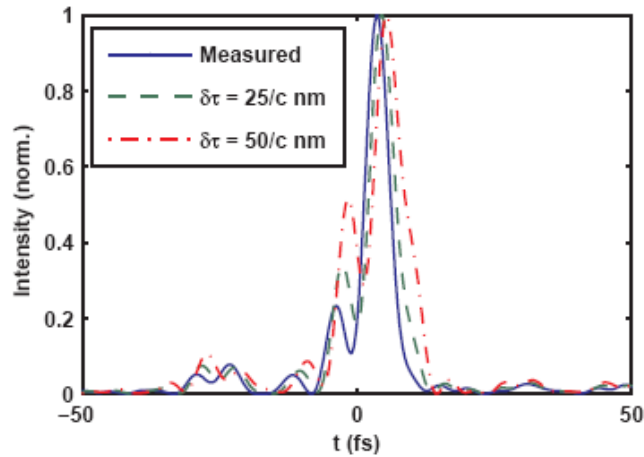


**Fig. 1.** Plot of simulated pulse envelopes as measured with a spectral shearing interferometer in the presence of varying amount of delay miscalibration.

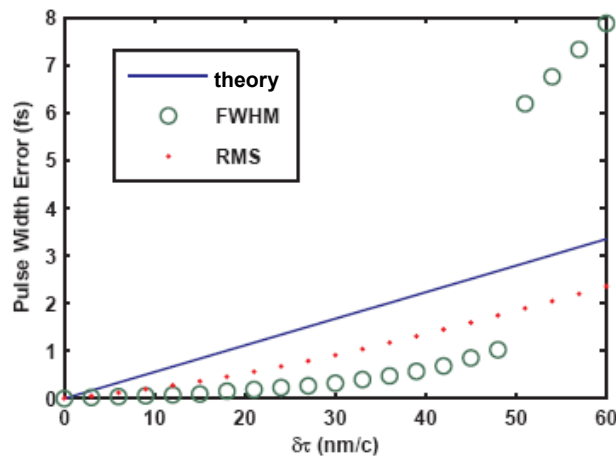


**Fig. 2.** Plot of simulated pulse width as delay miscalibration changes, as compared to our theoretical estimate (blue).

## References

- [1] C. Iaconis and I. Walmsley, "Self-referencing spectral interferometry for measuring ultrashort pulses," *IEEE JQE* 35(4), 501–509 (1999).
- [2] L. Gallmann, D. Sutter, N. Matuschek, G. Steinmeyer, and U. Keller, "Techniques for the characterization of sub-10-fs optical pulses: a comparison," *Appl. Phys. B* 70(S1), S67–S75 (2000).
- [3] J. R. Birge and F. X. Kärtner, "Analysis and mitigation of systematic errors in spectral shearing interferometry of pulses approaching the single-cycle limit," *J. Opt. Soc. Am. B* 25(6): A111-A119 (2008). Invited paper.
- [4] J. R. Birge, R. Ell, and F. X. Kärtner, "Two-dimensional spectral shearing interferometry for few-cycle pulse characterization," *Opt. Lett.* 31(13): 2063-2065 (2006).

## Robust Optimization of Dispersion Compensating Mirrors

### Sponsors

Office of Naval Research (ONR) N00014-02-1-0717  
National Science Foundation ECS-0501478

### Project Staff

Jonathan R. Birge, Dr. Omid Nohadani, Prof. Dimitris Bertsimas, and Prof. Franz X. Kärtner

The dispersion compensating mirror has become an enabling technology for modern ultrafast lasers. Solid-state mode-locked lasers can only operate at or below few-cycle pulse widths when the total cavity dispersion is reduced to nearly zero, with only a small amount (on the order of a few  $\text{fs}^2$ ) of residual second-order dispersion. In fact, pulse durations well below ten femtoseconds were not possible directly from oscillators until the development of high performance double-chirped mirror pairs [1].

Unfortunately, as bandwidths increase, so do the number of layers required to produce a stack with the high reflectivity needed for an intra-cavity mirror. For bandwidths exceeding an octave, mirror pairs with over 200 total layers are generally required. In practice the performance for such complicated mirrors is limited by the manufacturing tolerances of the mirrors. The sensitivity of a dielectric stack to manufacturing errors increases with the number of layers, and dispersion compensating mirrors push the limits of manufacturing tolerances, requiring layer precisions on the order of a nanometer. Currently, this challenges even the best manufacturers.

Despite the fact that manufacturing errors often limit the performance of thin-film devices, there has been little work on optimizing thin-film designs to mitigate the effects of errors. Some previous work in designing fault-tolerant mirrors has focused on optimizing first-order tolerances, a method readily available in commercial thin film design codes. Our approach to robust optimization probes the exact merit function in a bounded space of potential thickness errors, potentially taking into account features of the problem space not considered with local methods. The robustness is guaranteed to be equal or better than that obtained with nominal optimization. While our approach results in a much more computationally involved optimization, it is made feasible by the use of fast algorithms previously developed in our group [2].

Our approach is essentially a nonlinear minimax algorithm, consisting of two nested optimization loops: an inner maximization loop which finds the worst-case neighbor of a given mirror design, and an outer minimization which seeks to find the design with the lowest possible worst-case performance. Here, “neighbor” refers to a mirror configuration which is within a certain radius of our nominal design, as defined by our expected manufacturing tolerances. Once worst-case neighbors are identified, a direction is sought along which an updated neighborhood would not include these worst-case scenarios any longer. This direction is a vector that spans the largest angle to all worst implementation errors, Fig. 1.

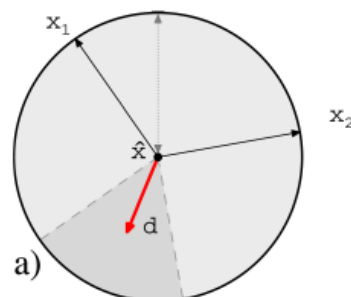


**Fig. 1.** Illustration of strategy for avoidance of worst-case neighbor by a movement in a direction which maximizes the angle to a set of “bad” neighbors.

To protect a design against errors, it is helpful to utilize available understanding of possible errors. For example, if there are worst-case scenarios in the respective neighborhood that are very rare according to our assumed layer perturbation distribution, there is no need for them to be considered during the inner maximization problem. By excluding these rare events, we are able to protect the design against realistic and statistically relevant errors only, without needlessly sacrificing nominal performance to guard against rare errors. Moreover, this approach leads to a reduction of the size of the respective search space and, thus, to an increase of the computational efficiency.

It is well known that the reflection coefficients of thin-film stacks are closely related to the Fourier transform of the layer thicknesses. Thus, one promising class of rare perturbations to eliminate from consideration is that in which there are strong correlations between the layers. These errors involve, for example, shifting of all the thicknesses in one direction, which results in a spectral shift regardless of the design. We will restrict ourselves to considering only statistically independent random perturbations to the layers, and thus restrict the maximum variation in the amplitude of the Fourier components of the error vector. A straightforward way to do this is to restrict the search to the class of error vectors with minimum coherence, requiring all Fourier components to have uniform amplitude.

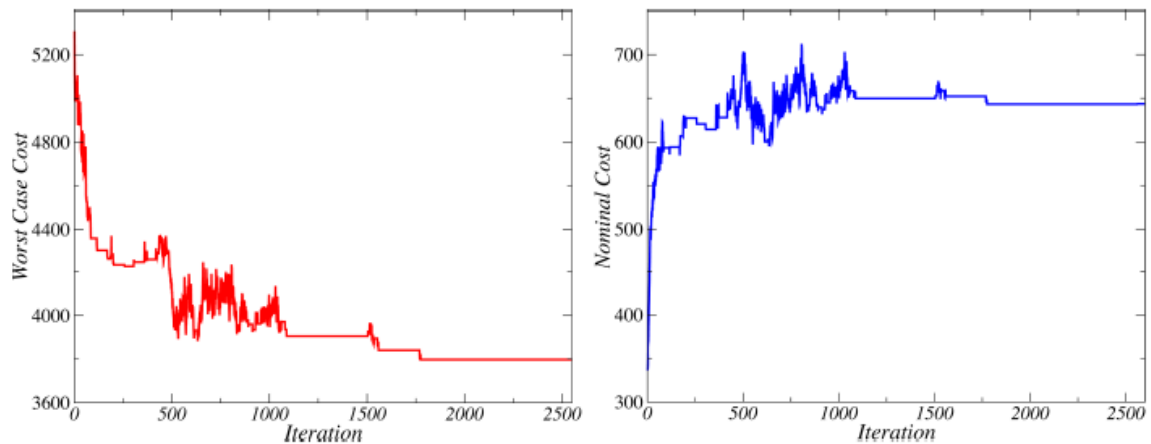


**Fig. 2.** (left) Worst case cost as a function of optimization iteration. (right) The nominal cost increases as the optimization progresses as the “price of robustness.”

We tested our robust optimization program [3] on the design of a 200 layer dispersion compensating mirror designed to provide compensation for a 5 fs mode-locked laser. Starting from a nominally optimized solution, our robust optimization algorithm successively decreased the worst-case cost, as shown in Fig. 2. The significant improvement of robustness comes at the price of a small increase in the nominal cost, however, as illustrated in the adjacent plot. The algorithm converges to the robust local minimum, at which point no descent direction can be found.

## References

- [1] F. X. Kärtner, U. Morgner, R. Ell, T. Schibli, J. G. Fujimoto, E. P. Ippen, V. Scheuer, G. Angelow, and T. Tschudi, "Ultrabroadband double-chirped mirror pairs for generation of octave spectra," *J. Opt. Soc. Am. B* 18(6): 882-885 (2001).
- [2] J. R. Birge and F. X. Kärtner, "Efficient optimization of multilayer coatings for ultrafast optics using analytic gradients of dispersion," *Appl. Opt.* 46(14): 2656-2662 (2007).
- [3] O. Nohadani, J. R. Birge, F. X. Kärtner, and D. J. Bertsimas, "Robust chirped mirrors," *Appl. Opt.* 47(14): 2630-2636 (2008).

## Fundamentally Mode-locked 3 GHz Femtosecond Erbium Fiber Laser

### Sponsors

Defence Advanced Research Projects Agency, DARPA HR0011-05-C-0155  
Air Force Office of Scientific Research and FA9550-07-1-0014

### Project Staff

Jian Chen, Jason Sickler, Hyunil Byun, Prof. Erich P. Ippen, and Prof. Franz X. Kärtner

Femtosecond sources with multi-gigahertz repetition rates at optical communications wavelengths are critical building blocks for numerous applications [1,2]. Currently, only a few approaches [3,4] meet the stringent requirements in terms of pulse duration, repetition rate, operating wavelength, and noise performance simultaneously. However, these current approaches are bulky, expensive, and of limited robustness, since they employ Fabry-Perot filters locked to the mode comb for multiplying the repetition rate to the multi-gigahertz range, either inside or outside of the low fundamental-repetition-rate laser cavities. A more simple, compact, robust and cost efficient approach is desirable. Lasers with fundamental repetition rates in the multi-gigahertz range are ideal candidates for some of the intended applications.

With the constraints of achieving femtosecond pulse duration, and low timing jitter, passive mode-locking is the only path to reach multi-gigahertz fundamental repetition rates. Record high repetition rates of a few hundred MHz have been reported previously [3,5]. However, those attempts failed to produce femtosecond pulses [6], which is of key importance for low jitter and for frequency metrology applications.

Here, we demonstrate, for the first time, a fundamentally mode-locked femtosecond erbium-doped fiber laser (EDFL) with a repetition rate of 3.2 GHz and a timing jitter of 19 fs [10kHz-40MHz]. This result exceeds previous attempts to increase the repetition rate of fiber lasers by about ten fold, and sets a clear pathway to achieving low timing jitter, mode-locked femtosecond sources at 1550 nm with up to ten GHz of repetition rate.

Saturable Bragg Reflector (SBR) mode-locking only results in femtosecond pulses when soliton pulse shaping [7] can be employed. In order to generate the shortest pulse duration with limited pulse energy the cavity dispersion needs to be minimized and the cavity nonlinearity needs to be maximized.

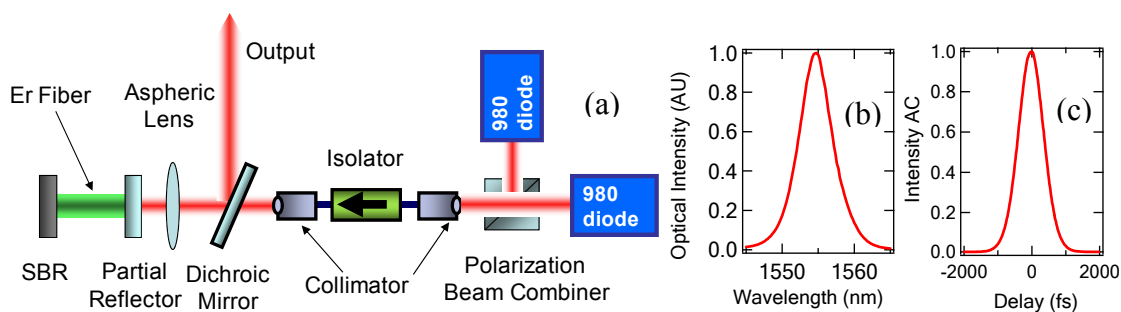


**Fig. 1.** (a) Experimental setup. (b) Optical spectrum of the pulse train. (c) Intensity autocorrelation measurement

The experimental setup is shown in Fig. 1 (a). Guided by simulation based on the above considerations, we choose a 3 cm-long highly doped erbium-ytterbium fiber (NP Photonics) with a group-velocity dispersion (GVD) of  $-60 \text{ fs}^2/\text{mm}$  and a nonlinear coefficient of  $\sim 3 \text{ (Wkm)}^{-1}$  as the gain medium. One end of the gain fiber is butt-coupled to an SBR, and the other to a 2% dielectric output coupler. We carefully choose the SBR so that the dispersion of the SBR is slightly positive with  $1000 \text{ fs}^2$  to compensate about half of the negative dispersion from the gain

fiber. The SBR also has a 6% modulation depth, a 2 ps recovery time, and a saturation fluence of  $25 \mu\text{J}/\text{cm}^2$ . Pump light is provided by two polarization combined 500 mW 980-nm-laser diodes, free-space coupled via an aspherical lens into the gain fiber through the output coupler. The output signal is separated from the pump light by a dichroic mirror.

The setup is simple, compact, and self-starting. When the laser is pumped with  $\sim 700$  mW of 980 nm pump power the mode-locked optical spectrum is 5.3 nm wide as shown in Fig. 1(b). Fig. 1(c) shows the intensity autocorrelation of the pulse train after amplification by an erbium-doped fiber amplifier resulting in a pulse duration of 600 fs, which was limited by dispersion compensation of the amplifier. Further compression to its transform-limited pulse duration of 500 fs is in progress. The average output power from the laser cavity is 2 mW and was used to seed a subsequent erbium doped fiber amplifier for applications demanding higher average power. The intracavity average power is calculated to be 100 mW yielding a pulse energy of 33 pJ. These numbers agree well with soliton theory and our simulations.

Figure 2(a) shows the measured RF signal using a 10 GHz photodetector; Figure 2(b) shows one of the RF comb lines measured with a 3 kHz resolution bandwidth indicating clean mode-locked operation with a background suppression better than 80 dB. Measurements of the timing jitter were carried out using an HP5052a signal source analyzer. Figure 2 (c) shows the single sideband phase noise measurement and the timing jitter progressively integrated from 40 MHz down to 1 kHz. The timing jitter integrated from 10 kHz to 40 MHz is 19 fs.

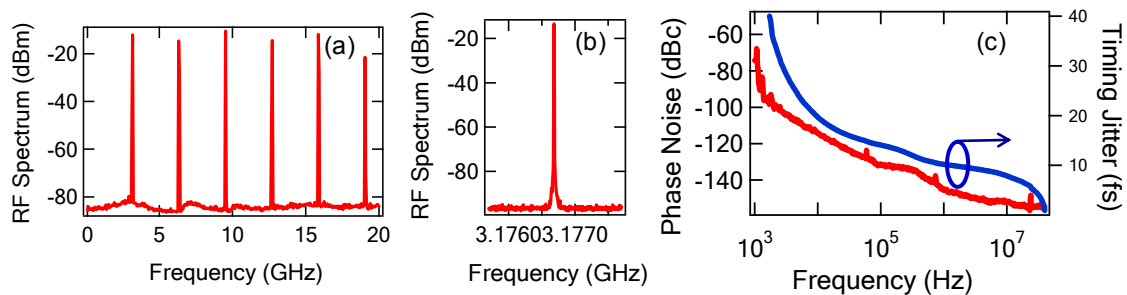


**Fig. 2.** (a) RF spectrum, span=20 GHz, (b) RF spectrum, span =2 MHz, RBW=3kHz, (c) Phase noise measurement, and integrated timing jitter starting from 40 MHz down to 1 kHz

We have demonstrated the first compact, multi-gigahertz, fundamentally mode-locked EDFL producing femtosecond-duration pulses with a low timing jitter of 19 fs [10kHz-40MHz] The laser design sets a clear pathway to achieve even shorter pulses and higher fundamental repetition rates beyond 10 GHz.

## References

- [1] S. T. Cundiff, *Nature*, vol. 450, pp. 1175-1176 (2007)
- [2] C-H. Li, A. Benedick, P. Fendel, A. G. Glenday, F. X. Kärtner, D. Phillips, D. Sasselov, A. Szentgyorgyi and R. Walsworth, *Nature* 452, 610-612 (2008)
- [3] J. Chen, J. Sickler, E.P.Ippen, and F.X. Kartner, *Optics Letters*, Vol. 33 (9), pp.959-961 (2008)
- [4] F. Quinlan, S. Gee, S. Ozharar, and P. J. Delfyett, *Optics Letters*, Vol. 31 Issue 19, pp.2870-2872 (2006)
- [5] T. Wilken, T.W. Hänsch, R. Holzwarth, P. Adel, M. Mei, in *Conference on Laser and Electro-Optics*. OSA, 2007.
- [6] J. J. McFerran, L. Nenadović, W. C. Swann, J. B. Schlager and N. R. Newbury, *Optics Express*, 15, 13155, (2007).
- [7] F. X. Kärtner and U. Keller, *Opt. Lett.* 20, 16-18, 1995.

## Low-cost and Highly Efficient Femtosecond Lasers

### Sponsors

National Science Foundation – ECS-0456928, ECS-0501478

Air Force Office of Scientific Research – FA-9550-07-1-0101 and FA9550-07-1-0014

Scientific and Technical Research Council of Turkey –104T247

### Project Staff

Umit Demirbas, Professor Alphan Sennaroglu, Professor Franz X. Kaertner, Professor James G. Fujimoto

$\text{Cr}^{3+}$ -doped colquiriites (Cr:LiSAF, Cr:LiCAF, Cr:LiSGAF) were first demonstrated as an important and versatile solid-state gain media in the late 80s [1]. These materials have attracted a great deal of attention because (i) they can be directly diode-pumped, (ii) they have broad emission bandwidths around 800 nm (enabling as short as  $\sim 10$ -fs pulse generation), and (iii) they have near-unity quantum efficiency to enable very efficient laser operation [1-8]. Although the Ti:Sapphire laser is the most commonly used laser system in femtosecond optics, it has the disadvantage of requiring expensive green lasers as the pump sources. Hence,  $\text{Cr}^{3+}$ -doped colquiriites are leading candidates for the development of low-cost femtosecond laser systems.

Here we will summarize our recent experimental results with Cr:LiCAF gain media both in continuous-wave (cw) and cw mode-locked operation. Our group used inexpensive multimode ( $\sim 1.5$ W,  $\sim \$1000$ ) or single-mode ( $\sim 150$  mW,  $\sim \$150$ ) laser diodes as pump sources, hence the overall material cost of the lasers was below  $\sim \$10$ k. With multimode diode pumping, cw output powers exceeding 1-W and mode-locked pulse energies as high as 2.8 nJ were obtained. Using single-mode diode pumping, up to 280-mW of cw output power with 54% slope efficiency, and continuous tuning between 765 and 865 nm were demonstrated. In cw mode-locking, 72-fs, 1.4-nJ pulses were obtained and a record electrical to optical conversion efficiency of 7.8% was demonstrated.

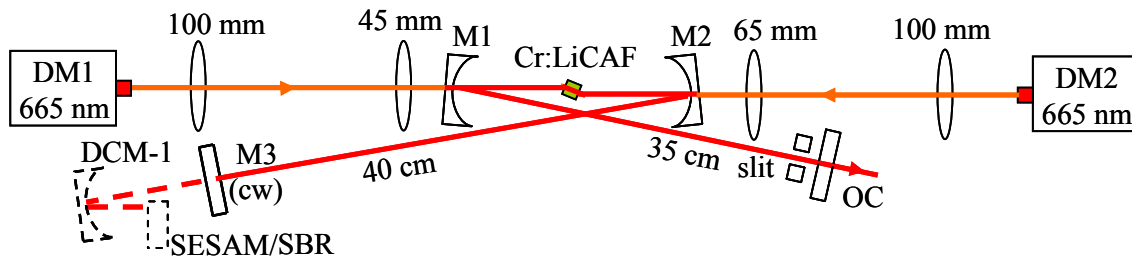
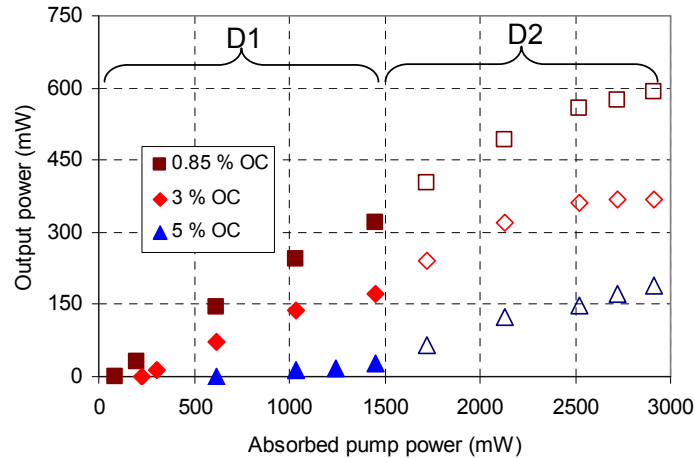


Figure 1. Schematic of the multimode diode-pumped  $\text{Cr}^{3+}$ :LiCAF laser.

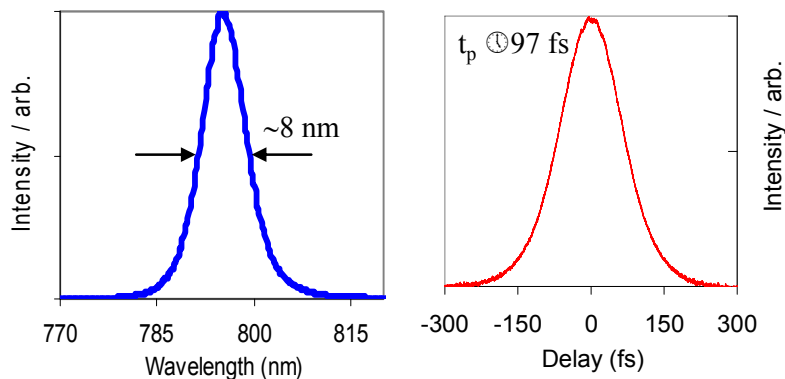
A schematic of the multimode diode pumped  $\text{Cr}^{3+}$ :LiCAF laser is shown in Figure 1. Two linearly-polarized, 1.6-W, single-emitter diodes (DM1-DM2) were used as the pump. Diode output was diffraction limited along the fast axis, and multimode along the slow axis with an  $M^2 \sim 10$ . The cw laser resonator was a simple x-folded cavity, consisting of two curved pump mirrors (M1 and M2), a flat highly reflecting end mirror (M3), and a flat output coupler (OC). A slit near the OC was used to control the transverse mode structure of the laser beam. For mode-locking experiments, a double-chirped mirror (DCM) was used to provide the necessary negative dispersion. A low-loss semiconductor saturable absorber mirror (SESAM, also known as a saturable Bragg reflector SBR) was used to initiate and sustain mode locking. The SESAM/SBR mode-locked laser was self-starting, immune to environmental fluctuations, did not require careful cavity alignment, and enabled turn-key operation.

Figure 2 shows the measured cw performance of the laser taken using different output couplers for multimode diode pumping. Using the 0.85 % output coupler we could get up to 590 mW of output power with a TEM<sub>00</sub> beam profile at a slope efficiency of 22 %. Output power saturation

was observed at high pumping levels (Figure 2) due to the strong thermal loading created by mode mismatch between the pump and the laser beams. Without the intracavity slit, using the 2 % output coupler, we could get as much as 1020 mW of cw output power with a corresponding slope efficiency of 30%; however, the laser output was multimode. This we believe is the highest obtained cw powers from a diode pumped Cr:LiCAF laser.



**Figure 2.** Measured cw efficiency curve for multimode diode-pumped Cr:LiCAF laser



**Figure 3.** Measured spectra and background-free intensity autocorrelation trace for multimode diode pumped cw mode-locked laser cavity.

Figure 3 summarizes the cw modelocking results for multimode diode pumping. The laser produced 97-fs pulses with 390 mW average power and 8 nm spectral bandwidth near 800 nm at 140 MHz ((2.8-nJ pulse energy). To our knowledge, obtained mode-locked average powers and pulse energies with the multimode diode pumped system are the highest demonstrated to date from a Cr:LiCAF laser. Also this is the highest modelocked average power ever achieved with diode pumped Cr:Colquirite lasers in a single beam configuration (although 500 mW were reported from a Cr:LiSAF laser, the power was split into two 250-mW beams).

Figure 4 shows a schematic of the single-mode diode pumped Cr:LiCAF laser cavity. Four AlGaInP single-mode diodes at ~660 nm, each costing only ~\$150, were used as the pump source (DS1-DS4). At a drive current of 220 mA (2.6 V), the diodes provided up to ~160-170 mW of output each. In total, at this maximum driving current (220 mA), the four diodes required ~2.3 W and produced ~660 mW of output power. The cw and cw mode-locked laser resonator was similar to what was described earlier for multimode diode pumping and same optical elements were used to ensure a consistent comparison.

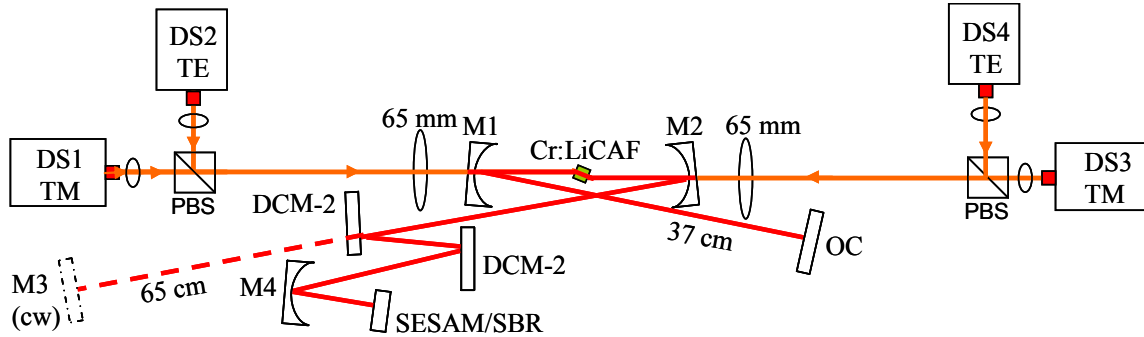


Figure 4. Schematic of the single-mode diode-pumped Cr<sup>3+</sup>:LiCAF laser.

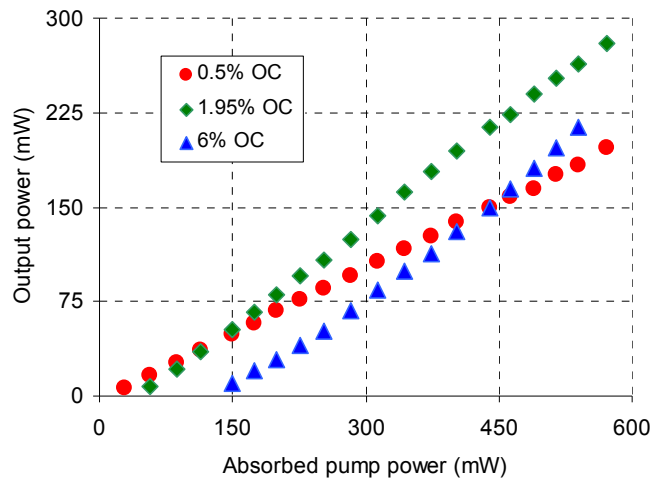
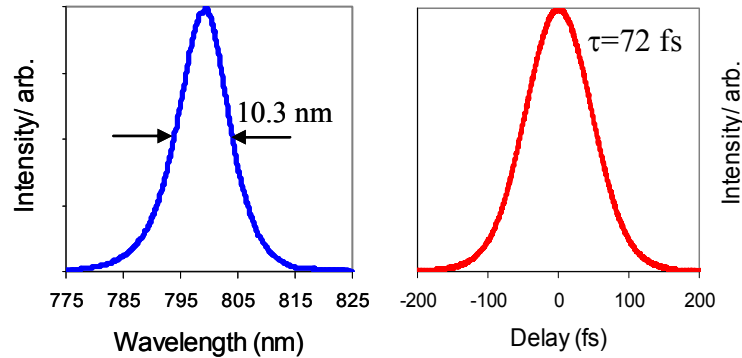


Figure 5. Cw efficiency curves taken with the single-mode diode-pumped Cr:LiCAF laser.

Figure 5 shows the cw laser efficiency curves taken using the 0.5, 1.95 and 6 % transmission output couplers with single-mode diode pumped cavity. Using the 1.95% output coupler, the laser produces up to 280 mW of output power with 570 mW of absorbed pump power, at a slope efficiency of ~54%. To our knowledge, this is the highest slope efficiency obtained from any diode pumped Cr:colquiriite laser to date [2]. Using the 0.5 % OC, lasing could be obtained with record low incident pump power levels of ~10 mW (corresponding absorbed pump power was ~9 mW). Using a fused silica prism as a dispersive element continuous and smooth tuning of laser wavelength between 765 and 865 nm was demonstrated. This, we believe, is the first demonstration of lasing above 840 nm for the Cr:LiCAF media [1].

When modelocked, the single-mode diode pumped Cr:LiCAF laser produces 72-fs pulses with 178 mW average power (~1.4-nJ pulse energy) and 10.3 nm spectral bandwidth near 800 nm at 127 MHz (Figure 6). To our knowledge, these are the highest average power and highest pulse energies obtained to date from single-mode diode-pumped Cr:colquiriite lasers. For the cw mode-locked operation, the optical to optical conversion efficiency was ~28% (178 mW / 660 mW), and

the electrical to optical conversion efficiency was  $\sim 7.8\%$  ( $178 \text{ mW} / 2.3 \text{ W}$ ). We believe this is the highest electrical to optical conversion efficiency obtained to date from any solid-state femtosecond laser system [3]. These results suggest that diode pumped Cr:LiCAF is emerging as a low cost, alternative technology to femtosecond Ti:Sapphire lasers.



**Figure 6.** Measured spectra and autocorrelation trace for the 72-fs, 1.4 nJ pulses with 178 mW of average output power, taken using the 1.9% OC.

The results obtained with Cr:LiCAF gain media have shown that Cr:LiCAF lasers could provide laser performance approaching Ti:Sapphire lasers in both cw and cw modelocked regime. We believe the single mode diode-pumped Cr:LiCAF laser system is especially promising because (i) it would significantly reduce the laser cost (the total cost of materials could be below  $\sim \$10\text{k}$  [10]), (ii) it would also be inexpensive to maintain [11], (iii) the system has record electrical-to-optical conversion efficiency and could be used in applications where minimal power consumption is critical, (iv) the laser could be made compact and portable (since the diodes and the laser crystal did not require water cooling and the diodes could be run by batteries [3, 12]), and (v) it could enable turn-key operation and would be suitable for use outside the research laboratory environment. Because of all these reasons, we believe that tunable cw and fs laser sources based on Cr:LiCAF gain media has the potential to replace the current expensive Ti:Sapphire technology in several areas of research and application.

## References

- [1] S. A. Payne, L. L. Chase, H. W. Newkirk, L. K. Smith, and W. F. Krupke, "Licaalf6-Cr-3+ - a Promising New Solid-State Laser Material," *Ieee Journal of Quantum Electronics*, vol. 24, pp. 2243-2252, Nov 1988.
- [2] A. Isemann and C. Fallnich, "High-Power Colquiriite Laser with high slope efficiencies pumped by broad-area laser diodes.," *Optics Express*, vol. 11, pp. 259-264, 2003.
- [3] B. Agate, B. Stormont, A. J. Kemp, C. T. A. Brown, U. Keller, and W. Sibbett, "Simplified cavity designs for efficient and compact femtosecond Cr:LiSAF lasers," *Optics Communications*, vol. 205, pp. 207-13, 2002.
- [4] U. Demirbas, A. Sennaroglu, A. Benedick, A. Siddiqui, F. X. Kartner, and J. G. Fujimoto, "Diode-pumped, high-average power femtosecond Cr<sup>+3</sup>:LiCAF laser," *Optics Letters*, vol. 32, pp. 3309-3311, 2007.

- [5] U. Demirbas, A. Sennaroglu, F. X. Kartner, and J. G. Fujimoto, "Highly efficient, low-cost femtosecond Cr<sup>3+</sup>:LiCAF laser pumped by single-mode diodes," *Optics Letters*, vol. 33, pp. 590-592, 2008.
- [6] P. Wagenblast, R. Ell, U. Morgner, F. Grawert, and F. X. Kartner, "Diode-pumped 10-fs Cr<sup>3+</sup>: LiCAF laser," *Optics Letters*, vol. 28, pp. 1713-1715, Sep 2003.
- [7] P. Wagenblast, U. Morgner, F. Grawert, V. Scheuer, G. Angelow, M. J. Lederer, and F. X. Kärtner, "Generation of sub-10-fs pulses from a Kerr-lens modelocked Cr<sup>3+</sup>:LiCAF laser oscillator using third order dispersion compensating double chirped mirrors," *Optics Letters*, vol. 27, pp. 1726-1729, 2002.
- [8] P. C. Wagenblast, T. H. Ko, J. G. Fujimoto, F. X. Kaertner, and U. Morgner, "Ultrahigh-resolution optical coherence tomography with a diode-pumped broadband Cr<sup>3+</sup>: LiCAF laser," *Optics Express*, vol. 12, pp. 3257-3263, Jul 12 2004.
- [9] D. Kopf, K. J. Weingarten, G. Zhang, M. Moser, M. A. Emanuel, R. J. Beach, J. A. Skidmore, and U. Keller, "High-average-power diode-pumped femtosecond Cr:LiSAF lasers," *Applied Physics B-Lasers and Optics*, vol. 65, pp. 235-243, Aug 1997.
- [10] J. M. Girkin and G. McConnell, "Advances in laser sources for confocal and multiphoton microscopy," *Microscopy Research and Technique*, vol. 67, pp. 8-14, May 2005.
- [11] D. L. Wokosin, V. Centonze, J. G. White, D. Armstrong, G. Robertson, and A. I. Ferguson, "All-solid-state ultrafast lasers facilitate multiphoton excitation fluorescence imaging," *Ieee Journal of Selected Topics in Quantum Electronics*, vol. 2, pp. 1051-1065, Dec 1996.
- [12] J. M. Hopkins, G. J. Valentine, B. Agate, A. J. Kemp, U. Keller, and W. Sibbett, "Highly compact and efficient femtosecond Cr : LiSAF lasers," *Ieee Journal of Quantum Electronics*, vol. 38, pp. 360-368, Apr 2002.

## Multiphoton Microscopy Using a Low Cost Femtosecond Cr:LiCAF Laser

### Sponsors

National Science Foundation – ECS-0456928, ECS-0501478

Air Force Office of Scientific Research – FA-9550-07-1-0101 and FA9550-07-1-0014

Scientific and Technical Research Council of Turkey –104T247

### Project Staff

Umit Demirbas, Professor Alphan Sennaroglu, Professor Franz X. Kaertner, Professor James G. Fujimoto, Dr. David Boas, Dr. Sava Sakadzic, Dr. Svetlana Ruvinskaya, Dr. Thorsten R. Mempel, Dr. Anna Moore

Multiphoton microscopy (MPM) enables high resolution imaging of physiology, morphology and cell-cell interactions in intact tissue and in live animals [1], and currently it is one of the most powerful tools in biomedical imaging. Unfortunately, wide-spread use of this powerful tool has been delayed, due to the high cost of the femtosecond lasers required as excitation sources (in general a femtosecond Ti:Sapphire laser costing >\$200k is used in commercial MPM systems). Working in collaboration with Dr. David Boas from Harvard Medical School, our group has shown that low-cost Cr:LiCAF lasers could also serve as an efficient source for MPM. Using the recently developed single-mode diode pumped Cr:LiCAF laser as an excitation source, we have demonstrated high resolution in-vivo MPM images with imaging depths up to 600  $\mu\text{m}$ . Performance is similar to what could be achieved using a Ti:Sapphire laser. With an emission peak centered around 800 nm, Cr:LiCAF laser is capable of exciting the majority of fluorophores used in MPM. Hence, we believe this achievement has the potential of reducing the cost of MPM systems [2], making this powerful tool more widely available.

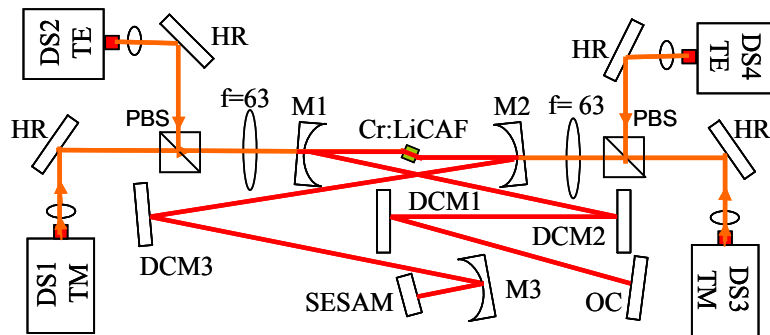


**Figure 1.** Schematic of the single-mode diode-pumped Cr<sup>3+</sup>:LiCAF laser used in MPM studies.

Figure 1 shows a schematic of the single-mode diode pumped Cr:LiCAF laser used in MPM studies. The laser was a compact version of the system described in the previous section on “Low-cost and Highly Efficient Femtosecond Lasers”. Neither the crystal nor the diodes require water cooling; hence a compact and portable system can be easily built. The laser produces ~80 fs pulses, with up to 1.8-nJ pulse energy at a repetition rate of 100 MHz. The spectrum of the pulses have a bandwidth of about 10 nm centered around 800 nm. The laser is turn-key and is immune to environmental fluctuations; thus, it does not require any previous laser expertise to operate. A neutral density (ND) filter was used to adjust the incident pump power on the sample. Dispersion pre-compensation is applied using an SF-10 prism pair to keep the pulsewidths on the sample around ~100 fs.

In our MPM work with the Cr:LiSAF laser, we have looked at three different areas in biomedical imaging: neuroscience, immunology and cancer research, where MPM is used extensively. As an example, here we will only present two of the MPM images taken with our Cr:LiCAF laser: (i) Rat’s cortical vasculature system as an example image in neuroscience, and (ii) Rat’s lymphatic

system as an example image in immunology. As just mentioned, neuroscience is one of the active research areas in biomedical imaging where MPM is used. In vivo MPM imaging of brain provides an unparalleled tool to understand the working mechanism of brain by enabling functional brain imaging using ion-sensitive fluorescent probes, where biochemical changes upon an excitation could be observed real-time. In Figure 2 (a), we see a 3-D MPM image of rat's cortical vasculature system. The image was taken in-vivo using the Cr:LiCAF laser as the excitation source and fluorescein was used as the marker. In this image, branching of capillaries up to a depth of 600  $\mu\text{m}$  could be observed. The resolution and the imaging depths obtained here are similar to the images that could be obtained using Ti:Sapphire technology, and proves that Cr:LiSAF could do the same job at a much lower cost.

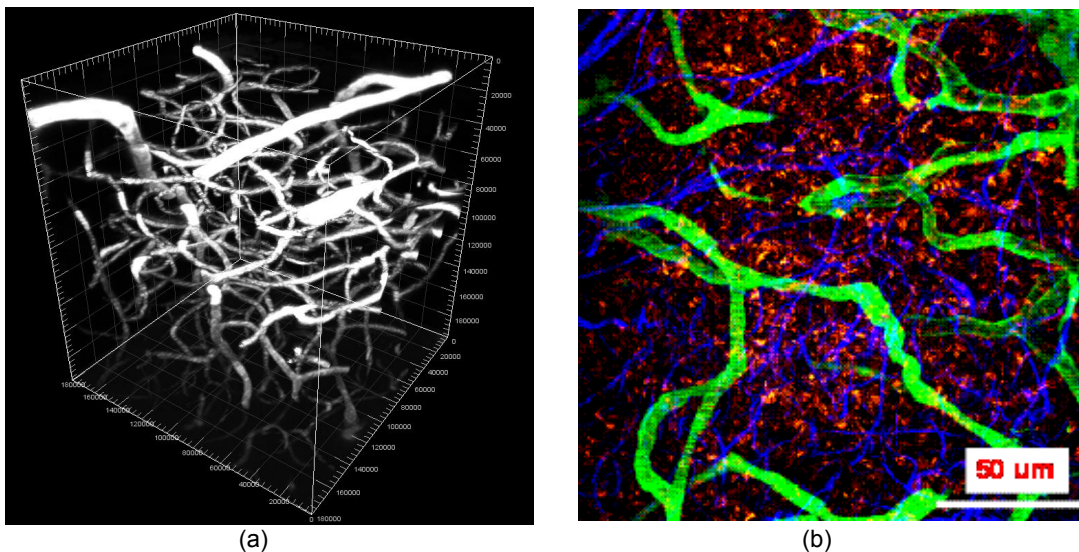


**Figure 2:** Multiphoton microscopy images taken with single-mode diode pumped Cr:LiCAF laser: (a) 3-D view of rat's cortical vasculature system up to a depth of 600  $\mu\text{m}$  (in vivo) (b) Rat's lymphatic system (in vivo): lymph nodes (red), capillaries (green), collagen fibers (blue)

Another research area that MPM is actively used is immunology. Studies of immune system with MPM help researchers to understand how our body fights with infectious pathogens on the cellular and molecular levels. In Figure 2 (b) we see a three color image of rat's lymphatic system, taken in-vivo using the Cr:LiCAF laser as the excitation source. Each color in the image shows a different structure in the immune system. In this image the blue color shows the collagen fibers where the emission is due to second harmonic generation by the structure itself. The red color shows the lymph nodes, where we used rhodamine for labeling. Lastly, green color shows the capillaries where fluorescein was used as a stain. Again the obtained image quality was similar to what could be obtained by using the expensive Ti:Sapphire technology.

One possible drawback of Cr:LiCAF as an excitation source for MPM might be its limited tunability compared to Ti:Sapphire. However, unlike single photon excitation, many fluorophores have quite broad multiphoton absorption bands; hence tunability is not as critical for most applications as in the case for single-photon excitation [3]. Besides that, the majority of fluorophores used in MPM imaging is excitable around 800 nm, where the Cr:LiCAF laser is a perfect match [4].

We believe diode pumped Cr:LiCAF is a promising alternative to Ti:Sapphire not only in MPM (or in biomedical imaging) but also in other scientific and technological areas such as spectroscopy, material processing, and optical frequency metrology. In terms of many parameters, Cr:LiCAF lasers could provide similar performance to Ti:Sapphire and could achieve 5-10 times reduction in cost, which could facilitate wider usage of femtosecond technology.

**References**

- [1] W. R. Zipfel, R. M. Williams, and W. W. Webb, "Nonlinear magic: multiphoton microscopy in the biosciences," *Nature Biotechnology*, vol. 21, pp. 1368-1376, Nov 2003.
- [2] J. M. Girkin and G. McConnell, "Advances in laser sources for confocal and multiphoton microscopy," *Microscopy Research and Technique*, vol. 67, pp. 8-14, May 2005.
- [3] J. M. Girkin, "Optical physics enables advances in multiphoton imaging," *Journal of Physics D-Applied Physics*, vol. 36, pp. R250-R258, Jul 21 2003.
- [4] C. Xu and W. W. Webb, "Measurement of two-photon excitation cross sections of molecular fluorophores with data from 690 to 1050 nm," *Journal of the Optical Society of America B-Optical Physics*, vol. 13, pp. 481-491, Mar 1996.

## Femtosecond Laser Frequency Combs, Optical Clocks and Phase Control

### 2-GHz Octave-Spanning Ti:sapphire Laser

#### Sponsors

Defence Advanced Research Projects Agency, DARPA HR0011-05-C-0155  
Air Force Office of Scientific Research and FA9550-07-1-0014

#### Project Staff

Li-Jin Chen, Andrew Benedick, Jonathan Birge, Michelle Sander and Prof. Franz X. Kärtner

Optical frequency combs based on self-referenced octave-spanning laser oscillators are versatile tools for frequency metrology, time resolved and frequency-domain spectroscopy, and optical arbitrary waveform generation (OAWG). To make this technique more powerful, oscillators operating at high repetition rates are highly desired because of its larger mode spacing and higher power per mode that enables a higher signal-to-noise ratio for frequency metrology and spectroscopy, as well as requiring lower resolving power of the spectral disperser in an OAWG.

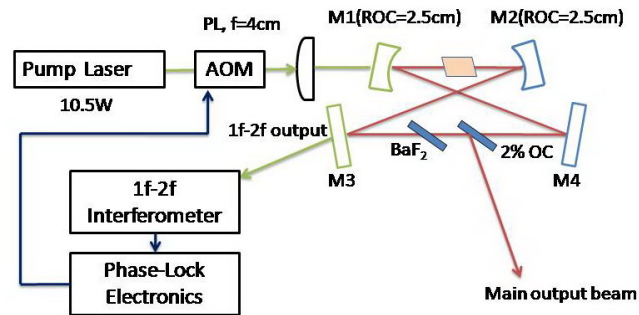
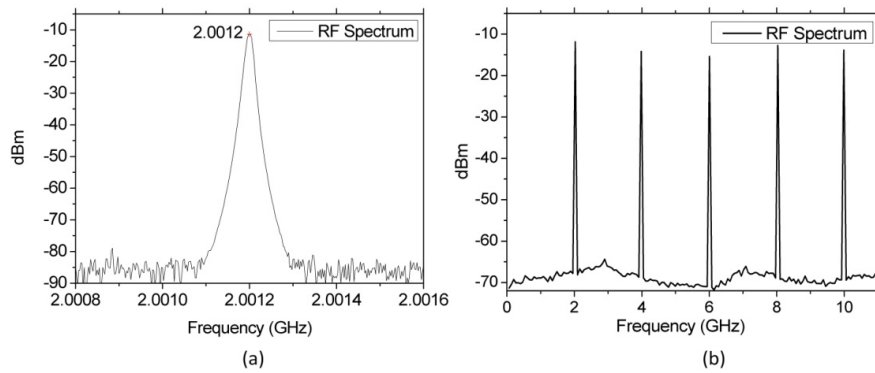


Fig. 1. Setup of the CE phase-stabilized 2-GHz Ti:sapphire laser.

As shown in Fig.1, we demonstrate a carrier-envelope (CE) phase-stabilized octave-spanning 2-GHz Ti:sapphire laser which is to our knowledge the highest repetition rate octave-spanning laser. Direct octave-spanning output is generated from a compact four-mirror cavity consisting of two curved broadband double-chirped mirrors (DCMs) with radius of curvature of 2.5cm, two flat DCMs, and two pieces of dispersive glass. Fine-tuning of intracavity dispersion is controlled through the insertion of a BaF<sub>2</sub> plate and a fused-silica wedge to achieve optimized Kerr-Lens modelocking (KLM). The fused-silica wedge also carries a broadband output-coupler (OC) coating designed to enhance the spectral wings of the output pulses by having 2% reflectivity in the center of the spectrum and >50% reflectivity below 650 nm and above 1050 nm.



**Fig. 3.** RF spectra showing (a) fundamental mode and (b) spectral envelope.

Mode-locking is unidirectional and easily started by translating mirror M2. Fig.2 show the RF spectrum of the detected pulse train verifying single-pulse operation. The laser generates, at 10.5 W of pump power, spectrum covering more than one octave [see Fig.3(a)] and about 660 mW total output power, split into a 600 mW main beam and a 62.1 mW 1f-2f output beam by our novel DCM mirror M3 for non-intrusive carrier-phase stabilization [1]. The average power of the 1f and 2f components, measured after 10 nm bandpass-filters centered at 560 nm and 1150 nm, are 160  $\mu$ W and 4.3 mW, respectively.

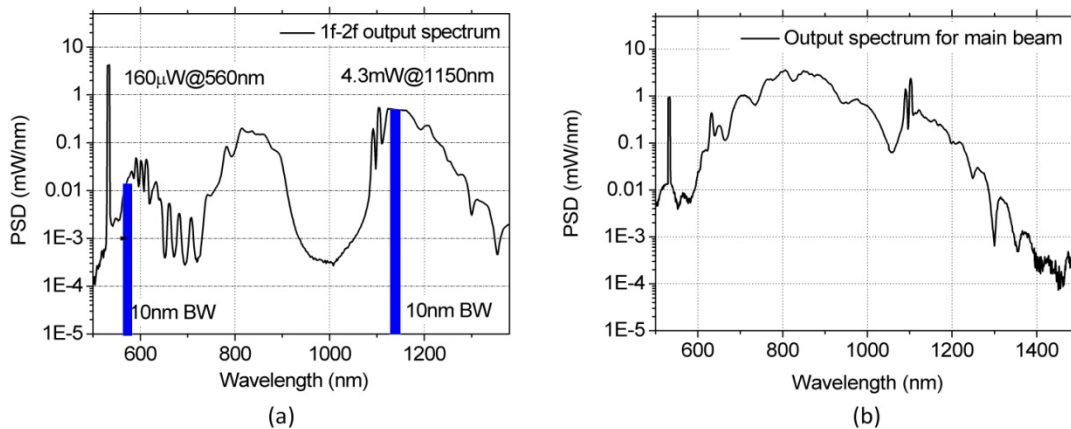


**Fig. 3.** Spectra of (a) 1f-2f output beam and (b) main output beam from the 2 GHz Ti:Sapphire laser.

We locked the CE offset frequency to a local oscillator set at 20 MHz through a phase-locked loop (PLL) that feeds an error signal to an acousto-optic modulator which regulates the pump power, thus shifting the CE frequency. As shown in Fig.4(a), the signal-to-noise ratio of the free-running CE beat note is as high as 50 dB measured with 100 kHz resolution bandwidth. In Fig.4(b) we further confirm that the linewidth of the CE beat note is below 10 Hz when the laser is phase-locked.

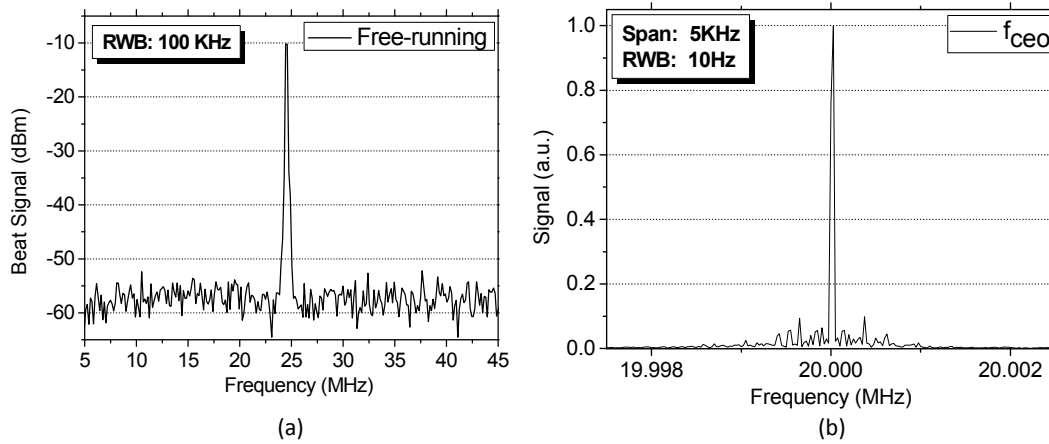


**Fig. 4.** (a) Free-running carrier-envelope beat note spectrum (log scale) (b) Locked carrier-envelope beat note spectrum (linear scale).

### References

- [1] H. M. Creps, J. R. Birge, E. L. Falcao-Filho, M. Y. Sander, A. Benedick, and F. X. Kärtner, "Non-intrusive phase-stabilization of sub-two-cycle pulses from a prismless octave-spanning Ti:sapphire laser," *Opt. Lett.* **33**:(8), 833-835 (2008).

## HeNe-CH<sub>4</sub> based Frequency Combs and Clocks using 1 GHz Repetition Rate

### Octave Spanning Ti:sapphire Lasers

#### Sponsors

Defence Advanced Research Projects Agency, DARPA HR0011-05-C-0155  
Air Force Office of Scientific Research and FA9550-07-1-0014

#### Project Staff

Andrew Benedick, Jonathan Birge, Dr. Peter Fendel, Li-Jin Chen, Dr. Richard Ell, Michelle Sander, Professor Franz X. Kärtner

High repetition rate, octave spanning Ti:sapphire oscillators have numerous applications in time resolved and frequency domain spectroscopy, frequency metrology and optical arbitrary waveform generation. As compared to lower repetition rate fiber and other solid state lasers no additional external broadening is necessary and the large mode separation enables easier access to individual comb lines with more power per mode.

We demonstrate here a greatly improved octave spanning 1 GHz Ti:sapphire laser [1] using the most broadband double-chirped mirror pairs, optimized Kerr-Lens modelocking (KLM) and an optimized output coupler. As a result the laser generates, at 9 W of pump power, 0.6 W-1 W of output power with an output spectrum of more than one octave as measured on a linear scale, see Figure 1a. The spectrum corresponds to a pulse with a Fourier limited pulse duration of 3.5 fs. Second harmonic generation of the output beam in 1mm LBO directly generates 1f-2f beatnotes for carrier-envelope phase stabilization with >55dB signal-to-noise (SNR) in 100kHz bandwidth, Figure 1b top trace. Using the central part of the output spectrum, difference frequency generation (DFG) 3.39  $\mu\text{m}$  is generated in a 5 mm long Periodically Poled Lithium Niobate crystal (PPLN). The 3.39  $\mu\text{m}$  radiation is strong enough to result in a beatnote with a single frequency HeNe reference laser of 30dB, Figure 1b bottom trace. This laser serves as the clockwork for a HeNe CH<sub>4</sub>-based molecular clock [2] with a measured Allan variance approaching  $10^{-14}$  in 100s and as an absolute femtosecond laser frequency comb for an optical arbitrary waveform generator.

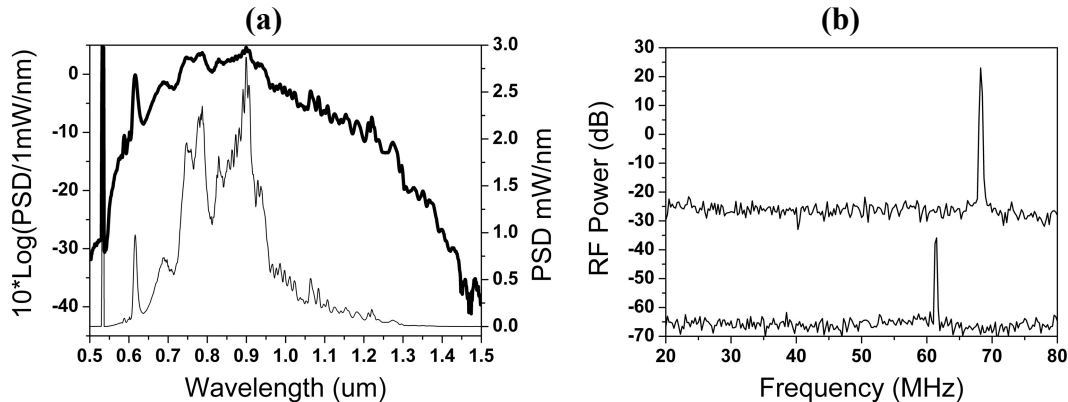


**Fig. 1:** (a) Output spectrum of the 1GHz Ti:Sapphire laser on a logarithmic(top) and linear(bottom) scale;  
(b) 1f-2f beatnote (top) and 3.39 $\mu\text{m}$  beatnote with HeNe reference laser (bottom).

The laser is a standard KLM four mirror Ti:sapphire ring laser with a 1 GHz repetition rate using double-chirped mirror pairs (DCMPs) to provide precise dispersion compensation together with a BaF<sub>2</sub>-plate and wedge, both inserted at Brewster's angle. 4% output coupling is achieved by coating one side of the BaF<sub>2</sub> wedge. The output increases from the center of the spectrum to >50% above 1050 nm and below 650 nm. With 9 W of pump power, 600 mW of output power with a FWHM spectrum of >200 nm is achieved, Fig. 1.

Initial attempts have been made to characterize the frequency comb system which is shown schematically in Fig. 2. Most notable has been a comparison against a cavity stabilized laser diode at 674nm. This laser diode is stabilized using the Pound-Drever-Hall technique to a ULE

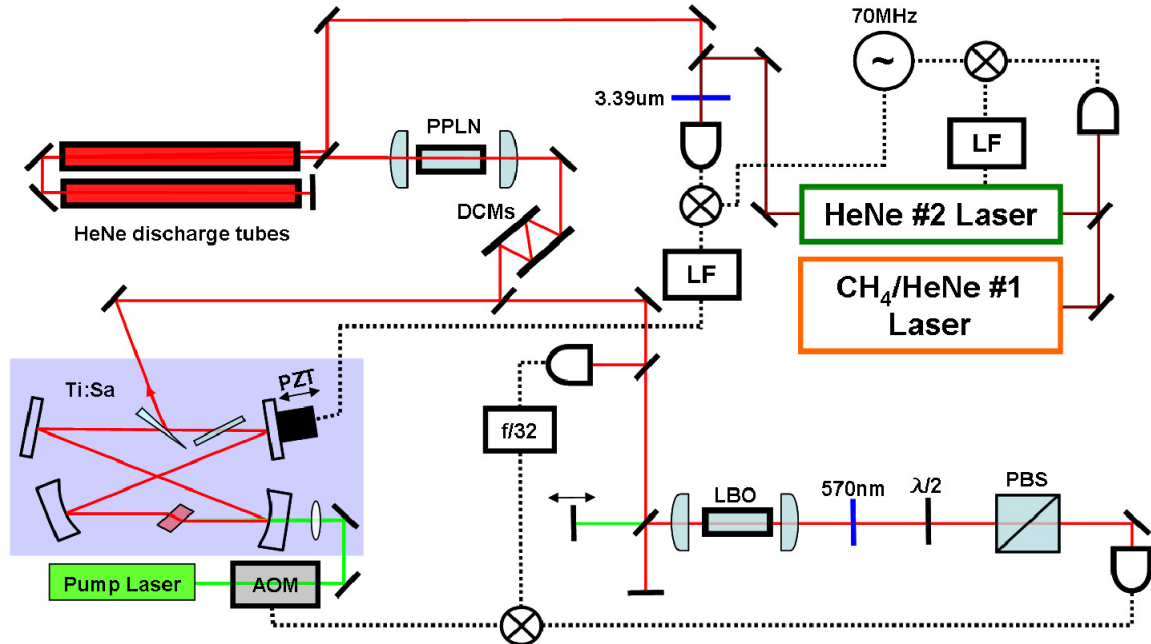


**Fig.2.** Schematic representation of the 1GHz Ti:Sapphire based optical clock and frequency comb system. LF, Loop Filter; DCM, Double chirped dispersion compensating mirrors; PBS, Polarizing beam splitter; AOM, Acousto-Optic modulator; PZT, Piezo electric transducer; PPLN, Periodically poled lithium niobate; LBO, Lithium triborate.

glass based reference cavity to a level of approximately 100Hz in one second. For comparison with the frequency comb, a heterodyne beat was generated between the stabilized laser diode and one tooth of the stabilized frequency comb with the resulting beat signal counted using a standard frequency counter. As can be seen in Fig. 3, the stability of the frequency comb/laser diode system is found to be  $5 \times 10^{-13}$  at one second with a  $1/\sqrt{T}$  frequency aging characteristic of the ULE based cavity. These results indicate that the measured stability is limited by the ULE cavity and that comparison against a higher stability reference should yield results closer to the stability of the  $\text{CH}_4/\text{HeNe}$  reference laser on which the frequency comb system is based.

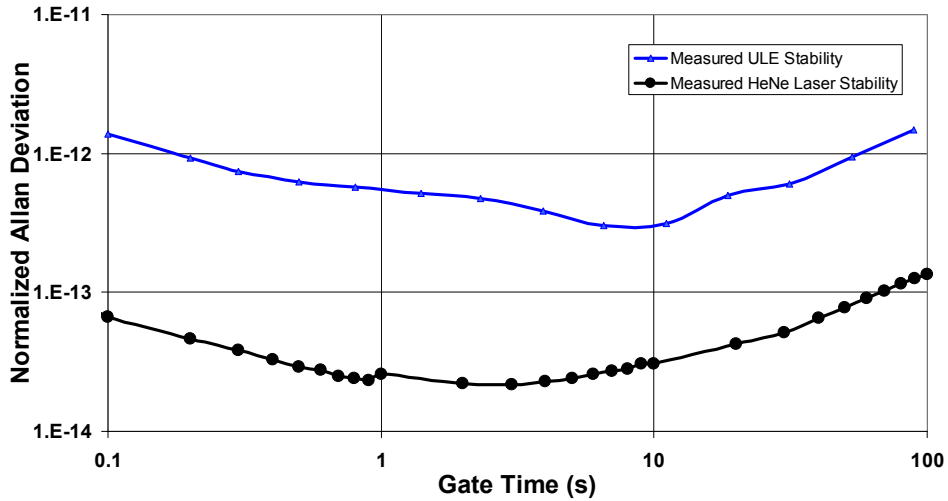


**Fig.3.** Results of heterodyne type Allan Deviation measurements between the 1GHz Ti:Sapphire frequency comb system and a ULE cavity stabilized laser diode (upper trace), and between two identical  $\text{CH}_4$  stabilized HeNe lasers (lower trace). The ultimate frequency stability of the frequency comb system should approach the lower trace.

**References**

1. T.M. Fortier, A.Bartels, S.A.Diddams "Octave Spanning Ti:Sapphire laser with repetition rate >1GHz," *Optics Letters* 31 (7): 1011-1013 APR 1 2006
2. S. Foreman, A. Marian, J. Ye, E.A. Petrukhin, M.A. Gubin, O.D. Mücke, F.N.C. Wong, E.P. Ippen, F.X. Kärtner "Demonstration of a HeNe/CH<sub>4</sub>-based optical molecular clock," *Optics Letters* 30 (5): 570-572 MAR 1 2005
3. O. D. Mücke, O. Kuzucu, F. N. C. Wong, E. P. Ippen, and F. X. Kärtner, S. M. Foreman, D. J. Jones, L.S. Ma, J. L. Hall, and J. Ye "Experimental implementation of optical clockwork without carrier-envelope phase control," *Optics Letters* 29 (23): 2806-2808 DEC 1 2004

## Ti:Sapphire Frequency Combs for High-Precision Radial Velocity Measurements in Astrophysics

### Sponsors

Defence Advanced Research Projects Agency, DARPA HR0011-05-C-0155  
Air Force Office of Scientific Research and FA9550-07-1-0014

### Project Staff

Andrew J. Benedick, Chih-Hao Li, Dr. Peter Fendel, Alexander G. Glenday, Professor Franz X. Kärtner, Dr. David F. Phillips, Professor Dimitar Sasselov, Dr. Andrew Szentgyorgyi and Professor Ronald L. Walsworth

The accuracy and long-term stability of state-of-the-art astrophysical spectrographs are currently limited by the wavelength-calibration source, typically either thorium–argon lamps or iodine absorption cells. These existing calibration sources are limited to the red-to-near-IR spectral bands most useful for exoplanet searches around M stars and dark matter studies in globular clusters. Iodine cells have very few spectral lines in the red and near-IR spectral bands, while thorium–argon lamps have limited lines and unstable bright features that saturate spectrograph detectors. Recently, laser frequency combs have been suggested as potentially superior wavelength calibrators<sup>1,2</sup> because of their good long-term stability and reproducibility, and because they have useful lines in the red-to-near-IR range. The absolute optical frequencies of the comb lines are determined by  $f = f_{\text{ceo}} + m \times f_{\text{rep}}$ , where  $f_{\text{rep}}$  is the repetition rate,  $f_{\text{ceo}}$  is the carrier-envelope offset frequency and  $m$  is an integer. Both  $f_{\text{rep}}$  and  $f_{\text{ceo}}$  can be synchronized with radio-frequency oscillators referenced to atomic clocks. For example, using the generally available Global Positioning System (GPS), the frequencies of comb lines have long-term stability and precision of better than  $10^{-12}$ . For the calibration of an astrophysical spectrograph, stability and precision of  $3 \times 10^{-11}$  are sufficient to measure a velocity variation of  $1 \text{ cm s}^{-1}$  in astronomical objects. This novel<sup>1</sup>, wide-line-spacing ‘astro-comb’ can provide improved wavelength calibration for a wide range of existing and planned astrophysical spectrographs.

The astro-comb set-up is shown schematically in Fig. 1. An octave-spanning optical frequency comb with a 1-GHz repetition rate (‘source-comb’) is generated by a mode-locked Ti:sapphire femtosecond laser<sup>3</sup>. The linewidth of each comb line is  $<1 \text{ kHz}$ , with both  $f_{\text{rep}}$  and  $f_{\text{ceo}}$  are stabilized using low-noise frequency synthesizers, which can be referenced to an atomic clock. The stabilized source-comb light passes through a FP cavity that filters out unwanted comb lines and increases the line spacing. The FP cavity is stabilized by an injected diode laser signal that is itself stabilized to the Rb D1 line (7,947 Å) using a dichroic-atomic-vapour laser lock (DAVLL).

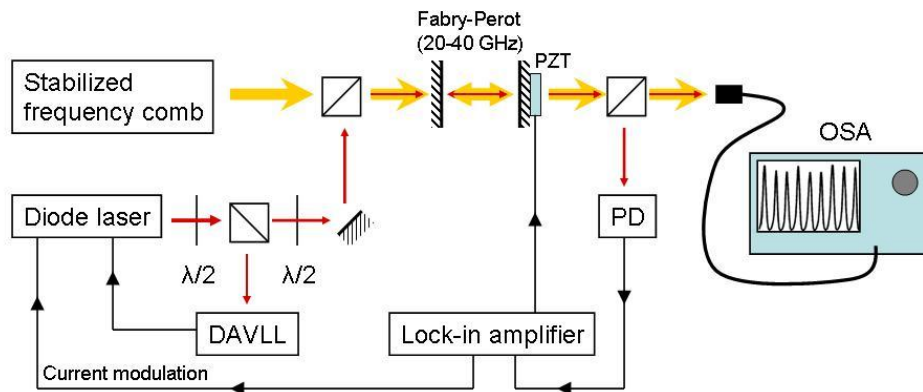


**Fig. 1:**Block diagram of the experimental setup. The stabilized 1-GHz frequency comb emitted from a femtosecond laser passes through a FP that filters out unwanted comb lines and increases the line spacing up to 40 GHz. The FP is stabilized by a diode laser which is locked to Rb D1 (794.7 nm) with the Dichroic Atomic Vapour Laser Lock (DAVLL) scheme.

To realize an astrophysical wavelength calibrator, the FP cavity must filter comb lines over a broad spectral range. The mirrors used in the plane-parallel FP cavity have  $\sim 99\%$  reflectivity and optimized group delay dispersion (GDD) ( $<10 \text{ fs}^2$ ) in the range of 770 nm to 920 nm. We measured the finesse of the FP cavity to be  $\sim 250$  at 794.7 nm, which is consistent with the theoretical limit estimated from the mirror reflectivity and Fresnel losses. The GDD-optimized mirrors enable the generation of a filtered comb spanning a bandwidth of  $\sim 100 \text{ nm}$ . With straightforward adjustment of the free spectral range of the FP cavity to approximately equal an integer multiple of  $f_{\text{rep}}$ , we realized such comb-line filtering. For example, Fig.2(a) shows the measured astro-comb output spectrum spanning a bandwidth of  $\sim 100 \text{ nm}$ , with 37-GHz line spacing and power  $\sim 10\text{--}100 \text{ nW}$  in each comb line.

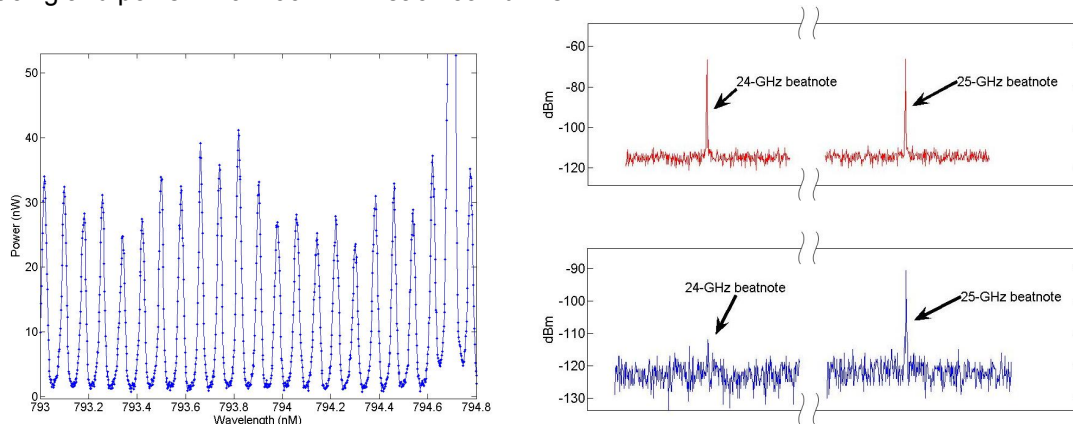


**Fig.2.** (a) Example of filtered comb lines from the prototype astro-comb. The very tall “tooth” in this figure is an injected laser signal that comes from the DAVLL-locked diode laser used to stabilize the Fabry-Perot cavity. It is also used as a reference to calibrate the comb’s teeth. This prototype astro-comb has typical tooth-spacing of about 37 GHz and wavelength coverage of 100 nm. (b) FP cavity is tuned such that the astro-comb has a 25-GHz line spacing. A fast photodiode and spectrum analyser are used to measure the power in the 24-GHz and 25-GHz beatnotes from the 1-GHz source-comb (upper) and the 25-GHz astro-comb (lower) in the band 815nm–845nm. The  $\sim 22\text{-dB}$  suppression of the 24-GHz beatnote in the astro-comb output signal corresponds to a  $\sim 25\text{-dB}$  single-sided suppression of extraneous comb lines, consistent with the FP cavity finesse of 250.

In Fig.2(b), we show a direct measurement of the suppression of extraneous lines of the astro-comb. The measured single-sided suppression of extraneous comb lines of more than 25 dB is consistent with the measured FP cavity finesse of 250. The DAVLL-stabilized FP cavity is quite robust, remaining locked for periods of days. The absolute uncertainty in the DAVLL stabilized system is below 0.5 MHz, which is more than sufficient to maintain a sensitivity of  $1 \text{ cm s}^{-1}$ . Residual frequency noise in the DAVLL is  $<300 \text{ kHz Hz}^{-1/2}$ , corresponding to an amplitude fluctuation of  $<0.1\%$  for the suppressed (extraneous) comb lines. The resultant frequency noise in the desired astro-comb line spacing is  $<3 \text{ kHz Hz}^{-1/2}$ . Taking advantage of the ultrastable source-comb lines, the astro-comb output spectrum measured by the spectrograph is more stable than the FP cavity by more than two orders of magnitude. Consequently, the stability of the astro-comb is more than adequate for wavelength calibration of astrophysical spectrographs to  $1 \text{ cm s}^{-1}$  sensitivity.

### References:

- [1] M.T. Murphy, Th. Udem, R. Holzwarth, A. Sizmann, L. Paspuini, C.Araujo-Hauck, H. Dekker, M. Fischer, T.W. Hansch and A. Manescau, “High Precision wavelength calibration with laser frequency combs,” *Mon. Not. R. Astron. Soc.* 380(2): 839-847 (2007).
- [2] C.H. Li, A.J. Benedick, P. Fendel, A.G. Glenday, F.X. Kaertner, D.F. Phillips, D. Sasselov, A. Szentgyorgyi and R.L. Walsworth, “A laser frequency comb that enables radial velocity measurements with a precision of  $1 \text{ cm s}^{-1}$ ,” *Nature* 452(7187): 610-612 (2008).
- [3] A. Benedick, J. Birge, O.D. Mucke, M. Sander and F.X. Kaertner “Octave Spanning 1GHz Ti:Sapphire Oscillator for HeNe CH4-based frequency combs and clocks,” *CLEO/Europe*, Munich, Germany, June 17-22, 2007.

## Drift-Free Microwave Signal Synthesis from Mode-Locked Lasers with Sub-10 fs Residual Timing Jitter

### Sponsors

Office of Naval Research (ONR), Contract N00014-02-1-0717  
 Air Force Office of Scientific Research (AFOSR), FA9550-07-1-0014  
 Sandia National Laboratories, Contract 777117

### Project Staff

Dr. Jungwon Kim and Professor Franz X. Kärtner

Optical pulse trains from mode-locked lasers show sub-fs timing jitter in the high frequency range [1]. Although the short-term jitter is sub-fs range and the relative microwave stability of optical atomic clocks can reach  $10^{-18}$  [2], the extraction of microwave signals from pulse trains is limited by excess noise in the photodetection process [3,4]. In frequency metrology, this excess noise limits the achievable microwave frequency stability, so far with the best reported result of  $2.6 \times 10^{-17}$  [2]. For high-stability optical/RF synchronization, which is a prerequisite for large-scale x-ray free-electron lasers (XFELs), this limits the continuous operation capabilities of such facilities over long time scales (e.g., >10 minutes) by timing drift between the optical pulse trains and the regenerated microwave signals.

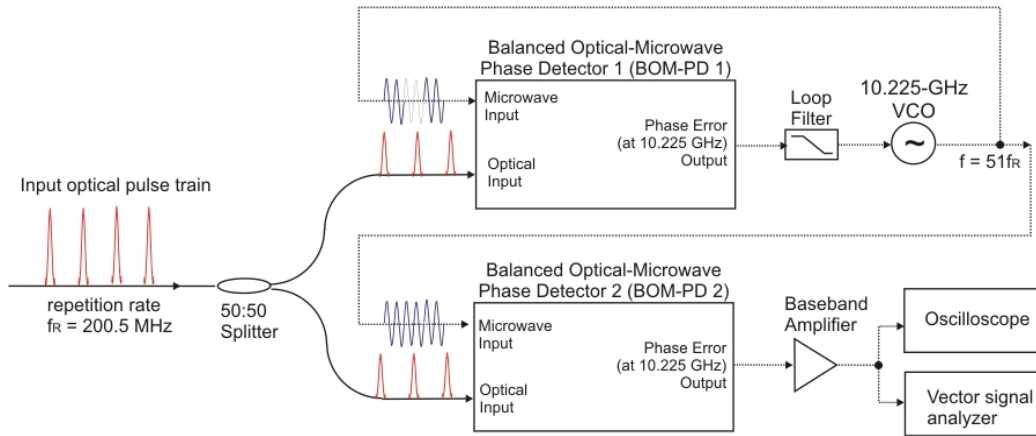
One way to overcome these limitations is by detecting the timing error between the optical pulse train and the microwave signal directly in the optical domain and using this information for tight synchronization of microwave signal to the pulse train. Previously, we demonstrated a balanced optical-microwave phase detector (BOM-PD) [5,6] based on electro-optic sampling with a differentially-biased Sagnac interferometer. Here, we used the BOM-PDs both for synchronization between optical and microwave signals and for monitoring the out-of-loop timing jitter over 10 hours without drift. In this way, we demonstrate 4.4 fs rms jitter in the [1 Hz, 1 MHz] range, and keep this level of accuracy with 6.8 fs rms integrated jitter over 10 hours. This corresponds to an unprecedented relative timing stability of  $1.9 \times 10^{-19}$ .

Figure 1 shows the schematic of the experimental setup for long-term timing jitter measurements between the 10.225-GHz microwave signal and the 200.5-MHz repetition rate optical pulse train. The optical pulse train is generated by a commercial 200-MHz Er-fiber laser. While keeping the architecture of previous implementations of BOM-PDs in [5], we improved the synchronous detection by using the same 500-MHz ( $2.5f_R$ ) signal both for driving the phase modulator and for downconversion of the error signals. Two almost identical but independent BOM-PDs were used to extract the timing error between the pulse train and the microwave signal. The first BOM-PD is used for synchronizing the optical pulse train with the microwave signal from the voltage-controlled oscillator (VCO). The second BOM-PD is used to measure the out-of-loop residual timing jitter between the regenerated microwave signal and the optical pulse train. This approach enables a long-term stable measurement of the microwave signal stability.

The measured timing jitter integrated from 1 Hz to 1 MHz is 4.4 fs, and most of the jitter is contributed in the high frequency range (above 100 kHz) from the limited feedback loop bandwidth and the phase noise of the free-running VCO. Figure 2 shows the long-term measurement of timing jitter with 1-MHz bandwidth over 10 hours. The relative rms timing jitter between the microwave signal and the pulse train shows 6.8 fs integrated from 27  $\mu$ Hz to 1 MHz. The maximum drift over 10 hours is 15 fs (maximum deviation of yellow curve in Fig. 2).

For timing distribution and synchronization, this result demonstrates that the timing between microwave signals and optical pulse trains can always be kept within  $\pm 23$  fs (the measured peak-to-peak timing jitter in the 27  $\mu$ Hz – 1 MHz range) over a time span of 10 hours. It also assures that the maximum slow timing drift stays within 15 fs over 10 hours. In the case of accelerators and XFELs, this will enable long-term drift-free synchronization of low-level RF systems within 10

fs accuracy, which has been impossible with pure-RF techniques or direct photodetection-based optical techniques. For frequency metrology, this result demonstrates that the relative stability of the microwave signal read-out process can be improved to  $\Delta t_{rms} / T = (6.8 \times 10^{-15}) / (36,000) = 1.9 \times 10^{-19}$ . This can significantly enhance the microwave signal read-out capabilities for optical atomic clocks, which is not limited by excess noise in the photodetection process.



**Figure 1:** Experimental setup for long-term out-of-loop relative timing jitter measurement between the optical pulse train and the regenerated microwave signal.

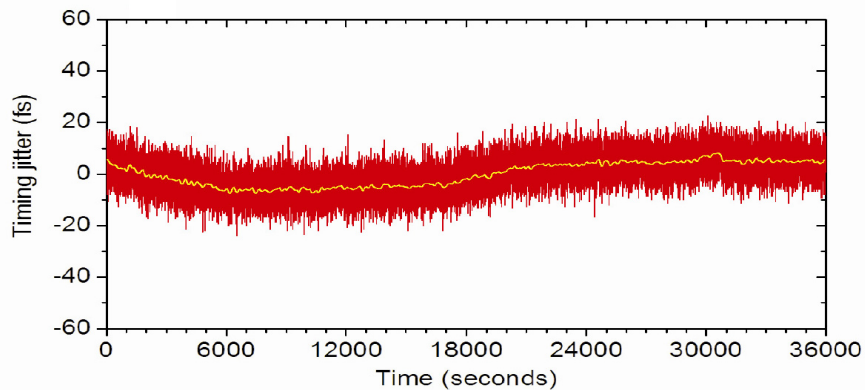


**Figure 2:** The long-term out-of-loop jitter measurement shows that the integrated jitter is 6.8 fs over 10 hours. The yellow line indicates the slow drift calculated from the jitter measurement with a time constant of 100 s. The maximum drift is 15 fs. The relative stability reaches  $1.9 \times 10^{-19}$  in 10 hours.

## References

- [1] J. Kim, J. Chen, J. Cox and F. X. Kärtner, "Attosecond-resolution timing jitter characterization of free-running mode-locked lasers," *Opt. Lett.* 32(24): 3519-3521 (2007).
- [2] L.-S. Ma et al, "Frequency uncertainty for optically referenced femtosecond laser frequency combs," *IEEE J. Quantum Electron.* 43(1): 139-146 (2007).
- [3] E. N. Ivanov, S. A. Diddams and L. Hollberg, "Study of the excess noise associated with demodulation of ultra-short infrared pulses," *IEEE Trans. UFFC* 52(7): 1068-1074 (2005).
- [4] E. N. Ivanov, S. A. Diddams and L. Hollberg, "Noise properties of microwave signals synthesized with femtosecond lasers," *IEEE Trans. UFFC* 54(4): 736-745 (2007).
- [5] J. Kim, F. X. Kärtner and F. Ludwig, "Balanced optical-microwave phase detectors for optoelectronic phase-locked loops," *Opt. Lett.* 31(24): 3659-3661 (2006).
- [6] J. Kim, F. Ludwig, M. Felber and F. X. Kärtner, "Long-term stable microwave signal extraction from mode-locked lasers," *Opt. Express* 15(14): 8951-8959 (2007).

## Sub-10 femtosecond Precision, Long-term Stable Timing Distribution Over Multiple Fiber Links

### Sponsors

Air Force Office of Scientific Research (AFOSR) FA9550-06-1-0468

Office of Naval Research (ONR) N00014-02-1-0717

EuroFEL

University of Wisconsin, Synchrotron Radiation Laboratory

### Project Staff

Jonathan A. Cox, Dr. Jungwon Kim and Professor Franz X. Kärtner

Ultra-low noise timing distribution and synchronization of lasers and microwave signals to a single master oscillator over one to ten kilometers is critical to the implementation of next-generation timing and phase sensitive systems, such as x-ray free electron lasers (XFEL) and phased antenna arrays for radio astronomy [1]. An all-optical scheme for timing distribution employing optical fiber for transmission is ideal since it permits sub-femtosecond performance at low-cost, with low-complexity and robust operation. With a fiber laser as the master oscillator, commercially available with less than 10 femtoseconds (fs) of timing jitter [10 kHz, 10 MHz], 100 fs pulses at 200 MHz can be transmitted over multiple fibers to directly provide a useable timing signal at numerous harmonics of the laser repetition rate [2, 3]. Furthermore, such ultrafast pulses allow for stabilization of the fiber link at the attosecond level with an all-optical, temperature-invariant technique, balanced optical cross correlation [1]. As a result, we have demonstrated the distribution of an ultrafast, optical pulse train over two independent, 300 meter long, stabilized fiber links with less than 1 fs rms of timing jitter [0.1 Hz, 100 kHz], and 6.4 fs rms of drift over 72 hours of continuous, unaided operation [4  $\mu$ Hz, 0.5Hz]. This corresponds to a long-term fractional timing stability of  $2 \cdot 10^{-20}$  between the outputs of both links. Coupling the ultrafast timing distribution system with the low-noise, low-drift (<6.8 fs rms [27 $\mu$ Hz, 1 MHz]) optoelectronic microwave signal regeneration system makes robust, cost-effective and long-term sub-10-femtosecond timing distribution possible [4].

The system operates by stabilizing the total group delay, or time-of-flight, of a dispersion compensated single mode fiber link with a motorized free space delay and a piezoelectric fiber stretcher, as shown in Figure 1. In this way, a  $\sim$ 100 fs pulse train from a 200 MHz erbium fiber laser is delivered across 300 meters of fiber. Measurement of the optical delay is made by performing an optical cross-correlation between a new pulse entering the link from the laser and an old pulse that was reflected back from the end of the link by the 50 percent faraday rotating mirror (FRM). This cross-correlation is performed with a periodically poled KTP (PPKTP) balanced cross-correlator, providing a measurement of the delay between the two pulses [1]. The error signal, in turn, drives the loop filter controlling the fiber stretcher, to remove the majority of fast fiber length fluctuations below 1 kHz. In addition, a motor controller adjusts the free space delay to keep the loop filter in range. To overcome the link loss, an in-loop EDFA is also implemented.

Measurement of the timing stability between the outputs of the two links is also performed with the out-of-loop PPKTP cross-correlator, as shown in Figure 1. The response of the cross-correlator is calibrated against the time delay provided by the piezo fiber stretcher. Over a frequency interval from 0.1 Hz to 100 kHz, we observed a timing jitter below 1 fs rms. In addition, from 35  $\mu$ Hz to 100 kHz, as computed from the average of nine, eight-hour intervals, we observed a timing jitter of 3.3 fs rms. Furthermore, over a 72 hour interval of continuous, unaided operation, shown in Figure 2, we observed only 6.4 fs rms drift from 4  $\mu$ Hz to 0.5 Hz. Moreover, the timing signal remained within 16.4 fs pk-to-pk over the full 72 hours.

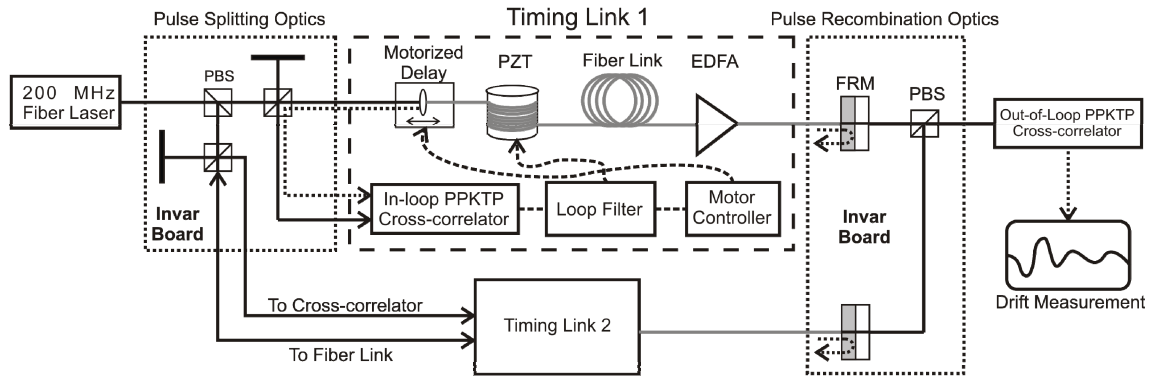


**Fig. 3.** Schematic of the timing link system with path length sensitive optics mounted in a symmetric fashion on temperature stabilized Invar breadboards. The experimental apparatus consists of two identical timing links for measurement purposes.

Since the optics are constructed on a highly temperature invariant breadboard in a symmetrical layout, we believe the performance is currently limited by the polarization mode dispersion (PMD) of SMF-28e fiber. With an upper limit on PMD ( $PMD_Q$ ) of 60 fs/ $\sqrt{\text{km}}$ , one expects no more than 33 fs PMD per link, depending on the stress applied to the fiber. Consequently, we expect the performance of the system with standard single mode fiber (SMF) to be, in large part, limited by the PMD of the SMF and the physical stresses exerted upon it.

In conclusion, we have demonstrated the first timing distribution system capable of operating with 10 fs absolute, or  $2 \cdot 10^{-20}$  relative, precision over multiple days. Strategies for overcoming PMD effects can be implemented to reach long term stable sub-femtosecond performance. When combined with optoelectronic microwave signal regeneration [4], this technology represents a complete set of tools for distributing and extracting a 10 fs timing signal in a robust and cost-effective fashion.

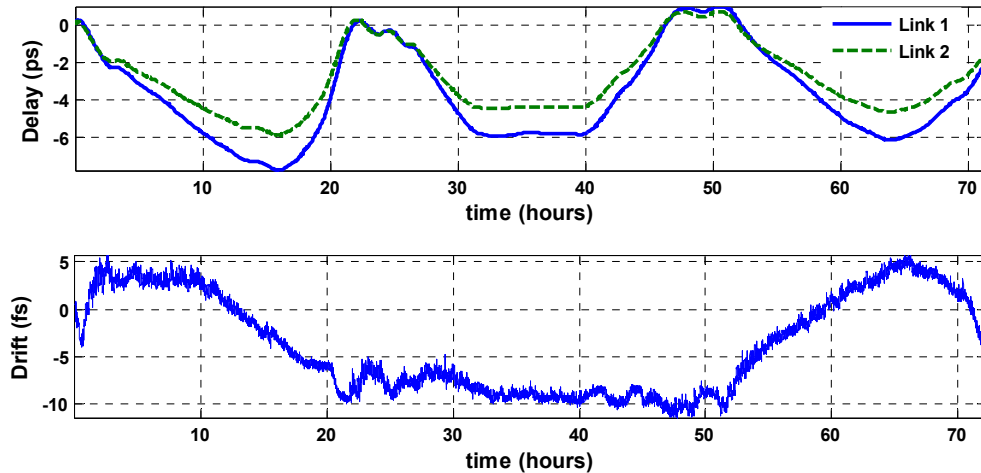


**Fig. 2.** The long-term timing drift shown in the time domain as measured over 72 hours. The upper plot shows the free space delay correction applied by the motors. The lower plot shows the timing drift between the link outputs, which was 6.4 fs rms over 72 hours [4  $\mu\text{Hz}$ , 0.5 Hz] and within 16.4 fs peak-to-peak.

Refernces

- [1] J. Kim, J. Chen, Z. Zhang, F. Wong, F. Kaertner. *Opt. Lett.* 32, 1044 (2007).
- [2] J. Kim, J. Chen, J. Cox, F.X. Kaertner. *Opt. Lett.* 32, 3519 (2007).
- [3] N. Newbury, P. Williams, W. Swann. *Opt. Lett.* 32, 3056 (2007).
- [4] J. Kim, F.X. Kaertner. Conference on Lasers and Electro-Optics, 2008. (CLEO).

## Optical Arbitrary Waveform Generation in the 1 – 2 $\mu$ m Wavelength Regime

### Sponsors

Defense Advanced Research Projects Agency, Contract HR0011-05-C-0155

Office of Naval Research MURI, Contract N00014-02-1-0717

Air Force Office of Scientific Research, Contract FA9550-07-1-0014

### Staff

David Chao, Jason Sickler and Professor Erich Ippen

Considerable progress has been made in our effort toward the creation of laser sources for truly arbitrary, and precisely referenced, optical waveforms at 1.5 $\mu$ m wavelengths. The high repetition-rate femtosecond fiber laser oscillators that have been developed toward this end have been described previously and elsewhere in this report. Here we discuss progress in the development of a high power fiber amplifier for these rep rate oscillators and success in frequency referencing the oscillator frequency comb. Amplification of the oscillator pulses must be sufficient for subsequent octave-spanning spectral broadening in a highly nonlinear fiber. Figure 1 shows the fiber amplifier we have used. Similar to previous, lower rep rate systems it consists of a single stage of highly doped erbium fiber with normal dispersion to avoid soliton break-up effects. Pumped in both forward and backward direction the amplifier has an output power of about 300mW for an input power of 5mW at 200MHz. Although there is some gain narrowing in the early part of the amplifier, pulse compression and nonlinearity near the end of the amplifier actually expands the spectrum. Recompression in a short section of SMF post-chirp fiber shortens the output pulses to 50fs.

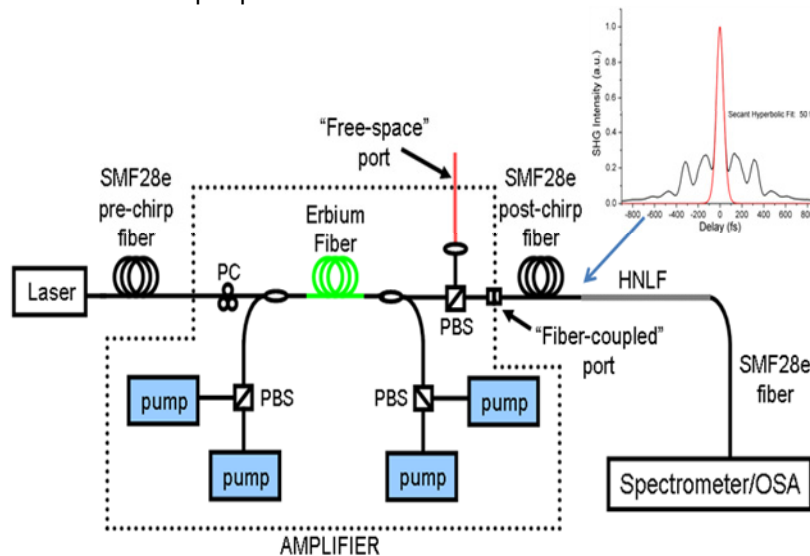


**Figure 1:** High-power 200MHz femtosecond pulse fiber amplification and continuum generation in highly nonlinear fiber (HNLF).

An autocorrelation of the amplified pulses indicates that a significant fraction of the energy remains in the wings. Nevertheless, these pulses are sufficient to produce the continuum spectrum shown in Figure 2. This continuum contains approximately 250 mW of total power, and nonlinear fiber used for the generation is the OFS HNLF Type B fiber. Colored bars in the illustrated spectrum indicate the frequencies selected for subsequent f-2f locking by SHG and for rep rate locking via DFG to a methane-stabilized HeNe reference laser operating at 3.39 $\mu$ m.

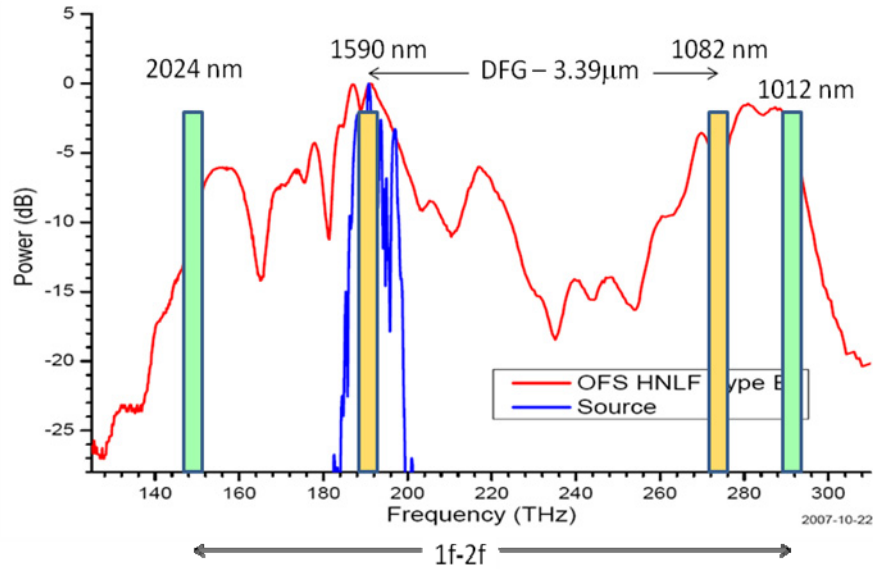


**Figure 2:** Plot of octave-spanning spectrum generated in HNLf. The wavelengths used for 1f-2f control and for DFG to 3.39 $\mu$ m are indicated.

Figure 3 shows a schematic of the interferometer used to obtain the 1f-2f beat signal needed for stabilizing the  $f_{\text{ceo}}$  of the oscillator.

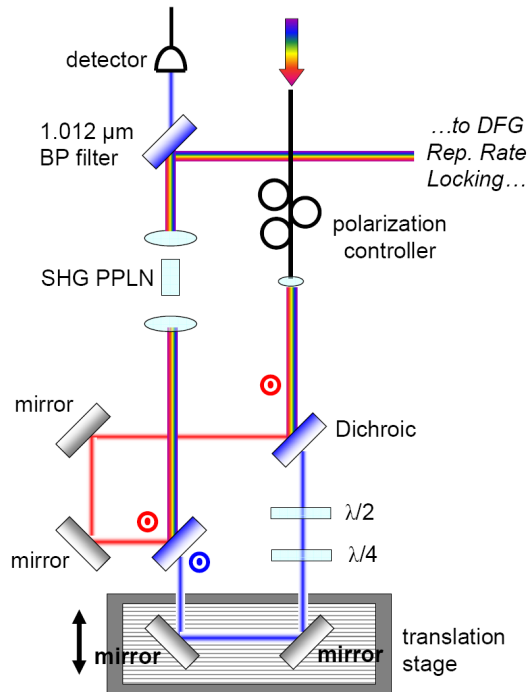


**Figure 3:** Schematic of the 1f-2f interferometer.

The polarization of the supercontinuum is first adjusted using an inline fiber polarization controller to align the  $\lambda_f$  polarization for optimal SHG conversion. The wavelengths are then separated by dichroic mirrors so that the relative delay between  $\lambda_f$  and  $\lambda_{2f}$  can be optimized. After the beams

are combined, the  $\lambda_f$  light is frequency doubled with a PPLN crystal. The  $\lambda_{2f}$  light, both originally from the supercontinuum spectrum, and generated in the PPLN crystal, are filtered with a 15 nm bandpass filter centered at  $\lambda_{2f}$ . The resulting beam is then placed on an avalanche photodiodes to generate the  $f_{ceo}$  beat.

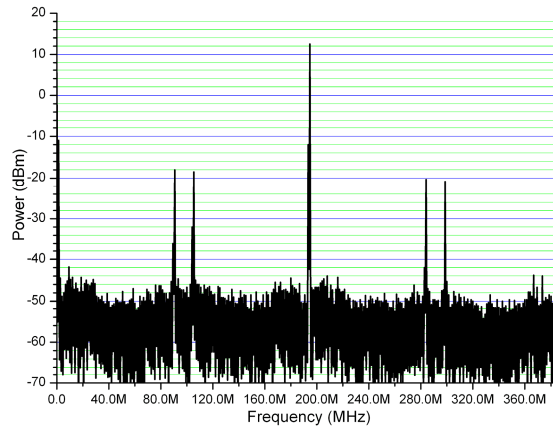


**Figure 4.** Beat signal from the 1f-2f interferometer, measured out to the second harmonic of the laser repetition rate.

The spectrum of the detector mixing products spanning from DC to the second repetition rate mixing product is shown in Figure 4. The beat signal is at least 30 dB above the noise floor, which is enough to provide an  $f_{ceo}$  lock.

Left alone on the optical table, air current and vibrations cause the  $f_{ceo}$  sidebands to fluctuate significantly, by at least tens of MHz every second, which would make obtaining and maintaining a lock difficult. By providing a box to reduce air currents and vibration isolation for the laser, the  $f_{ceo}$  sidebands become much more stable, varying at rates less than 1 MHz per second. This level of stability is sufficient for initiating a lock.

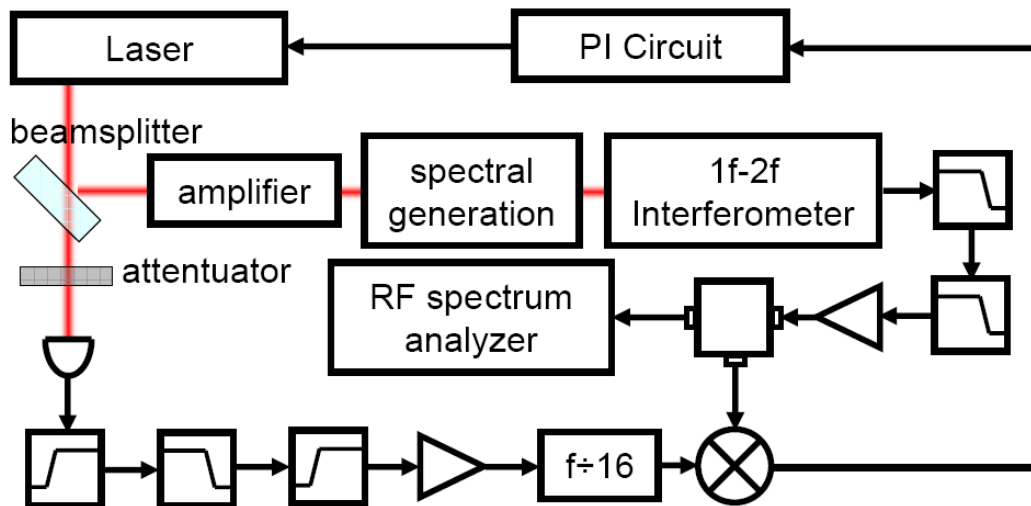


**Figure 5.** The carrier-envelope offset frequency locking system schematic.

Using the  $f_{ceo}$  beat, a locking system was constructed, as shown in Figure 5. Half of the fiber laser output power is attenuated and detected. The RF beat at the repetition rate is then isolated with RF filters, amplified, and divided by 16 to approximately 12.1 MHz. This frequency serves as the reference frequency for the phase-locked loop.

The remaining laser output power seeds the amplifier, which feeds the supercontinuum generation system, followed by the 1f-2f interferometer. The  $f_{\text{ceo}}$  beat is then isolated by RF filters and amplified, and serves as the controlled input to the phase-locked loop. The  $f_{\text{ceo}}$  beat is controlled by modulating the pump current. A bipolar junction transistor (BJT) is placed in parallel with the pump diode, and the error signal from the phase-locked loop drives the base port of the BJT. This effectively allows the drive current to be drawn away from the pump diode as needed to control the  $f_{\text{ceo}}$ . A Schottky diode is placed in parallel to the pump diode as well, with opposite polarity, in order to protect the pump diode from transients and excessive reverse biasing.

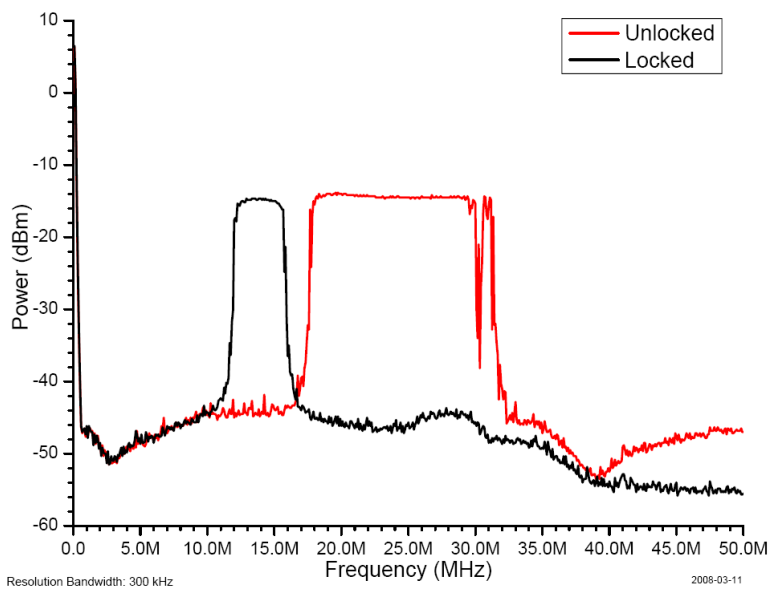


**Figure 6.** Variation of the beat signal over ten minutes when locked and unlocked.

To obtain a measure of the lock quality, the RF spectrum analyzer was set to record the highest value measured at each frequency. Figure 6 shows the resulting trace after ten minutes when  $f_{\text{ceo}}$  was locked (black) and when it was unlocked (red). The drift of the locked signal was due, in part, to the fact that the reference frequency was a fraction of the repetition rate, which was not locked. The lock was observed to be robust and stable for more than an hour, at which point it was turned off. The unlocked beat location was manually adjusted to be offset from the locking frequency and was lockable by merely turning on the feedback circuit, which demonstrates the locking range of the feedback phase detector.

Difference frequency generation can be used to generate a frequency comb with zero carrier-envelope offset frequency. Because of this, the repetition rate of the laser can be locked by beating the difference frequency product with a stable single-mode source. Using the supercontinuum shown in Figure 2, the difference frequency at  $3.39 \mu\text{m}$  was generated. To accomplish this, the interferometer shown in Figure 7 was used. The system generated the difference frequency of  $\lambda_{\text{high}} = 1082 \text{ nm}$  ( $277.3 \text{ THz}$ ) and  $\lambda_{\text{low}} = 1590 \text{ nm}$  ( $188.7 \text{ THz}$ ). The interferometer operated in the same way as the 1f-2f interferometer. The DFG was generated in a periodically-poled lithium niobate crystal, and then filtered by a  $40 \text{ nm}$  optical bandpass filter centered at  $3.39 \mu\text{m}$ .

A liquid-nitrogen-cooled InSb detector was used to detect the difference frequency. Figure 8 shows the generated DFG power as a function of relative interferometer path difference. The maximum DFG power observed was  $3 \mu\text{W}$ . Given the  $40 \text{ nm}$  ( $1.04 \text{ THz}$ ) bandwidth of the  $3.39 \mu\text{m}$  bandpass filter, approximately 5000 modes are represented by the total measured power,

giving a maximum power per mode of approximately 0.6 nW. The fact that blocking either path of the interferometer eliminates the signal further proves that the signal observed was the difference frequency.

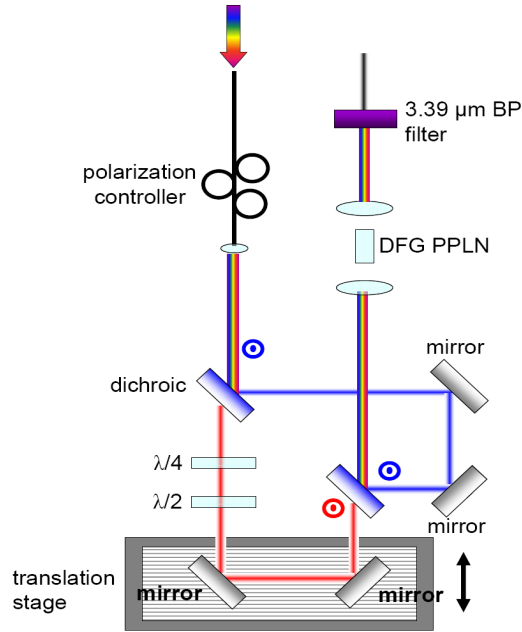


**Figure 7.** Schematic of the DFG interferometer.

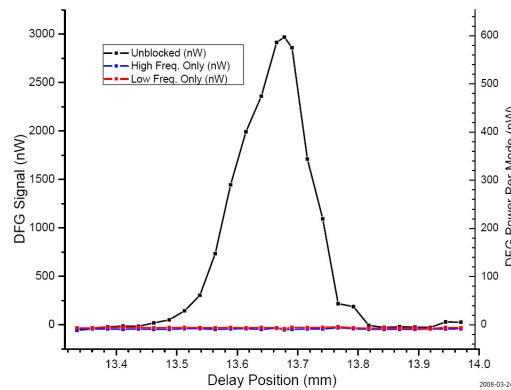


**Figure 8.** The difference frequency power at 3.39  $\mu\text{m}$  as a function of relative interferometer path difference. The curves show the unblocked output (black), and the output when the low frequency input (blue) and high frequency input (red) were blocked.

The difference frequency comb was then beat against a methane-stabilized HeNe laser. To generate the beat, the setup shown in Figure 9 was used. The difference frequency was spatially overlapped with the stabilized, single longitudinal mode output of the HeNe laser using a beam splitter. Each mode in the difference frequency comb beat with the 34  $\mu\text{W}$  HeNe mode and generated RF mixing products in the detector.

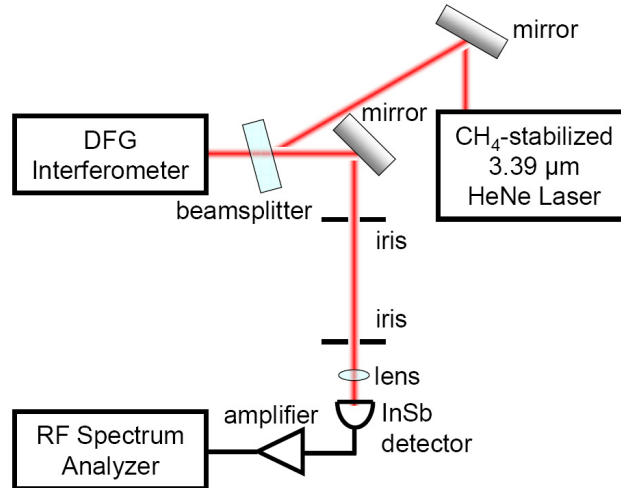


**Figure 9.** The setup for generating the DFG-HeNe beat.

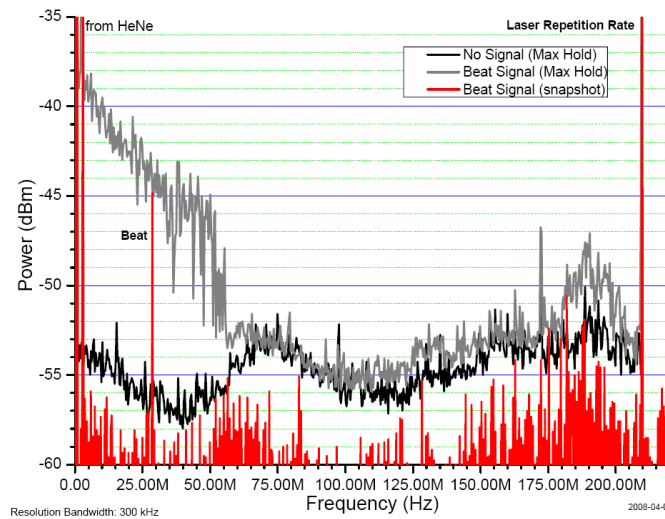


**Figure 10.** Beat between the difference frequency comb and the methane stabilized HeNe laser. For the black (no signal) and gray (beat signal) curves, the RF spectrum analyzer retained the highest observed value over the measurement time. The red curve shows a single-shot RF spectrum trace.

Figure 10 shows the resulting DFG beat data. A signal-to-noise ratio of 15 dB was observed out to the edge of the detector bandwidth at around 50 MHz. While 15 dB is not sufficient for locking, a comparison of the power levels to those found in experiments locking the repetition rate of a mode-locked Ti:Al<sub>2</sub>O<sub>3</sub> laser suggests that it can be done. Specifically, a HeNe discharge tube should be used to amplify the difference frequency signal, which should improve the signal-to-noise ratio.

Future work is directed toward increasing the average output power of the amplifier system to permit the direct amplification of higher rep rates and to increasing the stability of both frequency locks.

## **A High Repetition Rate Fundamentally Modelocked Sigma Erbium Fiber Laser**

### **Sponsors**

Office of Naval Research MURI, Contract N00014-02-1-0717  
Defense Advanced Research Projects Agency, Contract HR0011-05-C-0155  
Air Force Office of Scientific Research, Contract FA9550-07-1-0014

### **Project Staff**

Jason W. Sickler, Jonathan L. Morse, Professor Erich P. Ippen

Optical arbitrary waveform generation (OAWG) seeks to completely control the time-domain electric field. In the frequency domain, this means complete control of the amplitude and phase of the spectrum. One approach to achieving complete control of the spectrum is to begin with a periodic signal, such as that generated by a modelocked laser. A periodic signal's modes can be spatially separated by an arrayed waveguide-grating (AWG) and independently modulated in amplitude and phase to produce the arbitrary time-domain waveform.

The need to spatially separate the frequency components places restrictions on the source. As the laser repetition rate (i.e. the mode spacing) decreases, the spectral resolution of the AWG must increase. This leads to a larger AWG, more strict tolerances on waveguide path lengths, and the need for more waveguides for a given spectral bandwidth. Thus the mode-locked laser needs to have the highest possible repetition rate.

One approach to achieving a high repetition rate is to reduce the physical size of the cavity. However, as the cavity size is reduced, the per-pulse energy (both intracavity and output) decreases for the same average laser power. At some point, the intracavity pulse energy will not be sufficient to saturate the saturable absorber (or sustain another nonlinear modelocking mechanism), and the laser will no longer modelock.

The laser design discussed here seeks to reduce the cavity size, while still maintaining reasonably high average output powers. Figure 1 illustrates the system design. The laser is in a sigma configuration, so that a reflection point exists to allow for feedback control of the repetition rate. Saturable absorption is provided by a saturable Bragg reflector (SBR). The only fiber in the cavity is the erbium gain fiber with anomalous group velocity dispersion (GVD); the soliton effects of the fiber should ensure that the intracavity pulses will be near transform-limited at the saturable absorber, and thus saturation of the SBR will be maximized. The gain fiber is pumped through a short-wave-pass 980 nm/1550 nm dichroic mirror. The second dichroic allows remaining pump to exit the cavity, and the silicon ensures that no pump will interfere with SBR operation. The  $\lambda/2$  waveplate controls the output coupling at the polarization beam splitter (PBS). The vertically polarized (relative to the optical table) portion of the beam enters the sigma arm of the cavity, and is focused on the SBR with an aspheric lens. The sigma path includes a  $\lambda/4$  waveplate oriented so that the vertically polarized beam returns to the PBS horizontally polarized. After the PBS, the polarizing isolator ensures unidirectional operation. Finally,  $\lambda/2$  and  $\lambda/4$  waveplates allow control of the polarization state that is launched into the gain fiber.

The laser mode-locks at a repetition rate of 234 MHz. With optimization, a fundamental repetition rate of greater than 300 MHz should be achievable.

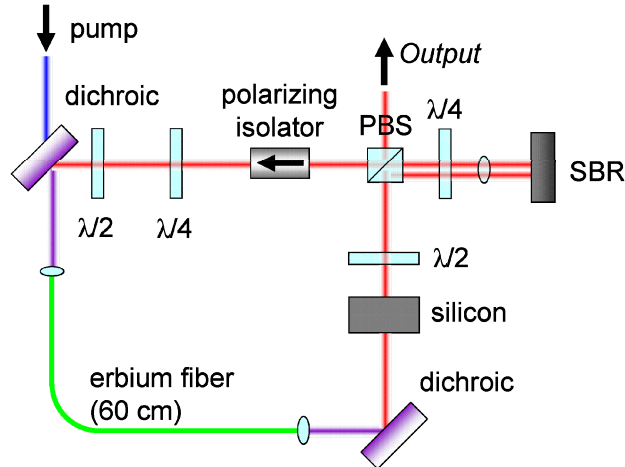


Figure 1. Short cavity mode-locked fiber laser approach.

The laser is self-starting and stably modelocks with several different SBR mirrors. Because the laser does not mode-lock when the SBR is replaced by a silver mirror, it is clear that the SBR at least enables self-starting. When the polarization launched into the gain fiber is in a linear state, mode-locking could not be achieved while using the SBRs, which indicates that polarization additive-pulse modelocking (P-APM) is also occurring.

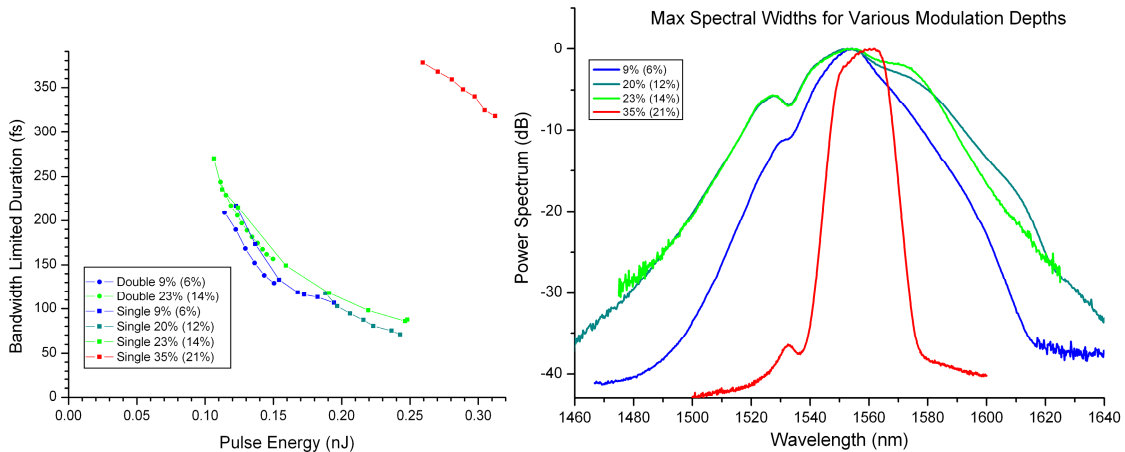
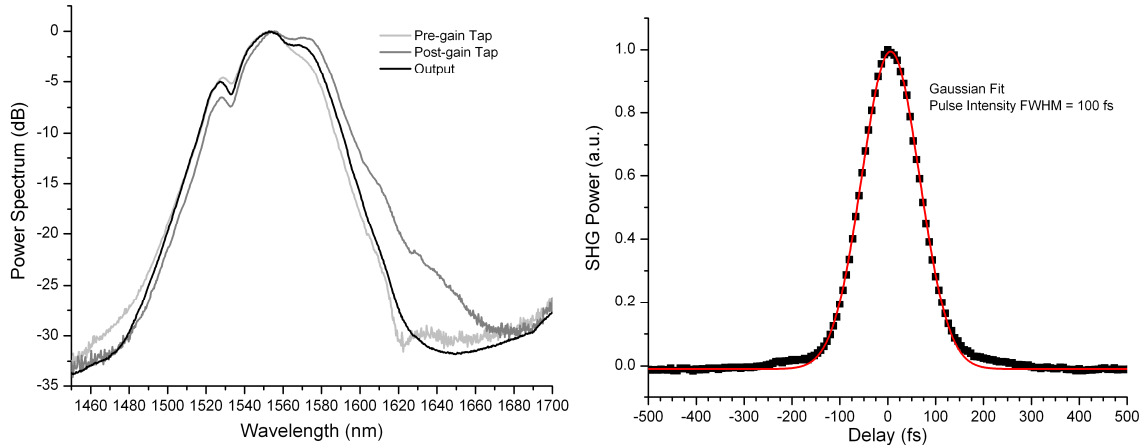


Figure 2. a) Bandwidth-limited pulse duration as a function of pulse energy. Single and Double refer to the number of intracavity pulses, and the linear loss and modulation depth of the SBR used are given. b) The broadest optical spectra using various SBRs.

Figure 2 shows the transform-limited pulse duration implied by the optical spectrum as a function of measured pulse energy. From this data, it appears that the modulation depth of the SBR does not affect pulse shaping because the results (with the exception of the highest modulation depth SBR) lie along the same contour. This indicates that pulse shaping is dominated by P-APM. Also, the 12% modulation absorber has a 12 ps recovery time, whereas the other SBRs have a 2 ps recovery time. The fact that these differences do not affect the pulse characteristics further supports that P-APM is shaping the final pulse.

Figure 2 also shows the maximum bandwidth optical spectra obtained with each SBR. From the absence of resonant sidebands, and the measured normal chirp on the output pulses, it is clear that the laser is operating in the stretched-pulse regime. The net GVD is  $-634 \text{ fs}^2$ , excluding any phase response of the SBR, so sub-100 fs pulses with moderate pulse energies should be expected, and are measured.

One will notice that the SBR with 21% modulation depth provides a distinctly different operating state. The square spectrum and higher pulse energies are consistent with a stretched-pulse laser with net normal GVD. The normal GVD contribution comes from the phase response of the SBR, which is dominated by the absorption resonance, and hence, increases with the strength of that resonance. Given that the location of the SBR band edge is at 1550 nm, the normal GVD contribution should be on the long wavelength side of the band edge. The location of the spectrum, relatively to the band edge, is consistent with these expectations.



**Figure 3.** a) OSA Trace, b) autocorrelation trace and Gaussian fit.

Figure 3 and Figure 4 provide a more complete characterization of the laser operation using the 14% modulation depth SBR. In Figure 3 the optical spectrum of the output port and (dichroic) tap ports before and after the gain fiber are shown. The Fourier transform of the optical spectrum corresponds to an 85.9 fs transform-limited pulse. The autocorrelation trace shows a compressed pulse duration of 100 fs after  $-16,253 \text{ fs}^2$  of GVD. A fit of the pulse duration as a function of external chirp compensation indicates an optimally compressed pulse of 90.1 fs using  $-18,047 \text{ fs}^2$  of GVD.

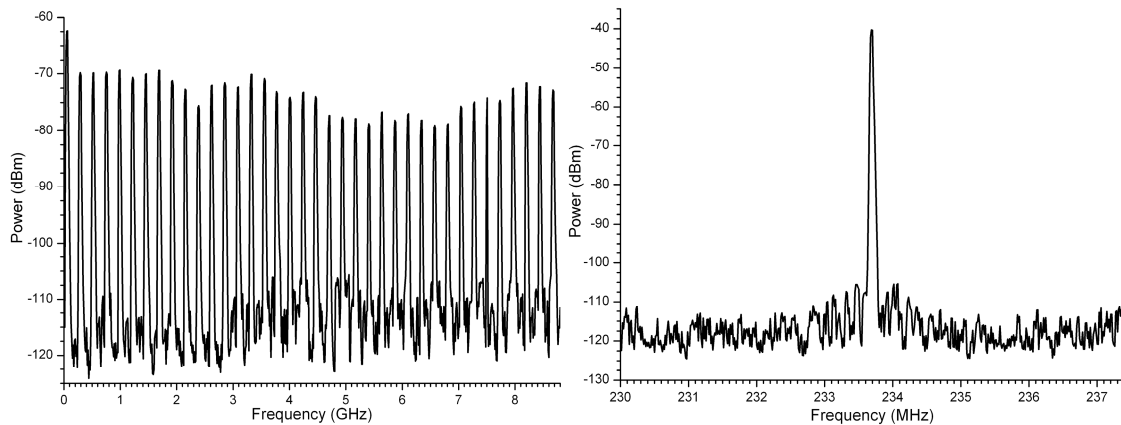


**Figure 4.** RF spectra showing a) smooth spectral envelope, indicating single-pulse operation, and b) showing a clean fundamental mode.

Figure 4 shows the RF spectrum of the laser output. The flat spectral envelope, combined with the smooth optical spectrum verifies single-pulse operation. In this state, the laser operates at a repetition rate of 234 MHz, a pulse energy of 246 pJ, a pulse duration full-width half-maximum of 100 fs, and an average output power of 57.6 mW.

## Ultrafast Phenomena and Quantum Electronics

### Stable Mode-Locked Pulses from Mid-Infrared Quantum Cascade Lasers

#### Sponsors

U.S. Army Research Office W911NF-07-1-0372

#### Project Staff

Vasileios-Marios Gkortsas, Dr Hyunyong Choi, Dr Ariel Gordon, Dr Christian Jirauschek, Christine Wang, Lyuba Kuznetsova, Professor Federico Capasso, Professor Theodore B. Norris and Professor Franz X. Kärtner

A stable train of short laser pulses in the mid-infrared wavelength range from mode-locked lasers is crucial for many applications such as nonlinear frequency conversion, time-resolved spectroscopy and frequency combs for optical metrology in this important wavelength range. The most common approach to generate short pulses in the mid-infrared rely on the down-conversion of short-wavelength mode-locked lasers through nonlinear processes. However, the complexity of these arrangements is a disadvantage. Mid-infrared Quantum Cascade Lasers could overcome this disadvantage due to the flexibility offered by bandgap engineering. Also multimode operation and modelocking phenomena of these lasers were already observed in 2000 [1], the fast gain recovery in quantum cascade lasers made it appear unlikely that stable short pulses are possible to be generated from these sources.

In this report, we present theoretical studies for the generation of a stable train of pulses from actively mode-locked QCLs employing diagonal transitions, such that the upper state lifetime of the laser transition approaches the cavity length. In that case, stable modelocking of these lasers, resulting in well separated pulses, may occur similar to what is known for the modelocking of conventional semiconductor and dye lasers due to the interplay between gain and loss over one roundtrip in the laser. Recently, active modelocking of these structures resulted in stable pulse trains, verified by the measuring the interferometric autocorrelation traces of the pulse trains indicating stable isolated pulses [2]. Here, we try to support these experimental findings by modeling the gain medium of QCLs as a two level system, described by the Maxwell-Bloch equations [3]. In our simulations the cavity length is 2 mm (corresponding to a cavity roundtrip time of 40 psec), the waveguide losses are  $10 \text{ cm}^{-1}$  and the mirror losses are 0.53 (amplitude). The upper state lifetime was chosen  $T_1=50 \text{ psec}$ , measured earlier for the diagonal intraband transitions, and the dephasing time is assumed to be 50 fsec. Thus the upper state lifetime of the laser transition is chosen somewhat longer than the cavity roundtrip time, and this situation impedes the formation of pulses through active mode-locking [3].

The laser is homogeneously pump over the full cavity length over threshold and in addition in a short, in our case 120  $\mu\text{m}$  long section, there is a sinusoidal modulation of the current with an amplitude 1.9 times above threshold with a frequency equal to the roundtrip frequency of the cavity. We simulated the laser for three different pump current levels 1.034, 1.18 and 1.32 times above threshold.

To compare with the experiment [2] pulses generated in our mode-locked QCLs are characterized using the interferometric autocorrelation. Figure 1 shows the interferometric autocorrelation obtained when the QCL is pumped 1.034 times above threshold and the sinusoidal modulation applied at the small section is 1.9 times above threshold. The observed peak-to-background ratio is 8:1, indicating that stable, isolated, mode-locked pulses are formed. As we increase the constant pumping along the cavity the peak-to-background ratio changes. In figure 2 the QCL is pumped 1.18 times above threshold while the modulation on the small section remains the same the peak-to-background ratio degrades to 8:2.5. In figure 3, where the constant pumping is 1.32 times above threshold the peak-to-background ratio becomes 8:5. From figures 2

and 3 we conclude that the modulation amplitude is not sufficient to suppress the continuous-wave lasing and the quality of the pulses deteriorated, no isolated Gaussian pulses are any longer generated. Qualitatively, this behavior agrees well with the experimental observations [2]. However, a more refined model is necessary to capture the laser dynamics quantitatively. So far, we have not included spatial hole burning in our model, which may play an important role as shown in [3].

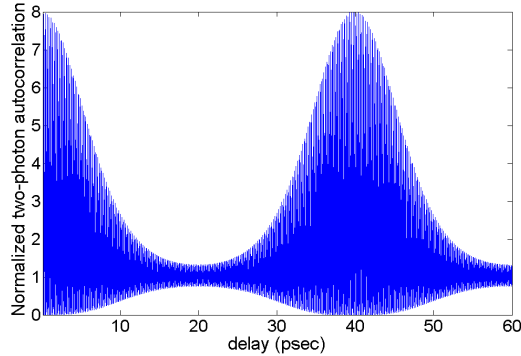


**Figure 1:** Autocorrelation trace when the QCL is pumped 1.034 times above threshold and a sinusoidal modulation 1.9 times above threshold is applied at the small section.

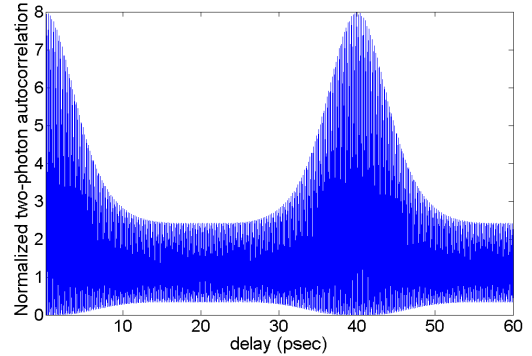


**Figure 2:** Autocorrelation trace when the QCL is pumped 1.18 times above threshold and a sinusoidal modulation 1.9 times above threshold is applied at the small section.

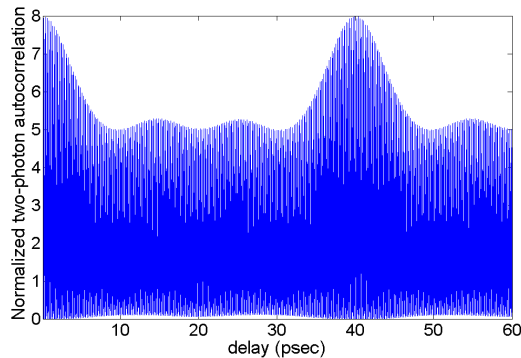


**Figure 3:** Autocorrelation trace when the QCL is pumped 1.32 times above threshold and a sinusoidal modulation 1.9 times above threshold is applied at the small section.

## References

- [1] Paiella, F. Capasso, C. Gmachl, D. L. Sivco, J. N. Baillargeon, A. L. Hutchinson, A. Y. Cho, and H. C. Liu, "Self-mode-locking in quantum cascade lasers with giant ultrafast optical nonlinearities," *Science*, vol. 290, pp. 1739–1742, (2000).
- [2] Ch. Y. Wang, L. Kuznetsova, L. Diehl, F. X. Kärtner, M. A. Belkin, H. Schneider, H. C. Liu and Federico Capasso, "Stable Mode-Locked Pulses from Mid-Infrared Quantum Cascade Lasers," *Conference on Lasers and Electro-Optics (CLEO)*, San Jose, CA, May 4-9, 2008.
- [3] A. Gordon, Ch. Y. Wang, L. Diehl, F. X. Kärtner, A. Belyanin, D. Bour, S. Corzine, G. Höfler, H. C. Liu, H. Schneider, T. Maier, M. Troccoli, J. Faist, and Federico Capasso, "Multimode regimes in quantum cascade lasers: from coherent instabilities to spatial hole burning," *Physical Rev. A* 75, 031802 (2007).

## Ultrafast nonlinear optical dynamics of high-power slab-coupled semiconductor optical waveguide amplifiers

**Sponsors:** Air Force Office of Scientific Research, Contract FA9550-07-1-0014

**Project Staff:** Ali Motamedi, Prof. Erich P. Ippen, Dr. Paul Juodawlkis

High power semiconductor optical amplifiers, in excess of 1W near 1.5 $\mu\text{m}$  are in demand for free space optical communication systems, optical array transmitters, and laser radar systems. One design approach to achieving such high powers is to increase the size of the optical mode, and the other is to decrease the overlap (confinement factor) between the optical mode and the active region of the device. Slab-coupled optical waveguide (SCOW) devices combine both of the above techniques to obtain devices with power in excess of 1W. SCOW topology has been utilized in the design of optical amplifiers[1] and CW[2] or mode-locked lasers[3].

Recent studies have demonstrated that two-photon absorption limits and causes deterioration of the maximum attainable output power of a SCOWA[4,5]. The low-confinement factor (<1%) increases the importance of nonlinearity in the passive waveguide relative to that of the gain saturation in the active region. In addition, since the two-photon absorption effect depends on peak power, whereas gain saturation depends principally on the optical energy within a population recovery time, the former imposes limitations on the output power in general and more severely when transmitting short pulses.

The pulse propagation through an active media can be described by

$$\frac{dI(z,t)}{dz} = I(z,t) [\Gamma g_m(z,t) - \alpha(z,t)], \quad (2)$$

where  $\Gamma$  is the confinement factor,  $I(z,t)$  is the peak intensity of the pulse,  $g_m(z,t)$  is the local material gain, and  $\alpha(z,t)$  is the local loss coefficient. A lower confinement factor requires a longer device and does not have the advantage of providing larger area for heat dissipation.

For pulses much shorter than the gain (carrier) recovery time, the local dynamic material gain,  $g_m(z,t)$ , can be determined from

$$g_m(z,t) = g_0 e^{-\int_{-\infty}^t d\tau I(z,\tau)/E_{sat}}, \quad (3)$$

where  $g_0$  is the unsaturated small signal gain and  $E_{sat}$  is the saturation density of the device. We note that the gain is not constant over the duration of the pulse and that this can result in pulse shape changes.

The loss,  $\alpha(z,t)$ , is a sum of several mechanisms:

$$\alpha(z,t) = \alpha_{TPA}(z,t) + \alpha_{2FCA}(z,t) + \alpha_{int} \quad (4)$$

The internal loss,  $\alpha_{int}$ , is a property of the constituent material and can be approximated to be uniform along the length of the device and independent of optical power. The two-photon loss is a

function of the incident intensity and is described by  $\alpha_{TPA}(z,t) = \beta' I(z,t)$ , where  $\beta'$  is related to  $\beta$ , the TPA coefficient by  $\beta' = \beta \frac{\iint I^2(x,y,z,t) dx dy}{I^2(z,t) \cdot A_{mode}}$ . For a Gaussian mode  $\beta' = \beta/2$ .

In addition to TPA loss, the free carriers generated by this process can further absorb energy from the incident beam. This free-carrier absorption (FCA) depends on the square of the intensity of the pulse and for pulses shorter than the carrier lifetime the FCA loss can be expressed

by  $\alpha_{2FCA}(z,t) = \int_{-\infty}^t \sigma' \frac{\beta I^2(z,\tau)}{\hbar\omega} d\tau$ , where  $\hbar\omega$  is the incident photon energy. The effective

FCA cross-section  $\sigma'$  used in this expression is related to the plane wave cross section  $\sigma$  by

$$\sigma' = \sigma \frac{\iint I^3(x,y,z,t) dx dy}{I^3(z,t) \cdot A_{mode}}. \text{ For a Gaussian mode profile } \sigma' = \sigma/3.$$

The device used in this study is an InGaAsP/InP slab-coupled optical waveguide amplifier with a  $5 \times 7 \mu\text{m}$  fundamental mode size resulting in an effective area of  $13.75 \mu\text{m}^2$ . The active region of this device is made up of five 8nm compressively strained quantum wells with composition yielding a peak photoluminescence at  $1530 \mu\text{m}^2$ . The confinement factor of this device is determined to be 0.5%.

To study the gain dynamics of this device using different pulsewidths, an optical parametric oscillator (OPO) operating at 1540nm was utilized. The OPO pulses are 150fs long at a repetition rate of 80MHz. They were stretched to pulsewidths ranging from 1.4ps to 40ps using an optical filter and a double-pass grating pair. The device was biased at 4A, and the gain of the device was measured as the function of the input pulse energy, and the results are shown in Figure 1.

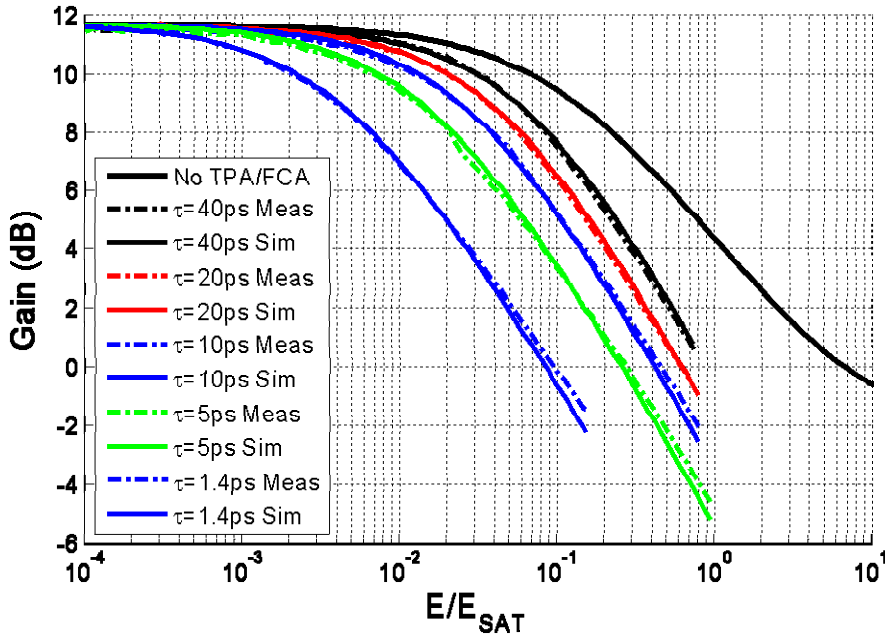


**Figure 1.** Net gain of the SCOWA vs. input pulse energy for different pulsewidths.  $I_{bias}=4A$ .  $E_{sat}$ , determined from the curve fitting is 360fJ.

The solid lines are fits to the measured data using the model as described above. These results show that the 3dB gain roll off moves to lower energies as the pulse duration is decreased. This can be attributed to the effects of the TPA and FCA losses which are proportional to the intensity and the square of the intensity of the pulse, respectively. The small deviations between the simulated results are most likely due to the pulse shaping in the amplifier due to self-phase modulation and dispersion as well as dynamic gain saturation. The above simulated results are obtained using unsaturated gain  $g_0 = 640/\text{cm}$ , confinement factor  $\Gamma = 0.5\%$ , material loss  $\alpha_{\text{int}} = 0.5\text{cm}^{-1}$ , FCA effective cross section  $\sigma = 7 \times 10^{-17} \text{ cm}^2$ , saturation energy,  $E_{\text{sat}} = 1.4\text{mJ}/\text{cm}^2$ , and TPA coefficient,  $\beta$  of  $65\text{cm}/\text{GW}$ . The resulting TPA coefficient of  $65\text{cm}/\text{GW}$  is in close agreement with the calculation of the TPA coefficient based on its dependence on the inverse cube of the bandgap energy[7] and the TPA coefficient of InP as reported in[8]. The FCA effective cross section,  $\sigma$  is in close agreement to the value reported in[5].

### References:

- [1] P. W. Juodawlkis, J. J. Plant, R. K. Huang et al., "High-power 1.5- $\mu\text{m}$  InGaAsP-InP slab coupled optical waveguide amplifier," *IEEE Photonics Technology Letters* **17** (2), 279-281 (2005).
- [2] J. J. Plant, P. W. Juodawlkis, R. K. Huang et al., "1.5- $\mu\text{m}$  InGaAsP-InP slab-coupled optical waveguide lasers," *IEEE Photonics Technology Letters* **17** (4), 735-737 (2005).
- [3] S. Gee, F. Quinlan, S. Ozharar et al., "Ultralow-noise mode-locked optical pulse trains from an external cavity laser based on a slab coupled optical waveguide amplifier (SCOWA)," *Optics Letters* **30** (20), 2742-2744 (2005).
- [4] Jason J. Plant, Juliet T. Gopinath, Bien Chann et al., "250 mW, 1.5 $\mu\text{m}$  monolithic passively mode-locked slab-coupled optical waveguide laser," *Opt. Lett.* **31** (2), 223-225 (2006).
- [5] Paul W. Juodawlkis, Jason J. Plant, Joseph P. Donnelly et al., "Continuous-wave two-photon absorption in a Watt-class semiconductor optical amplifier," *Opt. Express* **16** (16), 12387-12396 (2008).
- [6] F. R. Ahmad, Tseng Yen Wei, M. A. Kats et al., "Energy limits imposed by two-photon absorption for pulse amplification in high-power semiconductor optical amplifiers," *Optics Letters* **33** (10), 1041-1043 (2008).
- [7] E. W. Van Stryland, M. A. Woodall, H. Vanherzeele et al., "Energy band-gap dependence of two-photon absorption," *Optics Letters* **10** (10), 490-492 (1985).
- [8] A. M. Darwish, E. P. Ippen, H. Q. Le et al., "Short-pulse wavelength shifting by four wave mixing in passive InGaAsP/InP waveguides," *Applied Physics Letters* **68** (15), 2038-2040 (1996)

## Femtosecond Laser Fabrication

### Sponsors

National Science Foundation – ECS-0501478, BES-0522845

Air Force Office of Scientific Research – FA9550-040-1-0011, FA9550-07-1-0101

### Project Staff

Prof. James G. Fujimoto, Dr. Jung-Ho Chung, Yu Gu.

Since its first demonstration [1], direct writing of waveguide devices using femtosecond laser pulses has become a powerful and versatile technique for fabrication of photonic devices. Localized index modification enables the fabrication of three-dimensional structures and has the potential for creating high-density integrated photonic circuits, thus providing enhanced functionality not possible in planar geometries. In contrast to the conventional semiconductor-based fabrication process, the micromachining process is a single step process, allowing for rapid construction of a variety of devices. Various structures have been fabricated via direct writing using femtosecond lasers. They include a wide variety of planar devices such as several types of couplers, interferometers, and active waveguides, but also three-dimensional structures, such as optical splitters [2], interconnects, wavelength-division multiplexing couplers, and directional couplers [3,4]. For telecommunication and sensing applications, it is important to fabricate reproducible and reliable basic elements such as splitters, couplers, and interferometers. Via direct writing using a multi-pass cavity (MPC) Ti:Sapphire laser [5], we demonstrate the femtosecond laser fabrication of symmetric directional couplers and unbalanced Mach-Zehnder interferometers and the observation of their wavelength characteristics.

## 2. Femtosecond Laser Waveguide Fabrication and Measurement

Because waveguide properties such as mode size and index of refraction are sensitive to both the exposure power and scanning speed, it is important to explore the threshold for high-speed femtosecond laser waveguide fabrication. To this end, our group developed a specialized light source, which is a novel, Multiple-pass Cavity (MPC) mode-locked Ti:AlO<sub>3</sub> laser [5]. Figure 1 shows the schematic of the MPC laser. The MPC laser generates 45 fs duration pulses with maximum of 150 nJ of energy per pulse at 5.85 MHz. In contrast to amplified femtosecond systems, the MPC laser has a repetition rate high enough to produce a cumulative heating effect which enables device fabrication approximately three orders of magnitude faster than possible using amplified systems [6]. The cumulative heating effect results in symmetric waveguide cross-sections, and the relatively high pulse energy enables fabrication to be performed with fewer constraints on the numerical aperture.

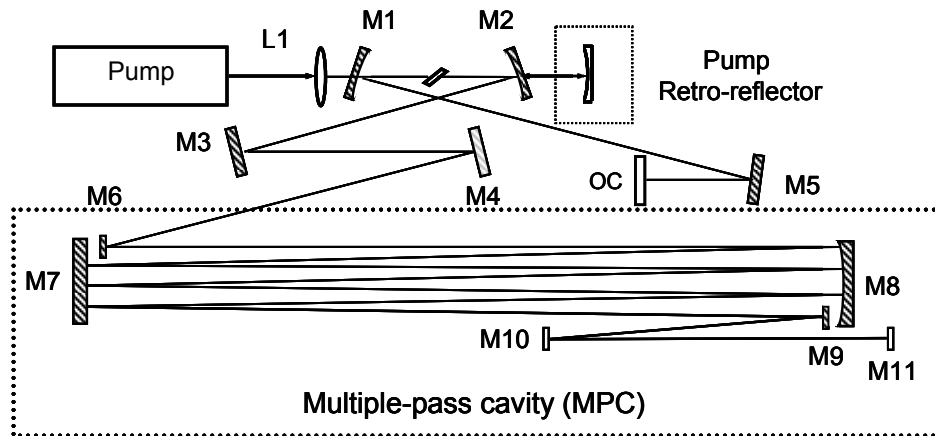
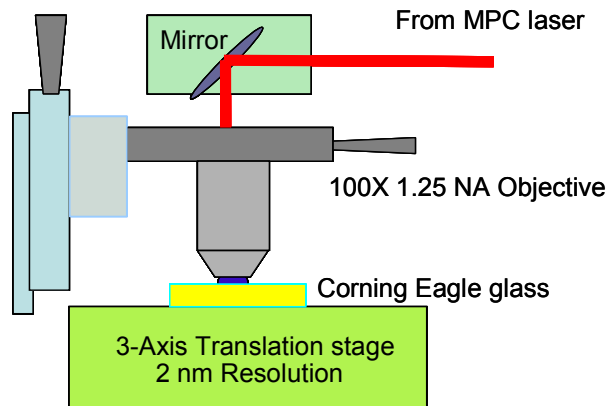


Figure 1. Schematic of MPC laser [5]. M7 and M8 make up the extended cavity.

Waveguides are fabricated in Corning EAGLE<sup>2000</sup> glass by translating the substrate transverse to writing direction using a high-precision air-bearing 3 axis stage. The output from the MPC Ti:Sapphire oscillator is attenuated so the exposure at the sample is around 120 mW, then focused with a 1.25 NA oil-immersion lens onto the substrate. The writing speed is set at 12 mm/s. To perform characterization, input and output facets are polished, and light from a tunable laser source (1500 to 1600 nm) is coupled into the devices using single-mode fiber. Index matching oil is used to minimized losses at the output and input interfaces. In all measurements, power is normalized against fiber-to-fiber coupling. Figure 2 shows the fabrication setup, and Figure 3 shows a phase-contrast microscope image of a laser fabricated waveguide. After fabrication, characterization is performed by coupling light from a SMF into the polished facet of the sample. Reported output power is normalized against output power from fiber-to-fiber coupling.



**Figure 2.** Schematic of fabrication setup. The glass substrate is mounted on an air-bearing 3 axis translation stage. The laser beam is focused using a high NA, immersion objective.



**Figure 3.** Phase contrast microscope image of a laser fabricated waveguide.

## References

- [1] K.M. Davis, K. Miura, N. Sugimoto, and K. Hirao, "Writing waveguides in glass with a femtosecond laser," *Optics Letters*, vol. 21, pp. 1729-31, 1996.
- [2] J. R. Liu, Z. Y. Zhang, S. D. Chang, C. Flueraru, and C. P. Grover, "Directly writing in fused of 1-to-N optical waveguide power splitters silica glass using a femtosecond laser," *Optics Communications*, vol. 253, pp. 315-319, 2005.
- [3] K. Minoshima, A. M. Kowalevich, E. P. Ippen, and J. G. Fujimoto, "Fabrication of coupled mode photonic devices in glass by nonlinear femtosecond laser materials processing," *Opt. Express*, vol.10, pp.645-652, 2002.

- [4] S.M. Eaton, W. Chen, L. Zhang, H. Zhang, R. Iyer, J.S. Aitchison, and P.R. Herman, "Telecom-band directional couplers written with femtosecond fiber laser," *Photonics Technology Letters*. 18, pp. 2174-2176, 2006.
- [5] A. M. Kowalewicz, A. T. Zare, F. X. Kartner, J. G. Fujimoto, S. Dewald, U. Morgner, V. Scheuer, and G. Angelow, "Generation of 150-nJ pulses from a multiple-pass cavity Kerr-lens mode-locked Ti : Al<sub>2</sub>O<sub>3</sub> oscillator," *Optics Letters*,. Vol. 28, pp.1597-1599, 2003.
- [6] S.M. Eaton et al. "Heat accumulation effects in femtosecond laser-written waveguides with variable repetition rate," *Optics Express* ,vol.13, pp. 4708-4716, 2005.

### 3. Femtosecond Laser Fabrication of Directional Couplers

Directional couplers are an essential and basic building block in photonic devices. In the past few years, there has been work in both two dimensional [1,2] as well as three-dimensional directional couplers and splitters [3,4]. In particular, our group has demonstrated the fabrication of asymmetric directional couplers with an extended cavity Ti: Sapphire oscillator [1]. Thru and cross port coupling ratios were measured while varying the interaction length and separation distance. Liu et al demonstrated symmetric 1x2 and 2x2 laser fabricated directional couplers optimized for 3dB operation at 1.5  $\mu\text{m}$  and used multi-scanning to reduce losses in s shaped bends [2]. In addition, telecom-band couplers with low loss(0.3 dB/cm), periodic dependence on interaction length and high extinction ratios have been demonstrated [5].

We fabricated and studied the wavelength characteristics of symmetric directional couplers with varying interaction lengths and show that their wavelength dependence can be tailored by controlling the physical parameters of the devices such as interaction length and radius of curvature in the bends. Observing the wavelength-dependent behavior of a directional coupler allows for comparison with coupled mode theory without errors resulting from taking data points from multiple devices. Figure 4 shows the geometric layout of the directional coupler. The separation is labeled S. x and R mark the centers and radii of curvature, respectively, of curved segments. The fields in the two ports are assigned to be A and B.

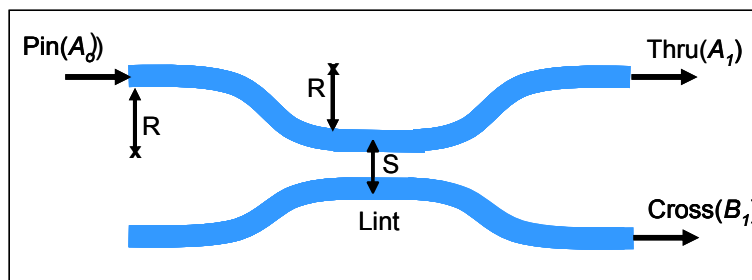


**Figure 4.** Geometric layout of the symmetric directional coupler. The coupler has straight segments connected by S-shaped curves consisting of two circular pieces placed adjacent to each other. The center to center waveguide separation in the interaction region, S, is set at 5  $\mu\text{m}$ . The interaction length parameter Lint is varied between 0 and 14 mm for a series of fifteen couplers.

The use of curved waveguides reduces losses from sharp changes in waveguide direction. However, bent waveguides are observed to exhibit a wavelength-dependent loss which is greater at longer wavelengths and smaller at shorter wavelengths. The value of the loss in bent waveguides has also been observed to increase nonlinearly with decreasing bend radius [6,7]. To reduce bending losses and wavelength-dependent loss, the radius of curvature in the S-shaped bends is limited to 125 mm. A relatively small waveguide separation (5  $\mu\text{m}$ ) is chosen to

reduce errors which may result in propagation constant mismatch. The interaction length parameter  $L_{int}$  is varied between 0 and 14 mm.

With degenerate coupling, solutions of coupled-mode equations yield intensities which are sinusoidal squared [8]:

$$\begin{aligned} |A_1(z)|^2 &= |A_0|^2 \cos^2(\kappa z) \\ |B_1(z)|^2 &= |B_0|^2 \sin^2(\kappa z) \end{aligned} \tag{1}$$

Here the coupling coefficient  $\kappa$ , describes the overlap between modes  $\varepsilon_a$  and  $\varepsilon_b$  of adjacent waveguides.

$$\kappa \propto \int NA^2 \varepsilon_a(x) \varepsilon_b(x) dx \tag{2}$$

To characterize the fabricated couplers, light is coupled into one arm of the device ( $A_0$ ) and the thru ( $A_1$ ) and cross port ( $B_1$ ) output powers are measured. Figure 5 from ref [9] shows the output powers from directional couplers with interaction lengths of 4 mm (a) and 14 mm (b), as well as theoretical curves for each port. Output powers are calibrated against fiber-to-fiber coupling.

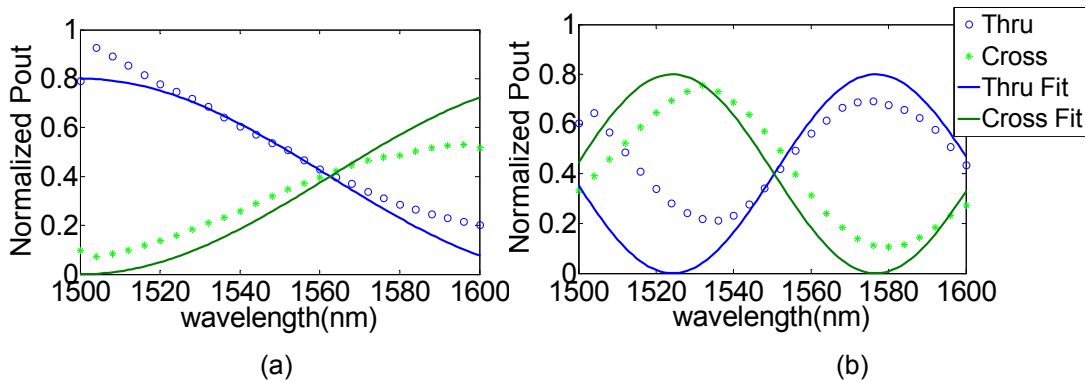


**Figure 5.** Spectral data and theoretical fits of thru and cross ports from directional couplers with interaction length parameters of (a) 6 mm and (b) 14 mm. The theoretical fits can be used to estimate the coupling constant [9].

Since the argument  $\kappa z$  changes with wavelength, the couplers have wavelength dependent behavior. As expected, thru and cross port powers show less wavelength variation for shorter interaction lengths and vary sinusoidally for long interaction lengths. Therefore, different interaction lengths can be used to tailor the wavelength characteristics. The contrast ratio does not reach 1 due to a finite mismatch in propagation constants, possibly from adjacent waveguides not being identical in size or errors in  $z$  position between waveguides. Theoretical fits for all fifteen devices were used to yield an estimate for the interaction parameter.

To enable the building of more complex devices, it is ideal to obtain couplers which act as wavelength-independent splitters. Ideal 3 dB couplers split the field strength and create a  $\pi/2$  phase shift in one arm. To create an ideal 3 dB coupler, the coupling coefficient  $\kappa$  should vary as little as possible across the desired wavelength range. This can be accomplished by fabricating waveguides as close together as possible without overlapping. In addition, the shortest possible interaction length is used to minimize the value of  $\kappa z$ . The radius of curvature of waveguides in bend portions must also be appropriately chosen to both minimize the effective interaction length and also minimize the effect of wavelength-dependent losses. Figure 6 shows the normalized thru and cross port data of a coupler which has been optimized for wavelength-independent 3 dB coupling. It has 125 mm radius of curvature in bent segments, 0.15 mm  $L_{int}$  and 5  $\mu\text{m}$  interaction separation. It can be seen that the coupling ratio is close to 1:1 for all wavelengths, but there remains a nonzero wavelength dependence of the total powers of a few percent. To further optimize the coupler, both the radius of curvature and the interaction parameters can be adjusted.

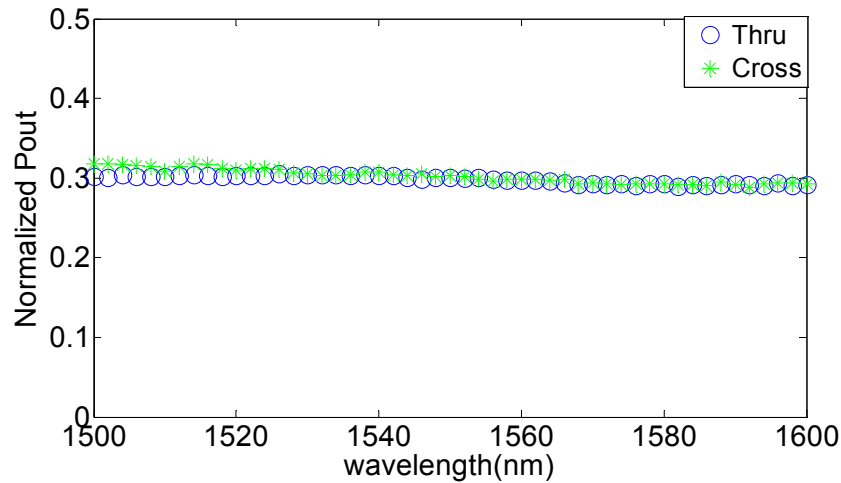


**Figure 6.** Normalized thru and cross port spectral data for a directional coupler optimized for wavelength-independent 3 dB operation. Lint is 0.15 mm. Interaction separation is 5  $\mu\text{m}$ . The radius of curvature of bent waveguides is 125 mm.

- [1] K. Minoshima, A. M. Kowalevich, I. Hartl, E. P. Ippen, and J. G. Fujimoto, "Photonic device fabrication in glass by use of nonlinear materials processing with a femtosecond laser oscillator," *Optics Letters*, vol. 26, pp. 1516-18, 2001.
- [2] J. Liu, Z. Zhang, S. Chang, C. Flueraru, and C.P. Grover, "Fabrication and optimization of one-to-two and two-to-two optical directional couplers in glass using a femtosecond laser," *Photonics North*, 2004.
- [3] S. Nolte, M. Will, J. Burghoff, and A. Tunnermann, "Ultrafast laser processing: new options for three-dimensional photonic structures," *Journal of Modern Optics*, vol. 51, pp. 2533-2542, 2004.
- [4] K. Suzuki, V. Sharma, J. G. Fujimoto, and E. P. Ippen, "Characterization of symmetric [3x3] directional couplers fabricated by direct writing with a femtosecond laser oscillator," *Optics Express*, vol. 14, pp. 2335-2343, 2006.
- [5] S. M. Eaton, W. Chen, L. Zhang, H. Zhang, R. Iyer, J. S. Aitchison, and P. R. Herman, "Telecom-band directional coupler written with femtosecond fiber laser," *IEEE Photonics Technology Letters*, vol. 18, pp. 2174-6, 2006.
- [6] M. Heiblum, and J. H. Harris. "Analysis of Curved Optical Waveguides by Conformal Transformation." *Journal of Quantum Electronics*. vol. QE-11, pp. 75-83, 1975.
- [7] K.R. Hiremath. M. Hammer, R. Stoffer, L Prkna, and J. Ctyroky. "Analytic approach to dielectric optical bent slab waveguides." *Optical and Quantum Electronics*, vol 37, pp.37-61, 2005.
- [8] K. Okamoto. Fundamentals of Optical Waveguides. Elsevier, Burlington, 2006.
- [9] Y. Gu, J. H. Chung, and J. G. Fujimoto, "Femtosecond laser fabrication of directional couplers and Mach-Zehnder interferometers," *Conference on Lasers and Electro-Optics*, Baltimore, MD, 2007.

#### 4. Femtosecond Laser Fabrication of Mach-Zehnder Interferometers(MZI)

Several groups have demonstrated the fabrication of Mach-Zehnder interferometric devices as well as their functionality. In earlier work, our group has demonstrated a femtosecond laser fabricated Mach-Zehnder Interferometer consisting of two X couplers placed back-to-back which shows expected interferometric fringes [1]. Groups have also demonstrated high extinction MZI which can be tuned through additional femtosecond exposure, or "trimming" [2,3]. In addition, laser fabricated Mach-Zehnder devices have been shown to have possible applications as heat

sensors [4] and Electro-Optic switches [5]. However, it has not been shown that these devices can be designed to function over larger wavelength ranges, on the order of 100 nm for example. The first aim of the Mach-Zehnder project is to demonstrate femtosecond laser fabricated MZI that function at the telecom wavelength and exhibit desirable properties such as high extinction ratio and tunability over 100 nm.

Couplers optimized for 3dB splitting and relative wavelength-independence were used to build an unbalanced MZI. Figure 7 shows the layout. X and R show the centers and radii of curvature for the bottom arm. Unbalance in arm lengths is created by using a longer segment of bent waveguide on the bottom arm while keeping the radius of curvature constant. The total arm lengths could also be changed by varying the straight waveguide region L.

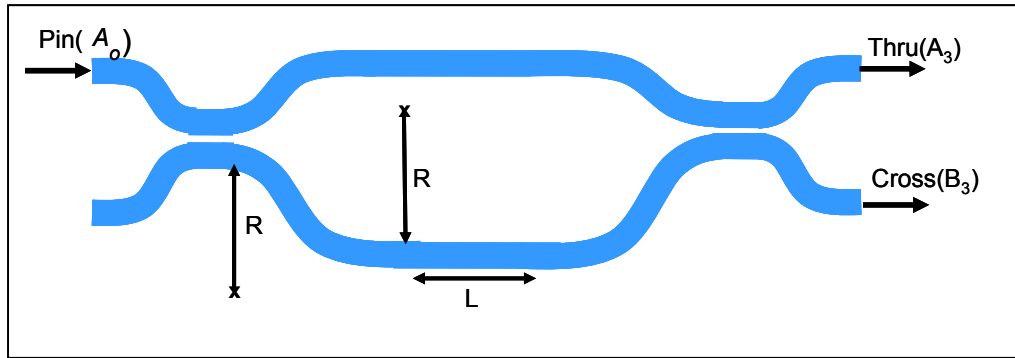


**Figure 7.** Schematic of unbalanced Mach-Zehnder interferometer. L is the straight portion of both arms. Unbalance is created by extending the length of the bent portion of the bottom arm.

From theory, the intensities of thru and cross ports oscillate as functions of the phase difference between the two arms, which is the product of the propagation constant  $\beta$  and the path length unbalance  $dL$ .

$$\begin{aligned} |A_3|^2 &= |A_0|^2 \sin^2\left(\frac{\varphi}{2}\right) \\ |B_3|^2 &= |A_0|^2 \cos^2\left(\frac{\varphi}{2}\right) \\ \varphi &= \beta \cdot dL \end{aligned} \quad (3)$$

With change in wavelength, the thru port power is expected to oscillate as a result of the variation of  $\varphi$ . Figure 8 shows the thru port output characteristics of a Mach-Zehnder device fabricated with path length differences  $dL$  of 25.6  $\mu\text{m}$ . As expected, the thru and cross port intensities vary as squared sinusoids. The extinction ratio is also observed to be high.

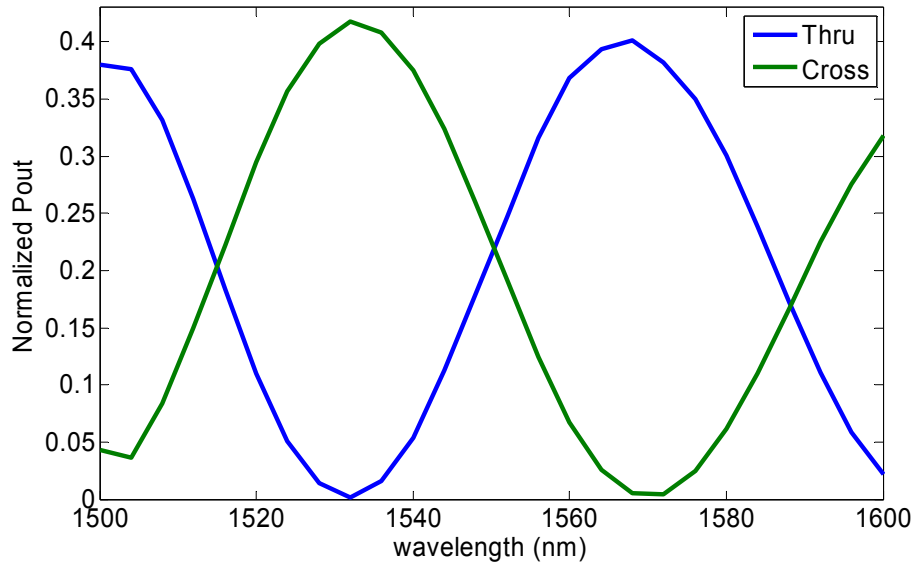


**Figure 8.** Spectral data of unbalanced Mach-Zehnder interferometers with unbalance of 25.6  $\mu\text{m}$ .

Using the known path-length unbalances, a theoretical fit was performed for each set of spectral data, and the propagation constant  $\beta$  at 1550 nm was estimated. There is some variation between the propagation constant calculated for each device since there is some fabrication error. Since the fabrication power has typical fluctuation of 1-2 mW and waveguides properties are expected to be nonlinearly dependent on it, this may be a major source of error. The stage position has finite error on the order of 10 nm, so this is expected to be small.

Since material interaction is mediated by nonlinear effects, there is strong dependence of waveguide properties such as index of refraction and mode size on writing parameters, such as power and speed. Of particular interest is the characterization of waveguide propagation constant as a function of writing parameters. We used laser fabricated MZI to study the dependence of propagation constant on scanning speed. Mach-Zehnder devices were fabricated with a fixed arm length unbalance and a different writing speed (speed2) in the straight portion of the lower arm, as shown in Figure 9. To reduce unbalanced loss, both arms were fabricated with the same radius of curvature.

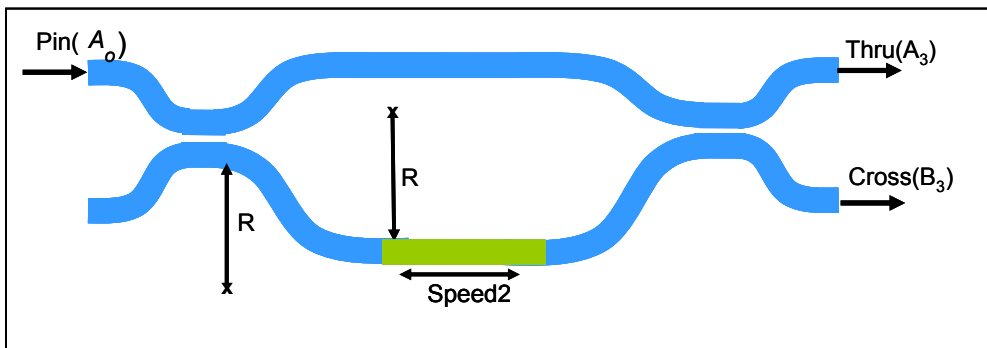


**Figure 9.** Unbalanced Mach-Zehnder interferometer with change of speed in bottom arm. The green segment indicates the length of waveguide written with changed speed parameter speed2.

For small perturbations, the change in the propagation constant can be found by observing the shift in the phase of the spectral dependence. If the thru port of the unperturbed device has

output wavelength characteristics according to Eq. (6), then the Mach-Zehnder with the perturbed writing speed has thru port spectral dependence characterized by a phase shift:

$$|A_3|_{new}^2 = |A_0|^2 \sin^2\left(\frac{\varphi_1}{2} + \Delta\varphi\right) \tag{4}$$

where  $\varphi_1$  is the original phase difference between the two arms

Working through calculations, the change in propagation constant in units of ( $m^{-1}$ ) is found to be

$$\Delta\beta = -\frac{\Delta\varphi}{L} \tag{5}$$

where  $L$  is the length of the waveguide with speed2.

When taking spectral data, the shift in phase of the periodic spectral dependence is used to back calculate the change in propagation constant. Figure 10 shows an example of spectral data from two devices fabricated with different speeds in the bottom arm.

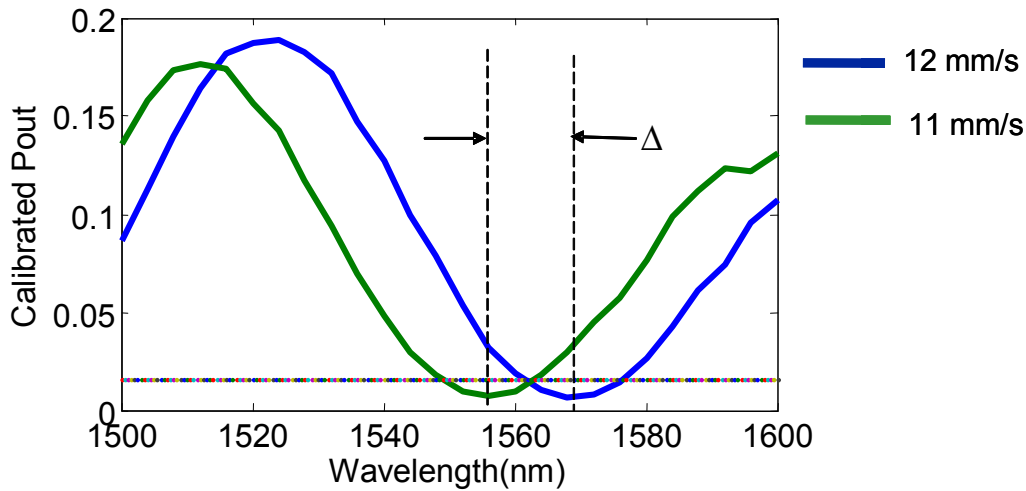


**Figure 10.** Spectral data from Mach-Zehnder device with two different writing speeds in the straight portion of bottom arm. The first device (blue) is written entirely with 12 mm/s, while the second device (green) is written at 11 mm/s in the straight portion of the bottom arm. The spectral shift is used to find the change in propagation constant from the reduced writing speed.

One significant issue in making the measurement of change in propagation constant with writing speed is the repeatability of identical devices. To make a statistically significant calculation in the change of propagation constant with writing speed, the variance in the maxima and minima positions of the spectral characteristics of MZ devices with identical structures must be small enough to provide a reliable comparison between MZ devices with different speed2. This can possibly be minimized by fabricating at a larger power to reduce the relative affect of power fluctuation. Another way to reduce the effect of finite repeatability is to fabricate multiple identical devices.

In conclusion, we demonstrate the fabrication and measurement of the spectral characteristics of femtosecond laser fabricated directional couplers from 1500 nm to 1600 nm. Thru and cross port powers show less wavelength variation for shorter interaction lengths and vary sinusoidally for long interaction lengths. Therefore, the wavelength characteristics can be tailored by changing the physical parameters. The successful fabrication and characterization of unbalanced Mach-Zehnder interferometers from 1500 nm to 1600 nm has also been demonstrated. The sinusoidal behavior of Mach-Zehnder interferometers was used to estimate the value of the waveguide propagation constant. In addition, Mach-Zehnder devices with a changed writing

speed in one arm are being used to characterize the dependence of propagation constant on writing speed.

### References

- [1] K. Minoshima, A. M. Kowalevich, E. P. Ippen, and J. G. Fujimoto, "Fabrication of coupled mode photonic devices in glass by nonlinear femtosecond laser materials processing," *Optics Express*, vol. 10, pp. 645-652, 2002.
- [2] C. Florea and K. A. Winick, "Fabrication and characterization of photonic devices directly written in glass using femtosecond laser pulses," *Journal of Lightwave Technology*, vol. 21, pp. 246-253, 2003.
- [3] P. Bado, "Manufacturing of High Quality Integrated Optical Components by Laser Direct-Write," *International Congress on Applications of Lasers and Electrooptics(ICALEO)*, 2003.
- [4] Y. Pin, G. Junpeng, G.R. Burns, and L. Ting Shan, "Direct-write embedded waveguides and integrated optics in bulk glass by femtosecond laser pulses," *Optical Engineering*. Vol 44, pp. 51104-1, 2005.
- [5] G. Li, K.A. Winick, Ali Said, M. Dungan, and P. Bado, "Waveguide electro-optic modulator in fused silica fabricated by femtosecond laser direct writing and thermal poling," *Optics Letters*, vol. 31, pp. 739-41, 2006.
- [6] Y. Gu, J. H. Chung, and J. G. Fujimoto, "Femtosecond laser fabrication of directional couplers and Mach-Zehnder interferometers," *Conference on Lasers and Electro-Optics*, Baltimore, MD, 2007.
- [7] M. Popovic. E. Ippen and F.X. Kartner, "Universally balanced photonic interferometers," *Optics Letters*, vol. 31, pp. 2713-15, Sept. 2006.

## Attosecond Science

### Broadband Optical Parametric Chirped Pulse Amplification

#### Sponsors

Air Force Office of Scientific Research (“DARPA HRS”) FA9550-06-1-0468  
MIT Lincoln Laboratory 7000013535  
Rocca Foundation

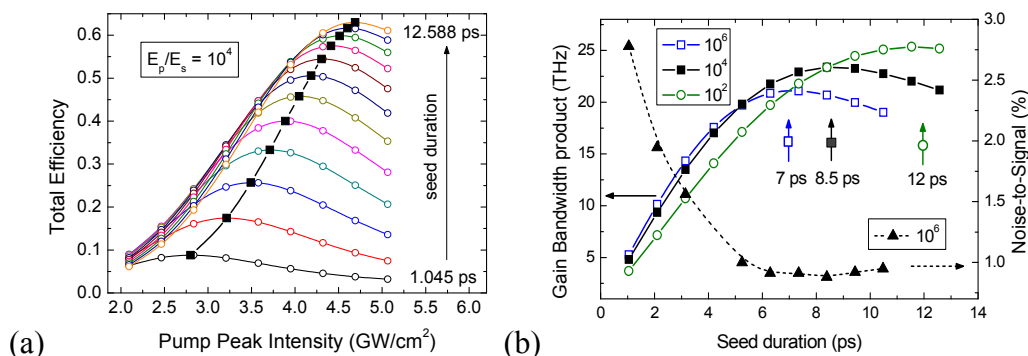
#### Project Staff

Dr. Jeffrey Moses, Shu-Wei Huang, Giovanni Cirimi, Dr. Kyung-Han Hong, Dr. Edilson L. Falcão-Filho, A. Benedick, J. R. Birge, Cristian Manzoni, Prof. Giulio Cerullo, and Prof. Franz X. Kärtner,.

Today’s demands on light sources for high-intensity ultrafast optics research are stringent: peak power must be maximized by scaling both to high energy and near-single-cycle duration, signal to noise contrast must be high, and often pulses at nontraditional wavelengths must be generated. These requirements have led to the rapid development of ultrabroadband optical parametric chirped pulse amplification (OPCPA) pumped by powerful picosecond pulses, in which gain bandwidth is stretched to near-octave breadths by group-velocity matching between signal and idler. Our group has been studying the optimization problem of an ultrabroadband OPCPA and developing few-cycle OPCPAs at 800 nm and 2  $\mu\text{m}$  that will eventually be used as the driving sources for high harmonic generation experiments.

In recent years, several problems in the construction of these amplifiers have become relevant. The coupling of temporal gain narrowing and spectral narrowing results in a trade-off between conversion efficiency and bandwidth. Additionally, the amplifier seed energy is often low while total gain is high, resulting in high levels of parametric superfluorescence and poor signal to noise ratio [1, 2]. While the effect of temporal gain narrowing on ultrabroadband OPCPA has been investigated [3], a study of simultaneous optimization of conversion efficiency, signal bandwidth and signal-to-superfluorescence ratio has not yet been presented.

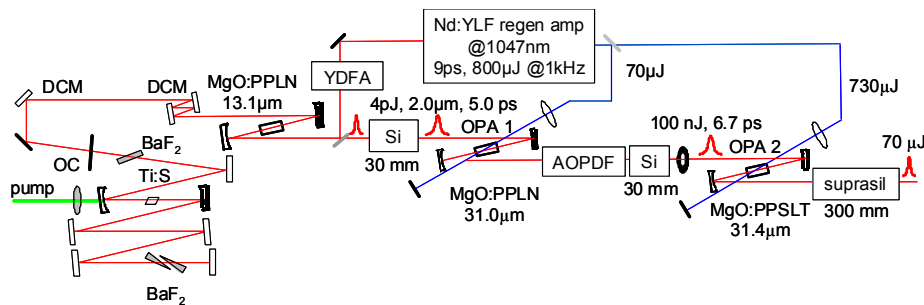
The basic compromise between conversion efficiency and amplified signal bandwidth in OPCPA is conceptually well understood: for a chirped seed pulse, frequency is mapped to time, and thus the spectral and temporal gain profiles simultaneously affect the width of the significant gain region. The optimization problem becomes more complex when suppression of superfluorescence is necessary: the seed is temporally chirped but the incoherent noise is not. Therefore the signal field has a narrower gain width than the noise field does. To suppress the superfluorescence, the signal pulse must be stretched more to cover the noise gain width so that gain quenching can take effect. However, it comes with the penalty of reduced bandwidth.



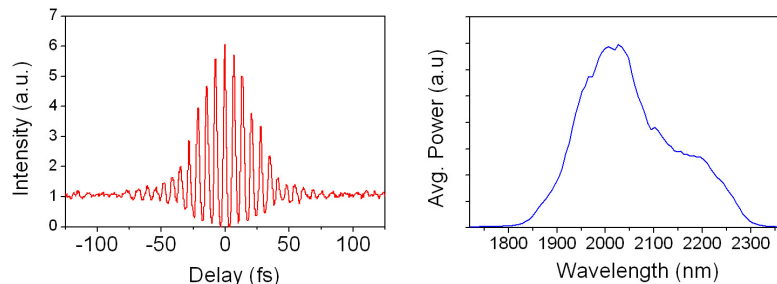
**Fig. 1.** (a) Simulation results for conversion efficiency (signal + idler) for several values of seed pulse duration and  $G = 10^4$ . The squares denote where maximum pump depletion occurs. (b) Efficiency-bandwidth product (at maximum possible conversion efficiency) versus seed pulse duration for  $G = 10^2$ ,  $10^4$ , and  $10^6$ . Triangles denote noise-to-signal ratio for  $G = 10^6$ .

Figure 1 is a set of simulation results for our 2  $\mu\text{m}$  OPCPA [4]. By varying both the pump intensity and the seed second order chirp, we explored the parameter space as shown in Fig. 1(a) for  $G = 10^4$ . Maximum conversion efficiency (squares) increases strongly with increasing seed duration until the significant gain region of the pump is filled. At this point the growth in conversion efficiency relaxes, while at the same time bandwidth begins to strongly decrease. Using these datapoints from Fig. 1(a), the efficiency-bandwidth product [panel (b), filled squares] is maximized when the seed duration is  $\sim 90\%$  of the pump duration. The same numerical analysis was conducted for the cases of a pump to signal energy ratio of  $10^2$  (circles) and  $10^6$  (open squares): a comparison between the three amplification regimes shows that the optimal seed to pump duration ratio decreases with increasing pump-to-signal energy ratio. In other words, the optimal seed duration decreases for increasing gains. Finally, a minimum in noise to signal ratio is found close to the maximum gain-bandwidth product (Fig. 1(b), triangles [ $G = 10^6$ ]).

Applying the optimization principles, our lab has been developing OPCPAs at 800 nm and 2  $\mu\text{m}$ . A schematic of our 2- $\mu\text{m}$  OPCPA system [5, 6] is shown in Fig. 2. An octave-spanning Ti:S oscillator generates passively CEP-stabilized broadband 2  $\mu\text{m}$  seed pulses by DFG in a MgO-doped periodically-poled lithium niobate (MgO:PPLN) crystal. A Nd:YLF regenerative amplifier is injection-seeded by the 1047 nm spectral component of the oscillator after pre-amplification in a fiber amplifier, and provides 9-ps, 800- $\mu\text{J}$  pump pulses for the OPCPA stages. The seed pulses are stretched in 30 mm of bulk silicon to 5-ps length and preamplified in OPA1. The pulses are then amplified to 70  $\mu\text{J}$  in OPA2 and compressed in 30 cm of near-lossless Suprasil300 glass. The infrared acousto-optic programmable dispersive filter (AOPDF), placed between amplification stages, adds programmable dispersion to allow the pulse duration to reach near transform limit after the compressor. An additional 30 mm block of silicon is placed between OPA1 and OPA2 in order to set the AOPDF chirp such that its diffraction efficiency is maximized at the same time that the chirp of the seed pulse in OPA2 (6.7 ps) is optimized for amplification. An aperture is used prior to OPA2 in order to eliminate spatial chirp caused by the AOPDF and to eliminate superfluorescence in high order spatial modes.



**Fig. 2.** Schematic of the 2  $\mu\text{m}$  OPCPA system



**Fig. 3.** (a) IAC of amplified signal pulse after compression, measuring 5 cycles (35 fs). (b) Corresponding spectrum with calculated transform limit of 27 fs.

Fig. 3(a) shows a 2nd-order interferometric autocorrelation (IAC) of the compressed pulse using two-photon absorption in InGaAs. The linear absorptive response of the detector is still significant at  $>1800$  nm, and there is some linear response distorting the 1:8 ratio of the IAC. The trace denotes a  $\sim 5$ -cycle (35-fs) compressed pulse, nearly compressed to its transform limit (27 fs). We are currently pursuing alternative diagnostics capable of measuring a 2-cycle pulse [7] and optimizing the OPCPA for a larger signal bandwidth. Previous results have already verified the CEP stability of the OPCPA process with self-CEP-stabilized seed pulses generated by DFG [2]. CEP measurements on the presented OPCPA system are also in progress.

A schematic of our 800 nm OPCPA system is shown in Fig. 4. The seed of the OPCPA is directly from the Ti:S oscillator. The oscillator produces 5-fs pulses around 800 nm with 100-pJ energy. The oscillator will be CEP stabilized actively by modulating the pump power. A narrow band fraction of the oscillator at 1047 nm is amplified with a Nd:YLF regenerative amplifier followed by a Nd:YLF multipass amplifier. The produced pulses have a 5-ps duration, an energy of 1 mJ and a repetition rate of 1 kHz. Such pulses are frequency doubled, their energy is split in two and they are used as pumps for the two stages of the OPCPA. The seed is stretched by using chirped mirrors for 800 nm produced at MIT, and then amplified by the first pump in a type-I, 5-mm long BBO crystal. The amplified pulses have an energy of 1  $\mu$ J, an extremely broad spectrum with a 4.4-fs transform-limited duration, and a 1-kHz repetition rate. The gain, considering various energy drops of the seed before amplification, is around  $10^5$ . Fig. 5 shows the comparison between the spectrum of the seed compared to the spectrum of the first stage output. After a second amplification stage, whose optimization is still in progress, we plan to compress the pulses with bulk BaF<sub>2</sub> and fused silica, measure the pulse duration with Spectral Phase Interferometry for Direct Electric-field Reconstruction [7], and verify the CEP stability with f-2f measurements.

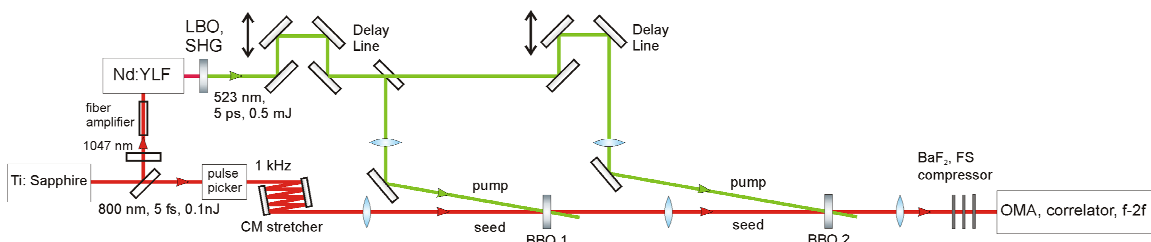


Fig. 4: Setup of the 800 nm OPCPA

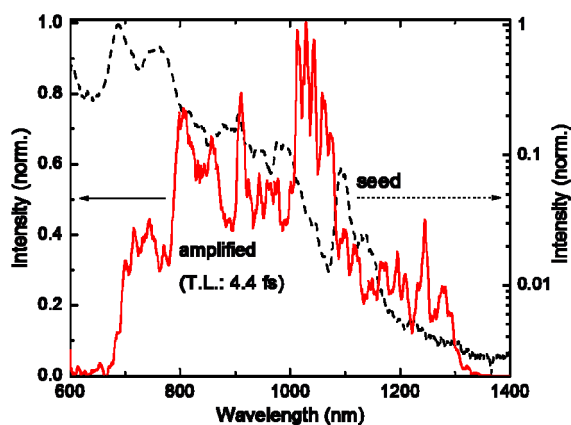


Fig. 5: First stage seed and amplified spectra.

**References**

- [1] F. Tavella, A. Marcinkevicius, and F. Krausz, *New J. of Phys.* 8, 219, 2006.
- [2] T. Fuji, N. Ishii, C. Y. Teisset, X. Gu, T. Metzger, A. Baltuška, N. Forget, D. Kaplan, A. Galvanauskas, and F. Krausz, *Opt. Lett.* 31, 1103, 2006.
- [3] S. Witte, R. T. Zinkstok, W. Hogervorst, K. S. E. Eikema, *Appl. Phys. B* 87, 677, 2007.
- [4] J. Moses, C. Manzoni, S.-W. Huang, G. Cerullo, and F. X. Kärtner, Paper TUE5I.8, *Ultrafast Phenomena*, Stresa, Italy, June 2008.
- [5] J. Moses, O. D. Mücke, A. Benedick, E. L. Falcão-Filho, S.-W. Huang, K.-H. Hong, A. M. Siddiqui, J. R. Birge, F. Ö. Ilday and F. X. Kärtner, Paper CTuEE2, *Conference on Lasers and Electro Optics (CLEO) 2008*, San Jose, CA, May 2008.
- [6] J. Moses, O. D. Mücke, S.-W. Huang, A. Benedick, E. L. Falcão-Filho, K.-H. Hong, A. M. Siddiqui, J. R. Birge, F. Ö. Ilday and F. X. Kärtner, Paper FR11p.2, *Ultrafast Phenomena*, Stresa, Italy, June 2008.
- [7] J. R. Birge, R. Eil, F. X. Kärtner, *Opt. Lett.* 31, 2063, 2006.

## Generation of high-average-power picoseconds pulse trains from cryogenically-cooled Yb:YAG amplifiers

### Sponsors

Air Force Office of Scientific Research (“DARPA HRS”) FA9550-06-1-0468  
and FA9550-07-1-0014  
MIT Lincoln Laboratory 7000013535

### Project Staff

Dr. Kyung-Han Hong, Aleem Siddiqui, Dr. Jeffrey Moses, Dr. Juliet Gopinath, Dr. John Hybl,  
Prof. F. Omer Ilday, Dr. Tso Yee Fan, and Prof. Franz X. Kärtner

### 1. Introduction

The requirements on pump sources for optical parametric chirped-pulse amplification (OPCPA) [1] are critical because parametric amplification with high efficiency while maintaining good beam quality is only possible with good spatio-temporal characteristics of the pump beam. The development of a large-average-power picosecond pump source that can be synchronized with seed beams with either high or low repetition rate is one of the most important challenges for future OPCPA technologies and their applications.

Over the last years, high-power high-repetition-rate picosecond laser technologies have been developed both on the basis of fiber and bulk amplifiers. On the side of fiber amplifier technologies, amplification of 10-ps pulses at 80 MHz to 51 W and at 47 MHz to 97 W has been demonstrated [2]. More recently, amplification of 20-ps pulses to 321 W at 1 GHz was reported [3], but for >100 W average power the pulses showed spectral broadening due to self-phase modulation (SPM). Besides limitations due to SPM, polarization maintenance is not easy to achieve in high-power fiber amplifiers. In contrast, bulk amplifiers allow much better power scalability due to the much lower constraints in peak power. Several solid-state laser systems based on Nd:YAG, thin-disk Yb:YAG, and Nd:YVO<sub>4</sub>, with average power levels ranging from 27 W to 111 W, have been demonstrated with ps or even sub-ps pulse duration [4]. Recently, a cryogenically-cooled Yb:YAG laser has proven to be a good candidate for average power scaling because of its good thermo-optic properties, small quantum defect, and low saturation fluence. At cryogenic temperatures, Yb:YAG has an emission bandwidth of 1.5 nm, suitable for picosecond pulse amplification. A high-power CW Yb:YAG laser with output power up to 450 W [5] and a picosecond amplifier at tens of kHz with 24 W [6] have been demonstrated.

In this report, we present the amplification of 5.5-ps pulses with a cryogenically-cooled Yb:YAG amplifier at a repetition rate of 78 MHz to 287 W of average output power, suitable for pumping high-repetition-rate OPCPA systems. To our knowledge, this is the highest-average-power picosecond pulse train at MHz repetition rates. The amplified pulses have a spectral bandwidth of 0.3 nm, centered at 1029 nm with good beam quality. The cryogenically-cooled Yb:YAG amplifier was developed by MIT Lincoln Laboratory, while a 6 W picosecond fiber CPA system based on chirped volume Bragg gratings (CVBGs) [7] was developed as a seed source at MIT campus. The seed source and amplifier were integrated at MIT campus and are ready for OPCPA applications.

### 2. Experimental setup and result

Figure 1 illustrates the optical layout of the fiber CPA chain and the 287-W cryogenically-cooled Yb:YAG amplifier. As a master oscillator at 78 MHz, we used a femtosecond Yb-doped fiber laser. The use of a femtosecond laser as a seed source for a picosecond amplifier allows wavelength matching to various 1- $\mu$ m amplifier media. The narrow 1029-nm portion was selectively amplified in the fiber CPA chain because several watts of seed power within 1.5-nm spectral bandwidth are necessary for efficient amplification in the Yb:YAG amplifier. The two-stage Yb-doped fiber amplifier shown in Fig. 1(a) is comprised of a single-mode preamplifier and

a 10-W commercial polarization-maintaining amplifier. Direct amplification of the seed pulses after simple spectral filtering leads to strong SPM and limits the amplification to  $\sim 0.3$  W. To boost the average power without SPM, we employed a CPA technique based on CVBGs that enable the stretching of a narrowband ps pulse to  $>100$  ps and re-compression to the original pulse duration at high efficiency. The 0.8-mW 370-ps pulse, stretched from a CVBG (OptiGrate, Inc.) in Fig. 1(a), was amplified to 30 mW by the preamplifier and then launched into the 10-W amplifier with a power of 8 mW after polarization control. We obtained a maximum average power of 10.8 W from the two-stage fiber amplifier chain. The output pulses were compressed to 4.5 ps with a bandwidth of 0.4 nm. The amplified spectrum is free of SPM-induced spectral broadening down to -50 dB, only limited by the measurement. It should be noted that the current CVBGs incur non-negligible spatial chirp due to tilt of the chirped index distribution in the CVBGs. The compressed power was 6.0 W at maximum output power from the amplifier with a compression efficiency of 56%. This fiber CPA system generated narrow-bandwidth ps pulses with enough average power and good beam quality to seed the cryogenic Yb:YAG amplifier.

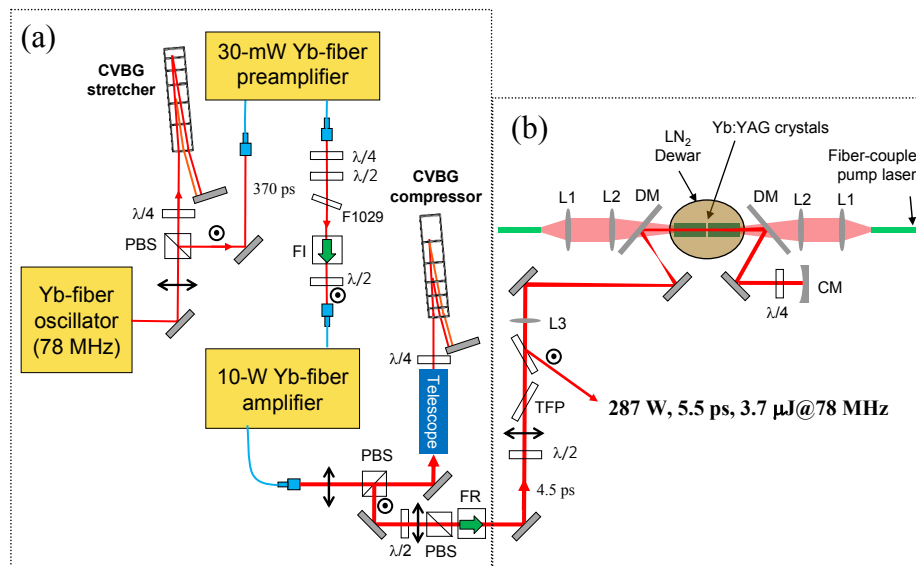


**Fig. 1.** Optical layout of a high-average-power picosecond laser system: (a) 6-W fiber CPA chain based on CVBGs, (b) 287-W cryogenically-cooled double-pass Yb:YAG amplifier. PBS, polarization beamsplitter;  $\lambda/4$ , quarter waveplate;  $\lambda/2$ , half waveplate; F1029, band-pass filter at 1029 nm; FI, Faraday isolator; FR, Faraday rotator; CVBG, chirped volume Bragg grating; TFP, thin-film polarizer; L1-L3, lens; CM, concave mirror; DM, dichroic mirror.

The amplified 4.5-ps pulse train was delivered to the cryogenically-cooled two-pass Yb:YAG amplifier pumped by 700 W of power from two fiber-coupled laser diodes, as illustrated in Fig. 1(b). The actual seed power arriving at the Yb:YAG crystal was 4 W due to power degradation in the 10 W amplifier and loss in the polarization optics. The 940 nm pump beams, delivered by two 0.4 mm diameter multimode fibers, are focused at each crystal to a diameter of  $\sim 1.6$  mm. Two 23 mm long Yb:YAG crystals have a doping concentration of 2%, and their surfaces are anti-reflection coated and have a normal-incidence cut with a 1-mm undoped YAG endcap on each side of the pump beam entrance. The pump beams are focused to the crystals through the dichroic mirrors while the crystals are cooled to 77 K by liquid nitrogen in vacuum. The double-pass geometry was implemented using two thin-film polarizers and a quarter waveplate. The seed beam diameter was adjusted to  $<1.5$  mm at the crystal for both passes using a lens (L3) and a concave mirror (CM) located at a confocal position to L3 in Fig. 1(b).

Figure 2(a) shows the measured and calculated output power versus pump power. We obtained an average output power as high as 287 W with 700 W of pump power, corresponding to an

optical-to-optical efficiency of 41%. The calculated output power assuming a Gaussian beam profile and taking into account temperature effects and loss due to amplified spontaneous emission, shows good agreement to the measured output power characteristic. The measured spectra before and after the amplification with the Yb:YAG amplifier are shown in Fig. 2(b). The amplified spectrum with a bandwidth of 0.3 nm did not show any indication of SPM. The amplified pulse duration was 5.5 ps (FWHM) from the autocorrelation trace shown in Fig. 2(c), which is 1.4 times the transform-limited pulse duration of 4.0 ps. Considering the estimated B-integral value of only  $5.1 \times 10^{-3}$  rad at the Yb:YAG crystals, the average power can be scaled to >10 kW without encountering limitations due to SPM. Spatial measurements showed a good near-field profile in the horizontal and vertical directions. The far-field image reveals an elliptical focused spot due to the spatial chirp induced by the CVBG, resulting in an  $M^2$  value in the horizontal direction as high as 2.75. The  $M^2$  value in the vertical direction was only 1.15, which is almost diffraction limited. Further spatial optimization will enhance the optical-to-optical conversion efficiency to >50%.

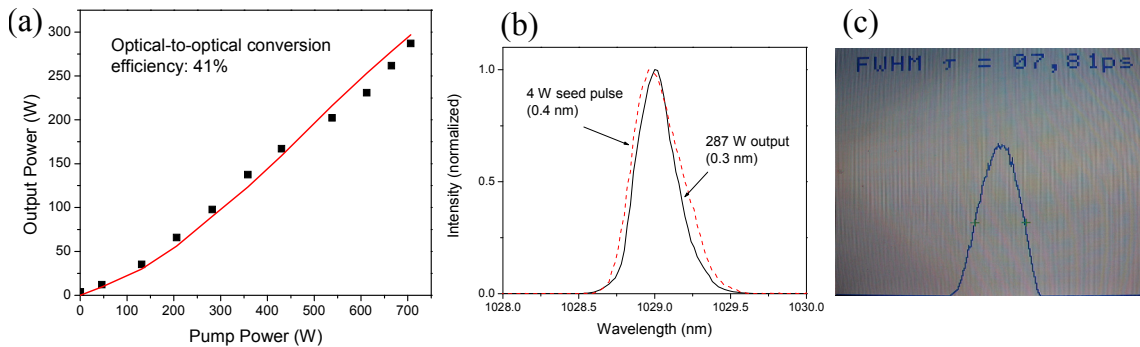


**Fig. 2.** Output power versus pump power (a), optical spectra (b), and autocorrelation measurement (c)

## References

- [1] A. Dubietis *et al.*, "Powerful femtosecond pulse generation by chirped and stretched pulse parametric amplification in BBO crystal," *Opt. Commun.* 88, 437 (1992).
- [2] J. Limpert *et al.*, "High-average-power picoseconds Yb-doped fiber amplifier," *Opt. Lett.* 26(23), 1849 (2001); J. Limpert *et al.*, "High-power picoseconds fiber amplifier based on nonlinear spectral compression," *Opt. Lett.* 30(7), 714 (2005).
- [3] P. Dupriez *et al.*, "High average power, high repetition rate, picoseconds pulsed fiber master oscillator power amplifier source seeded by a gain-switched laser diode at 1060 nm," *IEEE Photon. Tech. Lett.* 18(9), 1013 (2006).
- [4] G. J. Spühler *et al.*, "Appl. Phys. B 71, 19 (2000); F. Brunner *et al.*, "Powerful red-green-blue laser source pumped with a mode-locked thin disk laser," *Opt. Lett.* 29(16), 1921 (2004); L. McDonagh *et al.*, "111 W, 110 MHz repetition-rate, passively mode-locked TEM<sub>00</sub> Nd:YVO<sub>4</sub> master oscillator power amplifier pumped at 888 nm," *Opt. Lett.* 32(10), 1259 (2007).
- [5] T. Y. Fan *et al.*, "Cryogenic Yb<sup>3+</sup>-Doped Solid-State Lasers," *IEEE JST-QE* 13(3), 448 (2007).
- [6] S. Tokita *et al.*, "23.7-W picoseconds cryogenic-Yb:YAG multipass amplifier," *Opt. Express* 15(7), 3955 (2007).
- [7] K.-H. Liao *et al.*, "Large-aperture chirped volume Bragg grating based fiber CPA system," *Opt. Express* 15(8), 4876 (2007).

## High-Harmonic Generation with Long Wavelength Driver Pulses

### Sponsors

Air Force Office of Scientific Research (“DARPA HRS”) FA9550-06-1-0468

### Project Staff

Dr. Edilson Falcao, Vasileios Gkortsas, Dr. Ariel Gordon and Prof. Franz X. Kärtner

Optical harmonic generation is a nonlinear process where an optically driven medium emits coherent radiation at frequencies that are harmonics of the driving field. High harmonic generation (HHG) is an extreme case where high harmonic orders ( $10^2$ - $10^3$ ) of the driving frequency are emitted [1]. The driving frequency is typically in the near infrared; thus HHG can provide a source of coherent extreme ultraviolet (EUV), and possibly soft X-ray radiation, which leads to a wide range of applications, such as imaging with high spatial resolution or the generation of attosecond pulses [2]. The desire for using longer wavelength driver pulses is motivated by the scaling of the HHG single-atom response. The HHG photon energy increases quadratically with the driver pulse wavelength and linearly with its intensity, according to the cut-off law [3]:

$$\hbar\omega_{\max} = I_p + 3.17 \frac{E_0^2 e^2}{4m\omega_D^2},$$

where  $\hbar\omega_{\max}$  is the highest achievable harmonic energy,  $e$  and  $m$  are the electron charge and mass, and  $E_0$  and  $\omega_D$  are the driver field amplitude and frequency.

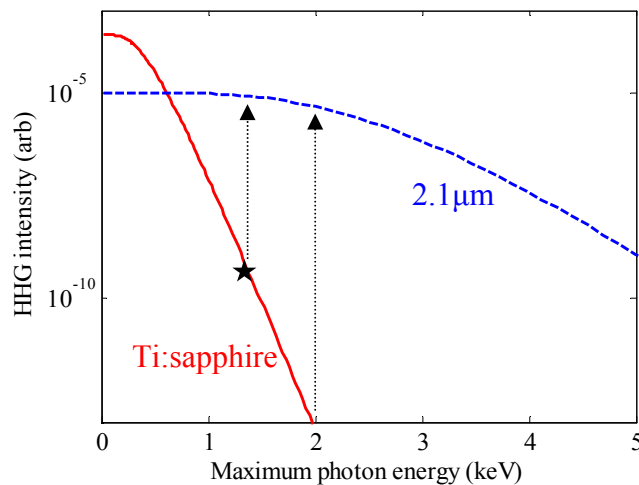


**Fig. 1:** Scaling of the single atom HHG photon yield with the maximum achievable photon energy due to quantum diffusion and ionization of the gas. Ti:sapphire driver pulses (red solid line) can hardly reach 1 keV. In the keV region, 2.1 $\mu$ m driver pulses (blue dashed) outperform them by many orders of magnitude. The star shows the location of experimental results that reached record photon energy [5] using Ti:sapphire lasers.

The conversion efficiency, in a fixed bandwidth and at the cut-off region, decreases with the fourth power of the drive wavelength and exponentially with the intensity [4]. The state-of-the-art experimental systems [5], where high photon energies are obtained by simply increasing the intensity of the driver pulses (at 720nm), already lie in the exponential tail of the efficiency curve (see Fig. E.1.) due ground state depletion (excessive ionization). This has been shown in a recent study by our group [4]. By using longer wavelength driver pulses the exponential falloff of the efficiency is pushed to much higher photon energies, as Fig. 1 demonstrates. Experimental studies of HHG with longer wavelength driver pulses are very few [6,7], and the experimental performance was limited by the pulse energy available rather than by the HHG process itself.

Our work is directed towards a compact soft-X-ray source emitting few keV photons. The driver sources are based on the Optical Parametric Chirped Pulse Amplification (OPCPA) technique and will cover the range from 800 nm to 2000 nm.

The setup for generating soft-X-ray pulses by high-harmonic generation is shown in Fig. 2. The intense driver pulses enter the HHG chamber through a window and are focused using a curved mirror. The entire system should be evacuated, at least to  $\sim 1 \times 10^{-3}$  torr. The focused pulses drill a tiny hole through the thin walls of a metallic tube (few mm diameter) by ablation and interact with the gas atoms inside the tube to generate high-harmonic radiation. The fundamental radiation and low-order harmonics ( $< 200$  eV) are suppressed by a diaphragm and thin metal filters for preventing them to reach the spectrometer. Then the soft-X-ray radiation is spectrally analyzed with a grazing incidence X-ray monochromator evacuated to  $\sim 1 \times 10^{-6}$  torr.

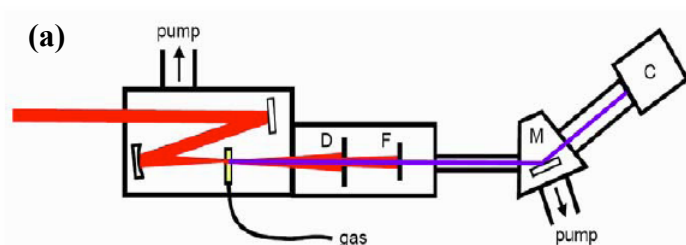
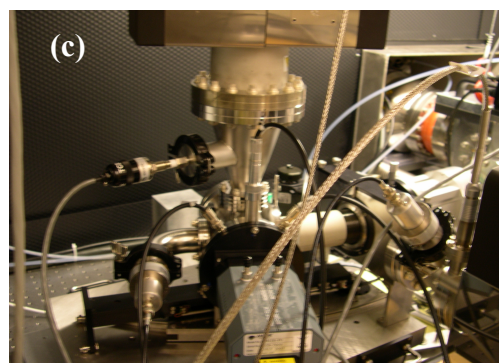
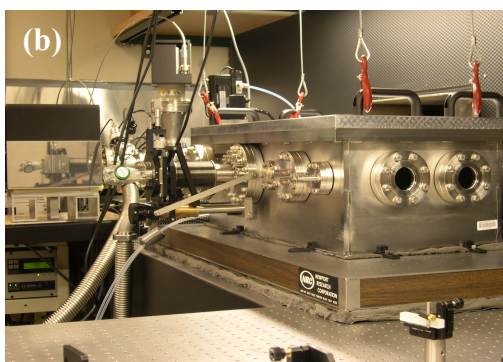


**Fig. 2:** (a) Schematic of HHG setup; (b) photo of the HHG chamber; (c) X-ray spectrometer photo.



In order to enable the measurement of the absolute number of photons per wavelength generated in the HHG, a calibration of our spectrometer was made at the Synchrotron Research Center (SRC) of the University of Wisconsin. The synchrotron radiation is an ultra-broadband radiation source with energy ranges at different beamlines determined mainly by the curvature of the electron beam at the position of the output coupler. For convenience, a monochromator, working as a spectrograph is positioned directly after the output coupler. This configuration makes the entire system behave like a tunable broadband radiation source. Using two different beam lines [the port 062 (6 meter Toroidal Grating Monochromator) and the port 041 (Varied-Line-Spacing Plane Grating Monochromator)], and in addition an absolute photodetector to characterize those lines, we calibrated our spectrometer in the range from 30 eV to 285 eV. This calibration will permit us to obtain secure numbers for the absolute efficiency of the HHG process, which is also important for comparison with theoretical results and future experiments.

Figure 3 shows a set of results with different spectral lines in the range from 150 eV to 285 eV. The modulation presented in the spectrum is mainly due to a combination of the efficiency of the spectrograph grating and of the transmission of a carbon filter used for this range of energies. The total number of photons incident on the spectrometer slit, during these measurements, varied from  $8.5 \times 10^8$  at the 150 eV line to  $5.7 \times 10^5$  at the 285 eV line.

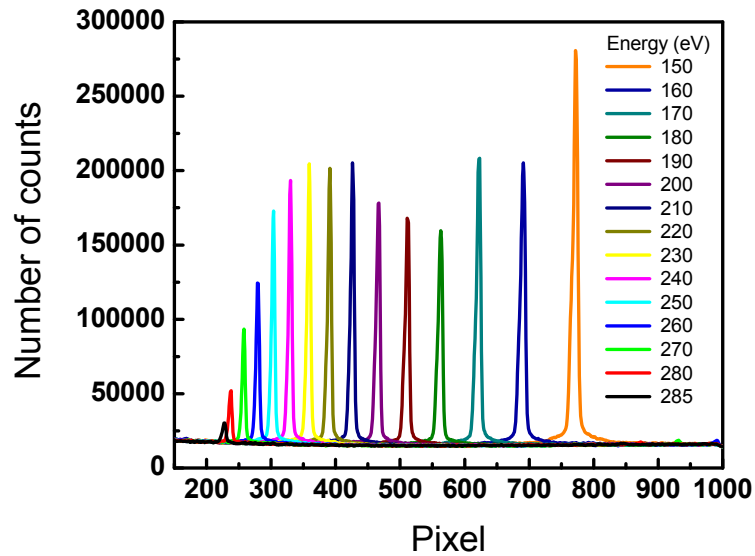


**Fig. 3:** Results obtained at the SRC. The horizontal scale corresponds to the pixel position of the CCD and the vertical scale corresponds to the number of counts detected.

## References

- [1] T. Brabec and F. Krausz, "Intense few-cycle laser fields: Frontiers of nonlinear optics", *Reviews of Modern Physics*, vol. 72, pp. 545-91, 2000.
- [2] R. Kienberger and F. Krausz, "Subfemtosecond XUV Pulses: Attosecond Metrology and Spectroscopy," in *Few-Cycle Laser Pulse Generation and Its Applications*, vol. 95, *Top. Appl. Phys.*, F. X. Kärtner, Ed. New York, Berlin: Springer-Verlag, 2004, pp. 343–379.
- [3] M. Lewenstein, P. Balcou, M. Y. Ivanov, A. L'Huillier, and P. B. Corkum, "Theory of High Harmonic Generation by low-frequency laser fields", *Phys. Rev. A*, vol. 49, pp. 2117-2132, 1994.
- [4] A. Gordon and F. X. Kärtner, "Scaling of keV HHG photon yield with drive wavelength", *Opt. Expr.*, vol. 13, pp. 2941-2947, 2005.
- [5] J. Seres, E. Seres, A. J. Verhoef, G. Tempea, C. Strelci, P. Wobrauschek, V. Yakovlev, A. Scrinzi, C. Spielmann, and F. Krausz, "Source of coherent kiloelectronvolt X-rays", *Nature*, vol. 433, pp. 596, 2005.
- [6] B. Sheehy, J. D. D. Martin, L. F. DiMauro, P. Agostini, K. J. Schafer, M. B. Gaarde, and K. C. Kulander, "High Harmonic Generation at Long Wavelengths", *Phys. Rev. Lett.*, vol. 83, pp. 5170-5273, 1999.
- [7] B. Shan and Z. Chang, "Dramatic extension of the high-order harmonic cutoff by using a long-wavelength driving field", *Phys. Rev. A*, vol. 65, pp. 011804(R)-1-4, 2002.
- [8] N. Ishii et al., "Development of a Few-Cycle Infrared OPCPA System and Its Use in High-Harmonic Generation", *Proceedings of CLEO/QELS Conference, CMK2*, 2007.
- [9] C. Vozzi et al., "Generation of High-order Harmonics with a Near-IR Self-phase-stabilized Parametric Source", *Proceedings of Conference on Ultrafast Phenomena, FRI2.2*, 2008.
- [10] P. Colosimo et al., "Scaling strong-field interactions towards the classical limit", *Nature Physics*, vol. 4, pp. 386-389, 2008.

## Photonic Analog to Digital Conversion

### Sponsors

Defense Advanced Research Projects Agency (DARPA) under Grant W911NF-04-1-0431

### Project Staff

R. Amataya, T. Barwicz, H. Byun, F. Gan, C. W. Holzwarth, O. O. Olubuyide, J. S. Orcutt, M. Park, M. A. Popović, P. T. Rackich, Professors G. Barbastathis, E. P. Ippen, J. L. Hoyt, F. X. Kaertner, M. Perrott, R. J. Ram, and H. I. Smith and Doctors M. Geis, M. Grein, T. Lyszczarz, S. Spector, and J. U. Yoon from MITLincoln Laboratory

The goal of this program is to leverage the low jitter properties of mode-locked lasers to achieve photonic analog to digital converters that overcome the bottleneck in speed and jitter of current purely electronic technology. Several photonic ADC techniques have been investigated in recent years [1,2]. The photonic ADC architecture pursued here in the form of an electronic photonic integrated circuit is known as time-interleaved optical sampling using wavelength-division multiplexing (WDM) [2] techniques. The envisioned sampling system is shown in Figure 1. A chirped optical clock signal from a mode-locked laser is channelized in time using precisely-tuned WDM filters to create time-interleaved optical sampling signals, each

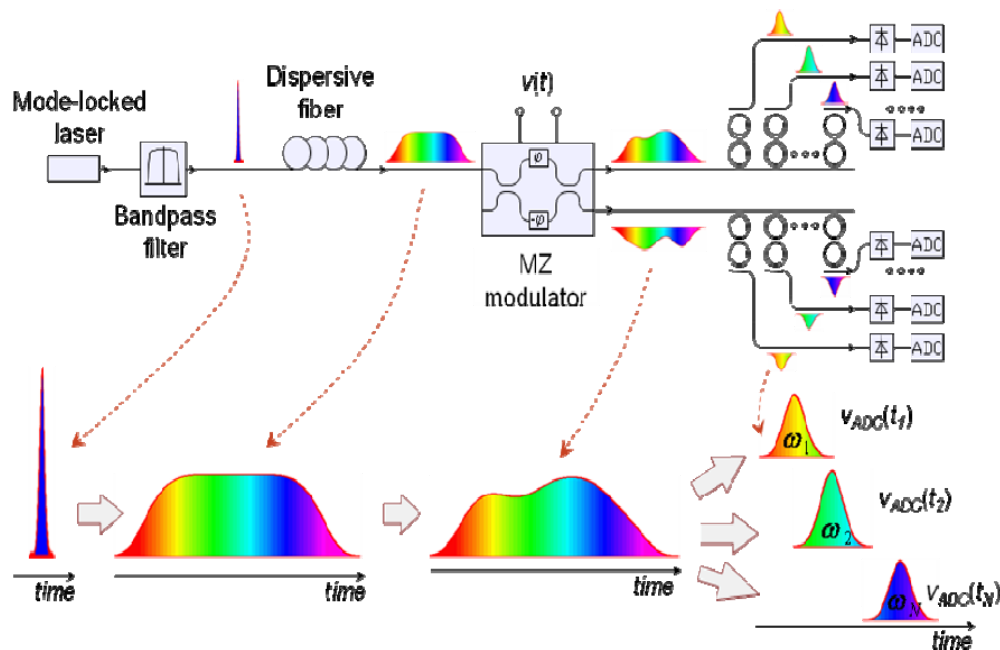


**Figure 1:** Schematic layout of the photonic ADC.

operating at the rate of the mode-locked laser, here 2 GHz). The total sampling rate is then the optical clock rate times the number  $N$  of WDM channels (here,  $N=20$ ). However, in order to realize the high resolution, the sampling times of the interleaved channels must be uniform, the converter gains from each channel must be closely matched, and the sample memory effects must be minimal. These characteristics require monitoring and tight feedback control of the WDM filters. A signal recovery algorithm has been developed that enables reconstruction of the actual RF-signal in the presence of small but deterministic errors in filter spacing and unequal converter gain. The ADC chip requires the development of a number of devices: Thermally tunable WDM filter banks with large FSR, wideband optical modulators, Ge- photodetectors, and low jitter femtosecond lasers, potentially also integrated. These devices are pursued in a close

collaboration between research groups at MIT Campus and MIT Lincoln Laboratory in various technologies. All these devices and techniques must be integrated on a CMOS compatible technology platform. As an example the proposed ADC chip requires filters with large free spectral range (FSR) and low loss. These two key requirements call for microring filters fabricated in a high-index contrast (HIC) material system.

The microring resonator filter designs used for fabrication of the filter banks presented here are based on to the design described in [3]. By utilizing this design with the HIC materials of silicon-rich silicon nitride ( $n = 2.2 @ 1550 \text{ nm}$ ) forming the core, and silicon dioxide ( $n = 1.455 @ 1550 \text{ nm}$ ) or air cladding a very wide FSR of 20 nm is realized. The filter design was fine tuned to achieve the objective of a 3 dB bandwidth of 25 GHz and less than 30 dB adjacent channel crosstalk for 80 GHz spaced channels. A 20 channel dual filter bank was fabricated (Figure 2).

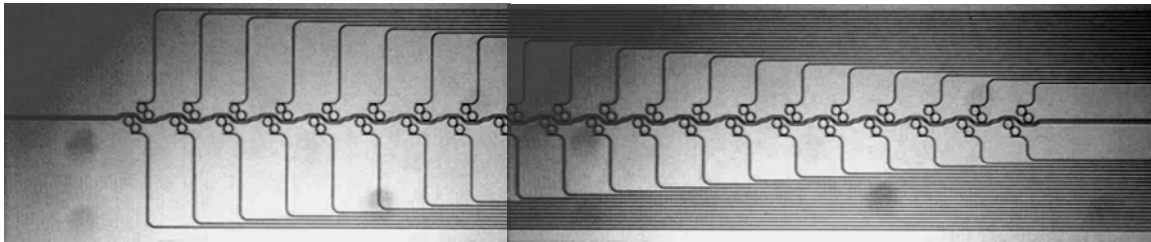


**Figure 2:** Twenty channel dual filter bank fabricated in SiN.

Direct-write scanning electron beam lithography (SEBL) was used due to its combination of high resolution and high level of dimensional control. The basic fabrication process used is similar to that described in [4]. Controlling the resonant frequency of HIC microring resonator filters requires an extremely high level of dimensional control. Fine tuning of filters to an exact frequency grid with heaters is in progress.

Description of the other devices necessary for the EPIC ADC-chip, such as low jitter femtosecond lasers, high-speed silicon modulators and Ge-photodetectors as well as the signal recovery algorithm can be found in various summaries of the participating groups throughout this progress report.

## References

1. P. W. Juodawlkis, J. C. Twichell, G. E. Betts, J. J. Hargreaves, R. D. Younger, J.L. Wasserman, F. J. O'Donnell, K. G. Ray, and R. C. Williamson, "Optically sampled analog-to-digital converters," *IEEE Trans. Microwave Theory Tech.* 49(10), 1840 (2001).
2. M. Y. Frankel, J. U. Kang, and R. D. Esman, "High-performance photonic analogue-to-digital converter," *Electron. Lett.* 33(25), 2096 (1997).
3. M.A. Popović, T. Barwicz, M.R. Watts, P.T. Rakich, L. Socci, E.P. Ippen, F.X. Kärtner and H.I. Smith, "Multistage high-order microring-resonator add-drop filters," *Opt. Lett.*, vol. 31, no. 17, September 1, 2006 (to appear).
4. T. Barwicz, M.A. Popović, M.R. Watts, P.T. Rakich, E.P. Ippen and H.I. Smith, "Fabrication of Add-Drop Filters Based on Frequency-Matched Microring Resonators," *J. Lightwave Technol.*, vol. 24, no. 5, May 2006, pp. 2207-2218.

## High-Resolution Timing Jitter Characterization of Mode-Locked Lasers

### Sponsors

Defense Advanced Research Project Agency (DARPA OAWG Program) HR0011-05-C-0155  
 Defense Advanced Research Project Agency (DARPA EPIC Program) W911NF-04-1-0431  
 Office of Naval Research (ONR) N00014-02-1-0717

### Project Staff

Dr. Jungwon Kim, Jeff Chen, Jonathan A. Cox, and Professor Franz X. Kärtner

It has been known that mode-locked solid-state lasers can generate optical pulse trains with ultra-low timing jitter. However, the characterization of timing jitter of free-running mode-locked lasers with attosecond-resolution is a highly nontrivial task. The accurate measurement of the high-frequency noise of mode-locked lasers is important for high-precision applications such as analog-to-digital converters, microwave signal synthesis, and large-scale timing distribution.

The most common measurement technique using a high-speed photodetector and a microwave mixer suffers from excess phase noise in the photodetection process and the limited timing resolution of mixers. The use of optical cross-correlation is an attractive approach in measuring timing jitter with high sensitivity and sufficient detection range. It also does not involve excess noise in the photodetection. In particular, balanced optical cross-correlation [1,2] can precisely extract the timing information without conversion of intensity noise into timing jitter. Here we demonstrate the characterization of the pulse timing jitter spectral density of free-running mode-locked lasers using balanced optical cross-correlation in the two configurations.

The first method, named the timing detector method, is analogous to the phase detector method [3] for phase noise characterization of microwave oscillators. It uses a low-bandwidth lock between the two mode-locked lasers and measures the relative timing jitter outside the locking bandwidth with a balanced cross-correlator. Figure 1(a) shows the schematic of the timing detector method. The laser under test is a commercial 200-MHz Er-fiber laser (Laser 1). The laser used as a reference (Laser 2) is a 200-MHz soliton Er-fiber laser [4]. The repetition rates of the two lasers are locked by a kHz-bandwidth phase-locked loop. By adjusting the relative delay between the two lasers, the locking point is placed at the linear detection regime of the balanced cross-correlation. The balanced cross-correlator is based on a single type-II phase-matched PPKTP crystal, which was recently demonstrated in [2].

The second method, named the timing delay method, is the optical equivalent of the delay-line frequency discriminator method [3]. As shown in Fig. 1(b), we use a 325-m long timing-stabilized and dispersion-compensated fiber link as a delay line, and measure the timing jitter between the pulse reflected from the end of fiber link and the pulse from the laser. We can measure the timing jitter of Laser 1 from  $f_{delay} = 1/T_{delay} = 310$  kHz to the Nyquist frequency, where  $T_{delay}$  is the delay time between the two pulses. The link is timing stabilized with 1 kHz bandwidth to prevent timing drift of the fiber link as shown in [2].

Figure 2 summarizes the measurement results of timing jitter spectral densities. Curves (1) and (2) show the measurement results for Laser 1 and 2, respectively, when measured by microwave-based techniques using a signal source analyzer (Agilent E5052B). Because the results depend on the input optical power and instrument settings, the best measurement results are included for a fair comparison with the optical cross-correlator based results (curves (3)-(5) in Fig. 2). Curve (3) shows the result obtained with the timing detector method when Laser 1 and 2 are synchronized with 2 kHz-bandwidth lock. The measured power spectral density is dominated by the laser with the worst jitter. The lower frequency range (<5 kHz) discrepancies arise from the feedback loop overshoot at the locking loop bandwidth. Above 20 kHz, the cross-correlation and signal source analyzer results show a significant difference, and the cross-correlation measurement indicates that the actual laser noise is much lower than the measured data using

the signal source analyzer. Curve (4) shows the cross-correlation result obtained with the timing delay method using the round-trip delay from the 325-m long fiber. Curve (5) shows the calculated timing jitter density of Laser 1 from curve (4) cross-correlation result [5]. Curve (6) shows the measured shot-noise limit of the timing delay method,  $2.2 \times 10^{-8} \text{ fs}^2/\text{Hz}$ . This noise floor sets the limit of 470 attoseconds resolution in 10 MHz bandwidth.

By combining the results of curve (3) in the [10 kHz, 310 kHz] range and curve (5) in the [310 kHz, 10 MHz] range, we can extract the upper limit for the integrated timing jitter of Laser 1 as 0.72 fs, 1.02 fs and 5.19 fs in the [1 MHz, 10 MHz], [100 kHz, 10 MHz] and [10 kHz, 10 MHz] ranges, respectively.

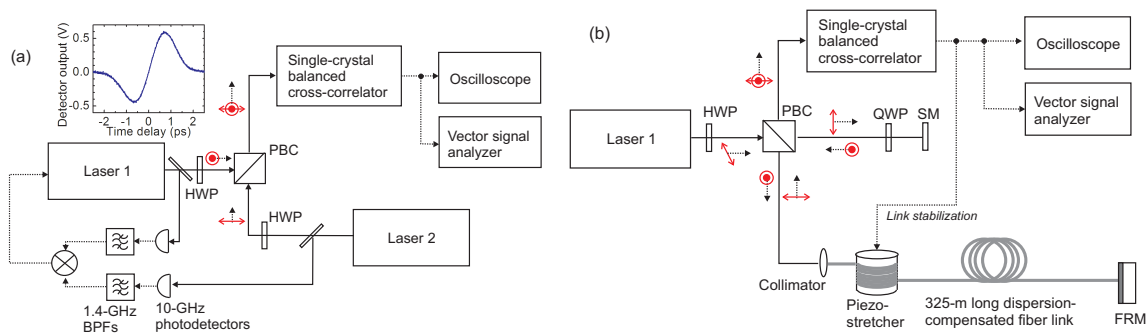


**Figure 1:** (a) The timing detector method. (b) The timing delay method. BPF, bandpass filter; FRM, Faraday-rotating mirror; HWP, half-wave plate; PBC, polarization beamsplitting cube; QWP, quarter-wave plate; SM, silver mirror.

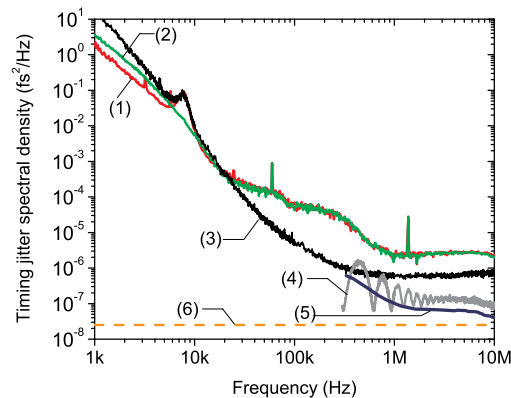


**Figure 2:** Timing jitter spectral density measurement results.

## References

- [1] T. R. Schibli et al, "Attosecond active synchronization of passively mode-locked lasers using balanced cross correlation," *Opt. Lett.* 28(11): 947-949 (2003).
- [2] J. Kim et al, "Long-term femtosecond timing link stabilization using a single-crystal balanced cross-correlator," *Opt. Lett.* 32(9): 1044-1046 (2007).
- [3] Agilent Technologies, "Phase Noise Characterization of Microwave Oscillator," Product Note 11729C-2.
- [4] J. Chen, J. W. Sickler, E. P. Ippen, and F. X. Kärtner, "High repetition rate, low jitter, low intensity noise, fundamentally mode-locked 167 fs soliton Er-fiber laser," *Opt. Lett.* 32(11): 1566-1568 (2007).
- [5] L. A. Jiang, S. T. Wong, M. E. Grein, E. P. Ippen, and H. A. Haus, "Measuring Timing Jitter with Optical Cross Correlations," *IEEE J. Quantum Electron.* 38(8): 1047-1052 (2002).

## High-Resolution Photonic Downconverting Analog-to-Digital Converter

### Sponsors

Defense Advanced Research Projects Agency (DARPA-EPIC Program) W911NF-04-1-0431  
Air Force Office of Scientific Research (AFOSR), Contract FA9550-07-1-0014

### Project Staff

Dr. Jungwon Kim, Matthew J. Park, Professor Michael H. Perrott, and Professor Franz X. Kärtner

Recently, sub-10 fs timing jitter has been measured for a free-running passively mode-locked Er-fiber laser integrated in the 10 kHz – 10 MHz range [1]. This sub-10 fs timing jitter can greatly benefit the sampling resolution of high-frequency microwave signals. For example, for 8-bit resolution sampling of a 40-GHz signal, an aperture jitter less than 10 fs is required. This level of jitter is difficult to achieve in a purely electronic implementation, and the use of low-jitter optical pulse trains open up new possibilities in analog-to-digital conversion [2].

Here, we demonstrate a novel optical sub-sampling downconversion receiver and analog-to-digital converter (ADC) for digitization of narrowband microwave signals at frequencies up to 40 GHz. This ADC may play an important role in radar and communication systems operating at high carrier frequency (e.g., >10 GHz) as well as in high-precision diagnostic of microwave signals in next generation light sources and accelerator facilities. The demonstrated signal to noise-plus-distortion ratio (SNDR) is 44 dB in 2-MHz bandwidth with a 40 GHz carrier frequency, corresponding to 7 effective-number-of-bit (ENOB). The measurement is currently limited by the timing jitter of the sampled 40 GHz signal itself, and the shot-noise-limited SNDR is 52 dB. To the best of our knowledge, this is the first demonstration of direct digitization of a microwave signal at 40 GHz with 7-bit resolution by leveraging a sub-sampling downconversion receiver. This experiment demonstrates that the low jitter properties of femtosecond lasers can be exploited to overcome electronic jitter limitations in ADCs.

The basic idea is downconversion of a narrowband high-frequency ( $\sim Nf_{rep}$ ) microwave signal to the baseband by sub-sampling with an optical pulse train having a repetition rate of  $f_{rep}$ . Figure 1 shows the schematic of the demonstrated optical sub-sampling downconverter and ADC.

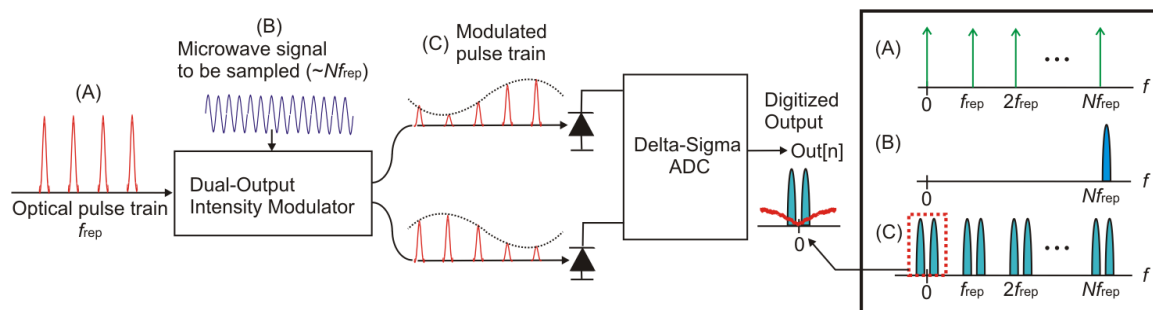


**Figure 1:** Schematic of the optical sub-sampling downconversion receiver and ADC.

The first step is frequency-mixing of the narrowband high-frequency microwave signal with the optical pulse train in the optical domain. This is done by applying the optical pulse train with a repetition rate  $f_{rep}$  to an intensity modulator driven by the microwave signal that we aim to sample with a frequency  $\sim Nf_{rep}$ . The spectrum of the microwave signal is copied at every harmonic of the repetition rate including at  $f=0$  (baseband) in the frequency domain. By low-pass filtering the baseband copy, one can downconvert the high-frequency microwave signal to baseband in the optical domain. The second step is transferring the information in the optical domain to the electronic domain. This can be done simply by applying the modulated pulse train to photodiodes. These elements also serve as the input stage to the continuous-time delta-sigma ADC. In this

ADC architecture, the baseband analog signal is filtered electronically and then quantized by a 1-bit resolution ADC operating at a high sample rate. The noise-shaping of the delta-sigma ADC enables high signal-to-noise ratio (SNR) in the narrow frequency band of interest.

For the demonstration experiment, a commercial 200-MHz repetition rate Er-fiber laser (Menlo Systems M-Comb-Custom) is used for generation of the sampling pulse train. It generates a train of  $\sim 200$  fs optical pulses with  $\sim 5$  fs timing jitter in the 10kHz–10MHz range [1]. The pulse train is applied to a dual-output 40-GHz LiNbO<sub>3</sub> Mach-Zehnder intensity modulator (EOSpace AZ-1x2-AV5-40). The two differentially modulated outputs from the modulator result in the suppression of the 2nd harmonic distortion. The used photodiodes are fiber-pigtailed, matched InGaAs pin-photodiodes (Hamamatsu G8195). The delta-sigma modulator as well as digital electronics is implemented as an integrated circuit. The custom IC is fabricated in the 0.18  $\mu\text{m}$  CMOS process of National Semiconductor. The ADC is clocked at 200 MHz, matched with the repetition rate of the mode-locked laser. This clock rate provides an over-sampling ratio (OSR) of 50 over an effective bandwidth of 2 MHz. The sampled microwave signal is generated by Agilent E8267D vector signal generator (VSG) with a 40.039 GHz carrier frequency and +1 dBm power level. It is set to the 200th harmonic of the repetition rate (200 MHz) plus 500 kHz for measuring SNDR and SNR. For digital modulation, a 1-Mbps GMSK signal with 40.04 GHz carrier is used.

Figure 2 shows the measured FFT of the digitized baseband output (curve 1) and the measured RF spectra of the balanced photodetector output. The maximum SNDR of the FFT result is 44 dB over an effective bandwidth of 2 MHz, which is equivalent to 7-ENOB resolution at 40 GHz. This number is lower than the predicted 52 dB SNDR (8.7-ENOB) assuming the ideal case when the shot-noise limited SNR and the modulator-nonlinearity-limited spurious-free dynamic range (SFDR) are balanced. In fact, it turns out that the noise floor from the VSG itself (curve 2) sets the noise floor of the FFT spectrum. The shot-noise-limited noise floor (curve 3) is 10 dB lower than the signal generator noise floor, which means that the measured SNDR and ENOB are not limited by the jitter of the optical pulse train, but rather by the jitter of the sampled microwave signal ( $\sim 16$  fs). Based on the measured shot-noise limited noise floor, the measurement capability is expected to be beyond 50 dB SNDR.

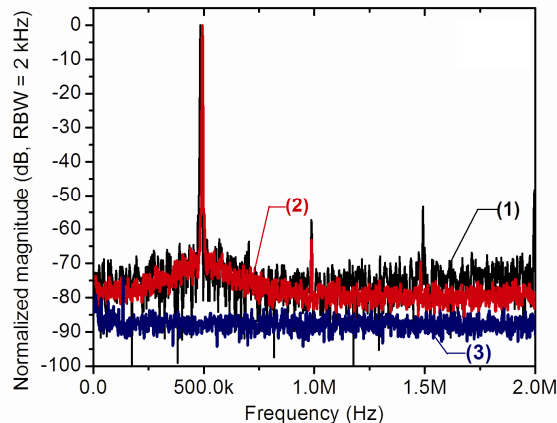


**Figure 2:** Curve 1 (black), measured FFT spectrum of the digitized baseband output; curve 2 (red), measured RF spectrum of balanced photodetector output when 40-GHz signal source is on; curve 3 (blue), measured RF spectrum of balanced photodetector output when 40-GHz signal source is off, and the signal is shot-noise limited.

## References

- [1] J. Kim, J. Chen, J. Cox and F. X. Kärtner, "Attosecond-resolution timing jitter characterization of free-running mode-locked lasers," *Opt. Lett.* 32(24): 3519-3521 (2007).
- [2] G. C. Valley, "Photonic analog-to-digital converters," *Opt. Express* 15(5): 1955-1982 (2007), and the references therein.

## High-Speed, Broadband, Silicon Electro-Optic Dual Output Modulators

### Sponsors

Defense Advanced Research Projects Agency (DARPA-EPIC) under Grant W911NF-04-1-0431 and Air Force Contract FA8721-05-C-0002.

### Project Staff

G-R. Zhou, F. Gan, Dr. S. J. Spector, Dr. M. W. Geis, Dr. M. E. Grein, Dr. M.A. Popović, Dr. J. U. Yoon, D. M. Lennon, Professor E. P. Ippen, Dr. T. M. Lyszczarz, and Professor Franz X. Kärtner

The development of silicon photonics has the potential to allow monolithically integrated, low-cost optical devices on a platform compatible with CMOS circuits. Optical modulators are an essential component in most applications and specifically for photonic analog to digital converters. There has been considerable recent effort directed at developing silicon based optical modulators [1, 2]. The most successful devices have used the free-carrier plasma dispersion effect, where a change in density of carriers causes a change in the refractive index of silicon. Carrier depletion has achieved the best high speed result to date, with a Mach Zehnder based modulator achieving 30 GHz of electrical bandwidth and a  $V_{\pi}L$  of 4 V·cm [1]. One disadvantage of the design in [1] is the use of a top contact which requires an epitaxial silicon overgrowth. The design presented here does not use a top contact, and shows performance approaching that of [1], with 26 GHz bandwidth and a  $V_{\pi}L$  of 4 V·cm [3].

The modulators are fabricated using Unibond silicon-on-insulator (SOI) wafers with a 0.22  $\mu\text{m}$  thick layer of silicon above a 3  $\mu\text{m}$  buried oxide (see Fig. 1(a)). The active areas of the device are p-n diode phase shifter sections in the arms of the modulator. An additional thermal phase shifter (not shown) is fabricated on one arm. An adiabatic 4-port 3 dB coupler is used at the output of the Mach-Zehnder interferometer leading to two complementary modulator output ports, needed for application in photonic analog-to-digital conversion [4]. An adiabatic 3 dB coupler design was chosen over a conventional one because of less stringent fabrication tolerances. The optimized coupler length is only 130  $\mu\text{m}$ .

Fig. 1(b) shows the cross-section of the waveguide in the active area of the modulator.

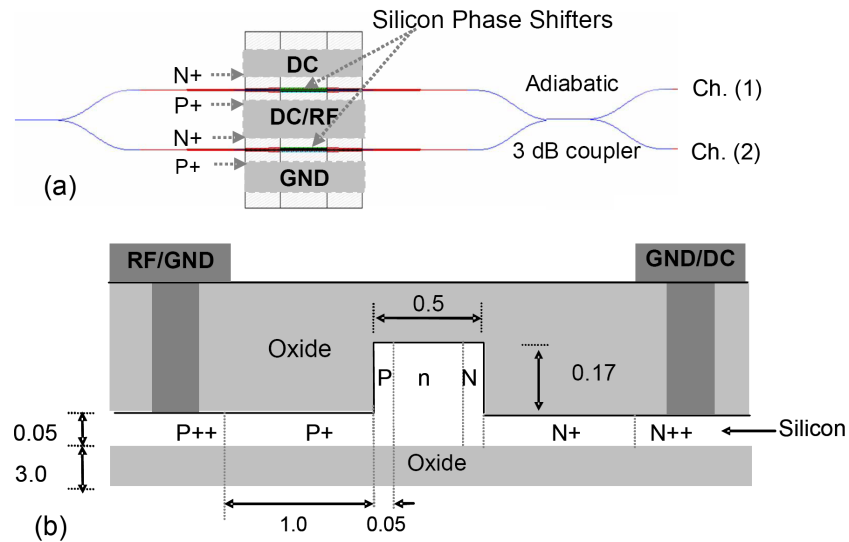


Fig. 1. (a) Top-view layout of the dual-output modulator, (b) schematic view of the cross-section of one of the phase shifters. (All dimensions are in  $\mu\text{m}$ ).

The central region (core) of the waveguide is 220 nm thick, 500 nm wide, and lightly n-type doped to a concentration of  $2 \times 10^{17} \text{ cm}^{-3}$ , resulting in a break down voltage of 16 V. The sidewalls are moderately doped, n-type on one side and p-type on the other, to a concentration of  $10^{18} \text{ cm}^{-3}$  and an approximate depth of 50 nm. When a reverse bias is applied, a depletion region forms at the p-n junction on one side of the waveguide, changing the refractive index. To make electrical contact to the core of the waveguide, heavily doped ( $10^{19} \text{ cm}^{-3}$ ), 50 nm thick slab regions connect the waveguide to metal contacts located  $1 \mu\text{m}$  away. To ensure good ohmic contact, the silicon slab under the metal contacts is degenerately doped to a concentration of  $10^{21} \text{ cm}^{-3}$ .

To model the carrier concentration in the waveguide, numerical simulations were performed by solving Poisson and carrier continuity equations. The simulations show that the application of a reverse bias of 8 V causes an increase in the modal index,  $\Delta N_{\text{eff}}$ , of  $\sim 1.67 \times 10^{-4}$  as well as in the absorption coefficient,  $\Delta \alpha$ , of  $\sim 1.61 \text{ cm}^{-1}$ . With an interaction length of 0.5 mm, this corresponds to a phase change  $\Delta \phi$  of  $0.11\pi$  and absorption loss of 0.34 dB.

Simple modeling can be used to estimate the electrical bandwidth of a 0.5 mm long device. The input capacitance of the diodes in the MZ interferometer is calculated to be  $\sim 0.1 \text{ pF}$  and the contact pad capacitance is  $< 0.05 \text{ pF}$ . This gives an estimate total capacitance from 0.1 and 0.15 pF. The  $5 \Omega$  of internal resistance in the MZ and  $50 \Omega$  output impedance of the RF power supply gives a calculated RC bandwidth of between 20 and 30 GHz.

The DC response of the modulator was tested by varying the DC bias voltage on arm #1 while the other arm remained at the same bias level. Fig. 2 shows the simulated and measured normalized light intensity as a function of the applied voltage, for the two complementary outputs. The measured and simulated results are in good agreement. The output of that modulator is also shown in Fig. 2(a), and gives a  $V\pi L$  of just over  $4 \text{ V}\cdot\text{cm}$ , which is comparable to results achieved earlier with a structure requiring more complicated fabrication [2]. Operating the modulator in a push-pull configuration has also been demonstrated, and cuts the effective  $V\pi L$  for the device in half to  $2 \text{ V}\cdot\text{cm}$ , as expected.

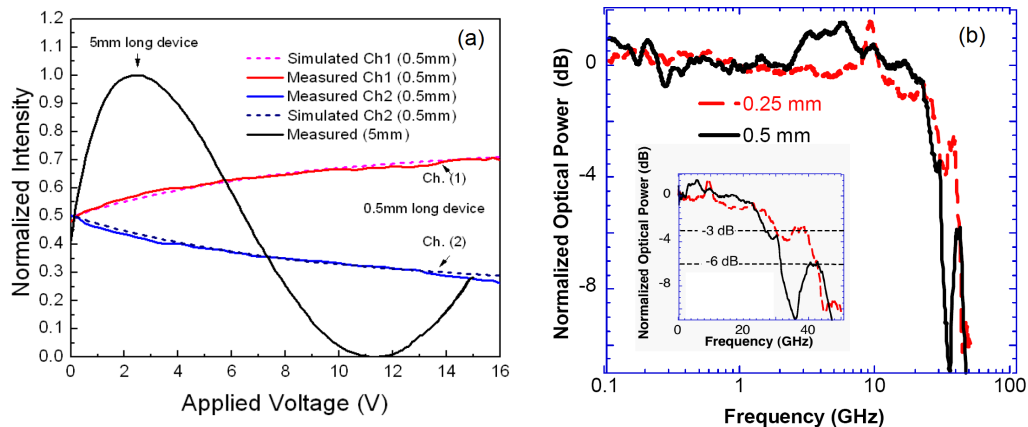


**Fig 2.** (a) Measured and simulated normalized light transmission as a function of applied voltage. (b) Measured frequency response of the modulator

Fig. 2(b) shows the small signal frequency response of the modulator after correction for frequency dependent cable losses. A 3-dB cut-off frequency of 26 GHz is reached in a 0.5 mm device, which agrees with the estimate calculated above. A shorter device with 0.25 mm long phase shifters was also measured, and exhibits 30-40 GHz of bandwidth. In order to drive the modulator with higher power, an RF amplifier and bias-T were added to the above experimental set-up. When running the 0.5 mm device in a push-pull configuration, 46 mW of RF power

achieves ~22% modulation depth for a 26 GHz sinusoid. From the  $V_{\pi}L$  of 2 V·cm, it can be found that a voltage of  $\pm 4.5$  V is necessary to achieve a 22% modulation depth in a 0.5 mm device.

In conclusion, we have demonstrated a silicon modulator with two complementary outputs, a  $V_{\pi}L$  of 4 V·cm (or 2 V·cm for the whole device operating in push-pull), and a 3-dB bandwidth of 26 GHz. A modulation depth of 22% was achieved. The insertion loss of the device is 10 dB, about half of which occurs on chip, and half of which occurs coupling in and out of the device.

## References

- [1] L. Liao, A. Liu, D. Rubin et. al., "40 Gbit/s silicon optical modulator for highspeed applications," *Electron. Lett.* 43(22): 1196-97 (2007).
- [2] L. Liao, D. Samara-Rubio, M. Morse, A. Liu, and D. Hodge, "High speed silicon Mach-Zehnder modulator," *Opt. Express* 13, 3129-3135 (2005).
- [3] S.J. Spector, M.W. Geis, G.-R. Zhou et. al., "CMOS-Compatible Dual-Output Wideband Silicon Modulator for Analog Signal Processing," *Optics Express* 16(15): 11027-31 (2008).
- [4] F.X. Kärtner, et. al., "Photonic analog-to-digital conversion with electronic-photonic integrated circuits", Proc. SPIE 6898: 689806 (2008).

## Accuracy of Photonic Analog to Digital Converters

### Sponsors

Defense Advanced Research Projects Agency (DARPA) under Grant W911NF-04-1-0431

### Project Staff

Anatol Khilo, Jonathan R. Birge and Professor Franz X. Kärtner

Photonic analog-to-digital converters (ADCs) [1] have the potential to exceed the performance of state-of-the-art electronic ADCs by orders of magnitude due to availability of very low-jitter pulse trains generated with mode-locked lasers [2], which can be used for sampling radio-frequency (RF) signals with very low aperture jitter. To increase the sampling rate of a photonic ADC, a scheme with wavelength demultiplexing of a pulse train into multiple channels and subsequent independent processing of these channels can be employed [3]. However, even if the timing jitter is very low, achieving precise analog-to-digital conversion of a wideband RF signal is a challenging task due to the high sensitivity of the ADC output to changes in ADC parameters. This report examines some factors determining the final ADC accuracy achievable and presents a universal algorithm for error correction by data post-processing.

The layout of the wavelength-demultiplexed photonic sampling ADC being considered is shown in Fig. 1 [3, 4]. A low-jitter pulse train with repetition rate  $f_R$  passes through a dispersive fiber with length  $L$  and dispersion coefficient  $\beta_2$ , which imposes chirp so that a frequency component  $\omega$  gets delayed by  $\tau(\omega) = \beta_2 \omega L$ . The chirped pulse train is modulated by a Mach-Zehnder (MZ) modulator whose RF driving voltage  $v(t)$  is the signal to be sampled. The modulator effectively imprints the time dependence of  $v(t)$  onto the optical spectrum. The optical signal is demultiplexed into  $N$  channels by a filter bank, so that every pulse is split into  $N$  sub-pulses. Each sub-pulse is detected by a photodetector and digitized by an electronic ADC taking one sample per pulse. This sample represents the RF signal at time moment  $t_n = \tau(\omega_n)$ , where  $\omega_n$  is the filter center frequency. We obtain  $N$  samples  $v_{ADC}(t_n)$  spaced uniformly across the repetition period  $T$  if we make sure that  $\beta_2 L \Delta\omega N = T$ , where  $\Delta\omega$  is the channel frequency spacing. This approach allows to improve the sampling rate over what is available in electronic ADCs by a factor of  $N$ . By using both outputs of the MZ modulator we can linearize its transfer function which is otherwise sinusoidal and factor out pulse-to-pulse energy fluctuations [5].

The output samples of one of the ADC arms can be shown to be approximately described by

$$v_{ADC}(t_n) \approx \left| E_{laser} \left( \frac{t_n}{\beta_2 L} \right) \right|^2 \cdot \int |v_{disp}(t')|^2 \cdot \left| T \left( \frac{t' - t_n}{\beta_2 L} \right) \right|^2 dt' \quad (1)$$

where  $v_{disp}(t)$  is the sine (for upper arm) or cosine (for lower arm) of the applied RF signal, which

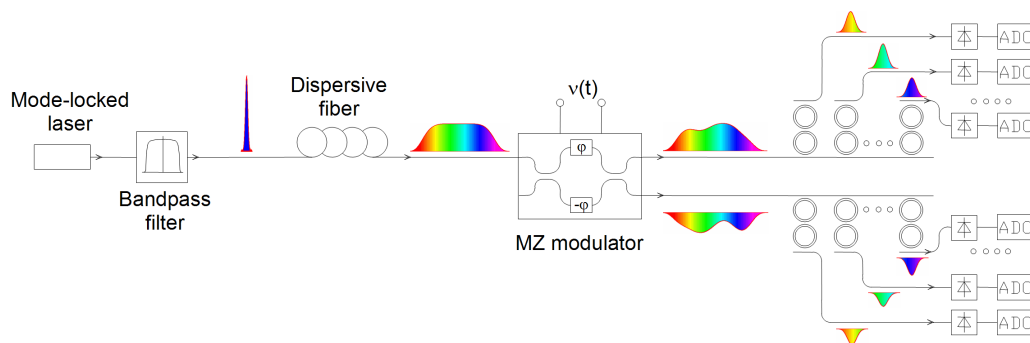
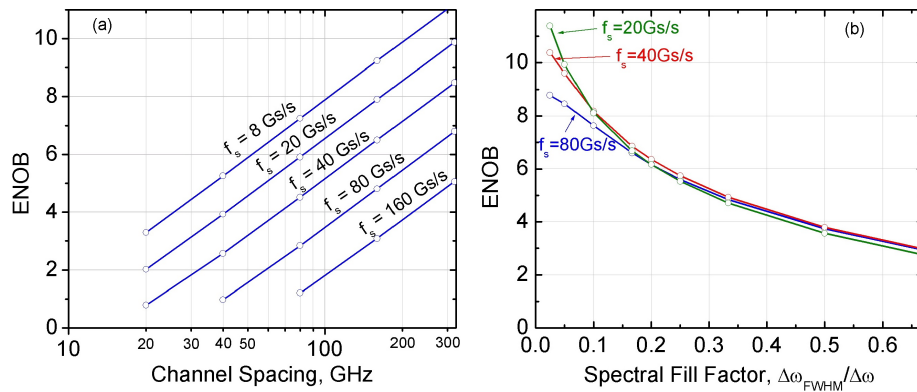


Fig. 4. Layout of the optically sampled wavelength-demultiplexed analog-to-digital converter.

is subsequently dispersed due to the chirp transferred from the chirped optical pulse train;  $T(\omega)$  is the frequency-dependent amplitude transmission function of each optical filter in the bank, the frequency is replaced by a function of time in the argument of this function according to time-frequency mapping;  $E_{laser}(\omega)$  is the envelope of the optical pulse in frequency domain. In deriving this expression, an approximation was used that the optical pulse spectrum remains constant within the bandwidth of the RF signal.

It follows from (1) that the ADC output differs from the applied RF signal even if ADC parameters have no errors. The factors contributing to this difference are (i) dispersion which is transferred to the RF signal, (ii) convolution with the optical filter transfer function, which can be interpreted to be due to the fact that each optical filter selects not just one frequency component but a range of frequencies, which corresponds to a time interval because of the time-frequency mapping, and (iii) laser spectrum variations across the RF bandwidth. Fig. 2 illustrates that ADC accuracy degradation due to dispersion and optical filter bandwidth can be substantial. For example, for a 40 Gs/s ADC with 80 GHz channel spacing and 25 GHz filter bandwidth, simulations predicts effective number of bits (ENOB) to be limited to about 4 bits.



**Fig. 2.** (a) ENOB limited by dispersion versus frequency spacing between the channels, and (b) ENOB limited by optical filter bandwidth versus spectral fill factor for several ADC sampling rates  $f_s$ .

Recovery of the original RF signal from the ADC output turns out to be not a straightforward task because the phase of the optical signal is lost in photodetection, preventing us from compensating dispersion in the digital domain. Another problem encountered is that the ADC is actually not sampling the applied RF signal but rather sine or cosine of this signal; sine and cosine create higher harmonics and the sampling rate of the ADC might not be sufficiently high to capture them, so spectral aliasing occurs. This makes it problematic to implement both dispersion compensation and deconvolution algorithm.

The ADC accuracy can also be reduced due to various imperfections of system components, such as (a) in the filter bank: errors in filter frequencies, mismatch between frequencies of the two filter banks, crosstalk between channels, channel-to-channel filter shape variations; (b) in MZ modulator: nonlinear dependence of phase shift on the driving voltage, loss dependence on the driving voltage (as in carrier-injection Si modulators), unequal splitting in MZ couplers; (c) in detection system: crosstalk between different sub-pulses for slow photodetectors, different sensitivities of photodiodes and individual ADCs, unequal channel path losses, etc. It is relatively straightforward to compensate for some of these errors at the post-processing stage. For example, errors due to imprecise positioning of the filter center frequencies can be dealt with by employing the non-uniform sampling theory. Other errors are harder to compensate, such as error due to dispersion. The situation becomes even more complicated when the error is caused

by several sources simultaneously. Therefore, a universal algorithm which can compensate for all kinds of errors simultaneously is necessary.

The algorithm we propose to use in order to compensate for deterministic ADC errors numerically on the post-processing stage is the following [6]. The relation between the input and output voltages of the ADC can be written as  $v_{\text{ADC}} = (1 + \hat{\varepsilon})v$ , where  $\hat{\varepsilon}$  is a nonlinear operator describing the distortion introduced by the system;  $\hat{\varepsilon}$  should be much smaller than 1 for a reasonable ADC system. The RF signal we want to find can then be expressed as

$$v = v_{\text{ADC}} - \hat{\varepsilon} v, \quad (2)$$

where the error  $\hat{\varepsilon} v$  is unknown. We start with a guess  $v^{(1)}$  for the RF signal assuming that this error is zero, i.e.  $v^{(1)} = v_{\text{ADC}}$ . Using this guess  $v^{(1)}$  as the RF driving voltage, we then run a system simulation and find the samples  $v_{\text{ADC}}^{(1)}$  which would be obtained from the ADC in this case. Because  $v_{\text{ADC}}^{(1)} = (1 + \hat{\varepsilon})v^{(1)}$ , the error can be found as  $\hat{\varepsilon} v^{(1)} = v_{\text{ADC}}^{(1)} - v^{(1)}$ . As our guess is close to the real RF signal, the error  $\varepsilon v^{(1)}$  is also close to the real error  $\hat{\varepsilon} v$ . Therefore, we substitute  $\hat{\varepsilon} v^{(1)}$  instead of  $\hat{\varepsilon} v$  into (1) and get an improved guess

$$v^{(2)} = v^{(1)} + (v_{\text{ADC}} - v_{\text{ADC}}^{(1)}) \quad (3)$$

The new guess can be further improved by running the ADC simulation and applying (3); this can be repeated until the desired accuracy is reached.

As an example, we consider the ADC system we are currently pursuing [4]. The pulse repetition rate  $f_R = 2\text{GHz}$  and  $N = 20$  channels give an overall sampling rate of  $40\text{GHz}$ . This system requires 20 ADCs sampling at  $2\text{GHz}$  (twice this number if both MZ outputs are used); such ADCs are currently commercially available. The filters have bandwidth of  $25\text{GHz}$  and are spaced by  $80\text{GHz}$ , requiring an optical source with at least  $1.6\text{THz}$  bandwidth. For this system, the ENOB is limited to about 4 by dispersion and filter bandwidth even if all system components are perfect. As a test case, we also assume rather poor ADC components: photodetectors with  $1\text{GHz}$  bandwidth, leading to overlap between the adjacent detected pulses, filter banks with randomly spaced center frequencies with a variance of  $15\text{GHz}$ , and a MZ modulator with  $30/70$  splitting ratio in the output coupler. The samples directly out of such ADC have  $\text{ENOB} \sim 1\text{bit}$ ; the proposed algorithm allows to improve ENOB to 10 bits in 11 iterations. Fig. 3 illustrates how the error is reduced with initial iterations. An ADC with better components requires fewer iterations.

The proposed algorithm was verified to be effective against the error sources listed above. For sufficiently low jitter and optical power on the photodetectors, the ENOB achievable using the proposed algorithm is limited only by the precision with which the ADC components are characterized. Because some ADC parameters may drift in time, e.g. filter center frequency can drift with temperature, periodic calibration by sampling of appropriate test signals derived from the mode-locked laser itself is needed. The proposed approach is generic and is expected to be effective for other photonic ADC configurations as well.

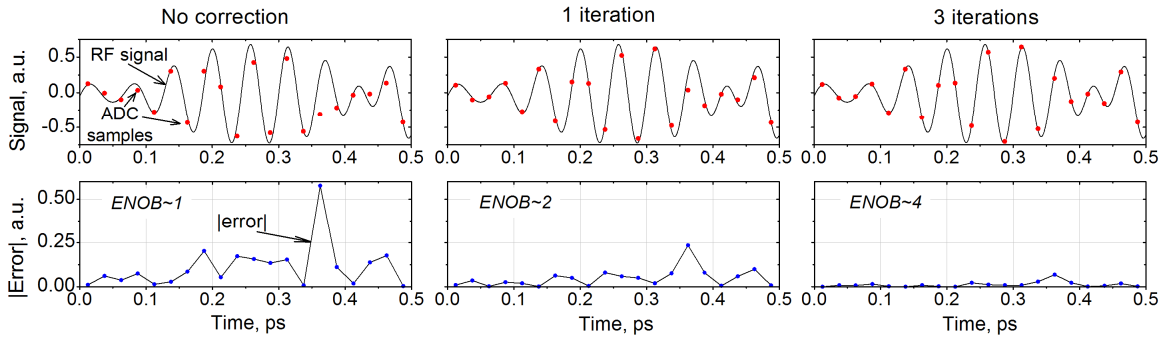


**Fig. 3.** Example of convergence of iterative error compensation algorithm.

## References

- [1] G.C. Valley, "Photonic analog-to-digital converters," *Opt. Express* 15(5): 1955-82 (2007).
- [2] J. Chen, J. Sickler, E.P. Ippen, and F.X. Kärtner, "Generation of low-timing-jitter femtosecond pulse trains with 2 GHz repetition rate via external repetition rate multiplication," *Opt. Lett.* 33(9): 959-961 (2008).
- [3] M.Y. Frankel, J.U. Kang, R.D. Esman, "High-performance photonic analogue-digital converter," *Electron. Lett.* 33(25): 2096-97 (1997).
- [4] F.X. Kärtner, et. al., "Photonic analog-to-digital conversion with electronic-photonic integrated circuits", *Proc. SPIE* 6898: 689806 (2008).
- [5] J.C. Twichell, R. Helkey, "Phase-encoded optical sampling for analog-to-digital converters," *IEEE Phot. Tech. Lett.* 12(9): 1237-39 (2000).
- [6] A. Khilo, J. R. Birge, F. X. Kärtner, "Adaptive Error Compensation for Photonic Analog-to-Digital Converters," Paper CMII4, *Conference on Lasers and Electro-Optics (CLEO)*, San Jose, CA, May 4-9, 2008.

## Integrated, low jitter, 400 MHz femtosecond waveguide laser

### Sponsors

Defense Advanced Research Project Agency (DARPA OAWG Program) HR0011-05-C-0155  
 Defense Advanced Research Project Agency (DARPA EPIC Program) W911NF-04-1-0431

### Project Staff

Hyunil Byun, Dominik Pudo, Sergey Frolov, Amir Hanjani, Joseph Shmulovich, Professor Erich P. Ippen, and Professor Franz X. Kärtner

High repetition rate sources of femtosecond laser pulses are necessary for a variety of applications including optical arbitrary waveform generation, frequency metrology [1] and photonic analog to digital conversion [2]. Passive mode-locking enables low jitter femtosecond pulses while alleviating the need for an external microwave oscillator. In the past, both polarization additive-pulse mode-locking (P-APM) and/or saturable Bragg reflector (SBR) mode-locking [3,4] have been used with fiber and waveguide lasers, with the latter leading to more compact cavities and fewer required components. Recent experimental demonstrations of high repetition rate fiber lasers based on the SBR approach achieved repetition rates as high as 3 GHz [5] and a timing jitter as low as 37 fs in the frequency range [1 kHz, 10 MHz] [6]. Nevertheless, integrated versions of such lasers have the additional benefits of being mass-producible with reduced footprint, and increased stability. Early attempts of passively mode-locked lasers using an erbium-doped waveguide (EDW) as a gain medium and an SBR as a mode-locking element were limited to lower rep rate and picosecond pulse operation [7,8]. Femtosecond operation of such lasers [9] was only achieved by employing nonlinear polarization rotation mode-locking, which is difficult to integrate. In addition, in all of these cases the cavity comprised free-space optics in between the SBR and the EDW.

In this report, we demonstrate a 394 MHz, self-starting, passively mode-locked femtosecond laser based on planar silica waveguide technology. The laser generates 440 fs pulses with an average output power of 1.2 mW for a pump power of 400 mW.

The experimental setup is depicted in Fig. 1. The laser cavity consists of a 5 cm section of erbium doped aluminosilicate waveguide with a group-velocity dispersion of  $30 \text{ fs}^2/\text{mm}$ . A 20 cm section of phosphorous-doped silica waveguide with a dispersion of  $-25 \text{ fs}^2/\text{mm}$  is used to obtain a net anomalous intracavity dispersion to enable soliton mode-locking [10]. The Er-doped section and the P-doped silica-glass section have a effective mode area of  $10 \mu\text{m}^2$  and  $40 \mu\text{m}^2$ , respectively. A loop mirror is used at one end to provide 10% output coupling, while the other end is butt-coupled to an external SBR. The SBR is a commercial unit with 14% modulation depth, a 2 ps recovery time, and a saturation fluence of  $25 \mu\text{J}/\text{cm}^2$ . Pump power is provided by an external 980 nm laser diode coupled into the waveguide chip. The laser was operated with 400 mW of cavity-coupled pump power; the intracavity signal power was measured to be 12 mW, corresponding to a 30 pJ intracavity pulse energy. The output pulses with an average power of 1.2 mW are then amplified to 18 mW using an EDFA (980 nm pump, 350 mA), detected using a 10 GHz photodiode, and measured with a 500 MHz sampling scope and a signal source analyzer (Agilent E5052).

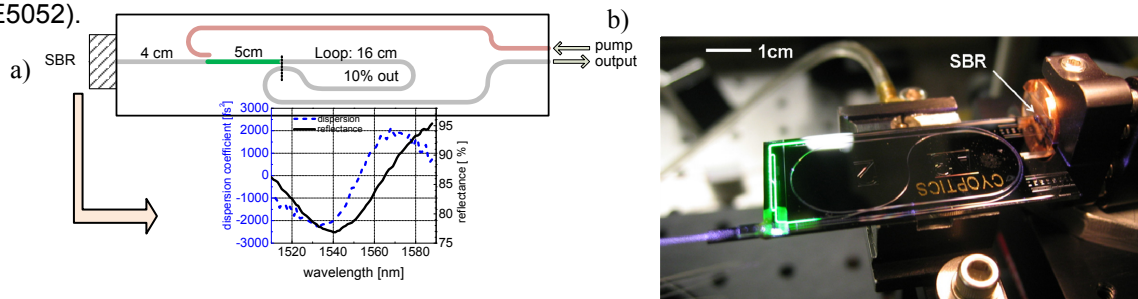


**Fig. 1.** a) Integrated laser layout b) Snapshot of the laser setup. Inset on the left depicts the SBR's reflection and dispersion spectr

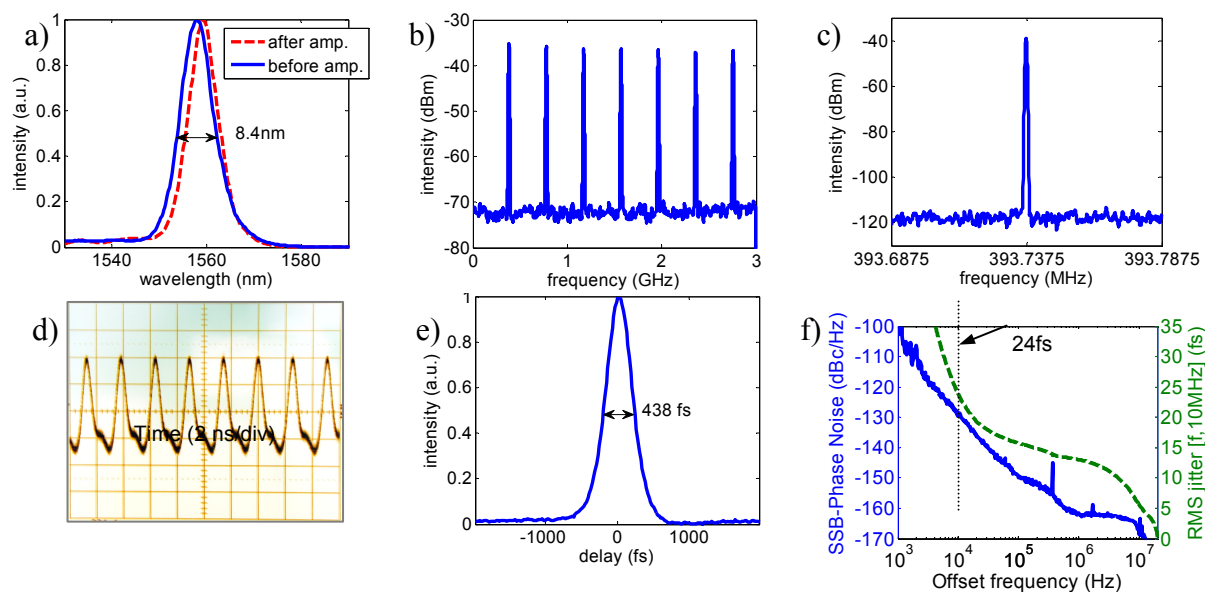


**Fig. 2.** Measurement traces at 400 MHz: a) normalized optical spectrum before and after amplification, b) Rf spectrum (3 GHz span, 10 MHz resolution), c) RF spectrum (100 kHz span, 500 Hz resolution), d) 10 second persistence trace, e) background free autocorrelation trace and f) single side band (SSB) phase noise of the first harmonic of the laser.

Figure 2 depicts the measurement results. The persistence trace shows excellent signal stability, while the RF spectrum in c) indicates a side-mode suppression ratio of 80 dB. The 8.4 nm FWHM optical bandwidth before amplification implies 300 fs duration transform-limited pulses. After amplification, the optical bandwidth decreases to 7.4 nm, corresponding to 340 fs. The autocorrelation measurement yielded a pulse duration of 440 fs. The difference is attributed to incomplete compensation of the chirp added by the erbium-doped fiber. The laser was self-starting. Figure 2(f) shows the phase noise of the first harmonic (394 MHz) of the laser. The timing jitter integrated from 20 MHz progressively down to 1 kHz is also shown. The timing jitter integrated from 10 kHz to 20 MHz is 24 fs. No polarization control or active stabilization is required, and the laser is self-starting. Higher repetition rates can be achieved by further reducing the cavity length while optimizing the pumping scheme.

## References

- [1] S. T. Cundiff, "Metrology - New generation of combs," *Nature* 450: 1175-1176 (2007).
- [2] A. Bartels, et al., "Ultrafast time-domain spectroscopy based on high-speed asynchronous optical sampling," *Review of Scientific Instruments* 78(3): 035107 (2007).
- [3] H.A. Haus, "Theory of mode-locking with a fast saturable absorber," *J. Appl. Phys.* 46(7): 3049-3058 (1975).
- [4] R. Paschotta and U. Keller, "Passive mode locking with slow Saturable absorbers," *Appl. Phys. B* 73(7): 653-662 (2001).

[5] J. Chen, et al., "Fundamentally Mode-locked 3 GHz Femtosecond Erbium Fiber Laser," paper presented at the Conference on Ultrafast Phenomena, Stresa, Italy, June 9-13, 2008.

[6] H. Byun, D. Pudo, J. Chen, E.P. Ippen and F.X. Kärtner, "High repetition rate, 491 MHz, femtosecond fiber laser with low timing jitter," *Opt. Lett.*, forthcoming.

[7] E.R. Thoen, et al., "Erbium-ytterbium waveguide laser mode-locked with a semiconductor saturable absorber mirror," *IEEE Photon. Technol. Lett.* 12(2): 149-151 (2000).

[8] J.B. Schlager, et al., "Passively mode-locked glass waveguide laser with 14-fs timing jitter," *Opt. Lett.* 28(23): 2411-2413 (2003).

[9] D.J. Jones, et al., "116-fs soliton source based on an Er-Yb codoped waveguide amplifier," *IEEE Photon. Technol. Lett.* 10(5): 666-668 (1998).

[10] F.X. Kärtner and U. Keller, "Stabilization of solitonlike pulses with a slow saturable absorber," *Opt. Lett.* 20(1): 16-18 (1995).

## Nanophotonics

### Widely-Tunable Silicon Nanophotonic Circuits for Telecom Applications

#### Sponsors

Defense Advanced Research Project Agency (DARPA EPIC Program) W911NF-04-1-0431  
Pirelli Labs, Italy

#### Project Staff

Miloš A. Popović, Tymon Barwicz, Fuwan Gan, Marcus S. Dahlem, Charles W. Holzwarth, Peter T. Rakich, Prof. Henry I. Smith, Prof. Erich P. Ippen and Prof. Franz X. Kärtner

Numerous photonic-circuit capabilities have been envisioned based on microring-resonator structures including linear filters, nonlinear devices, and ‘slow-light’ delay lines. Such circuits can support applications such as chip-scale tunable/reconfigurable optical add-drop multiplexers (T/R-OADMs), high-rate photonic sampling systems, and intrachip communication networks for microprocessors. The majority of these applications requires strong-confinement (SC) waveguides based on high index contrast (HIC) in which bending loss is negligible at bend radii of a few microns. Silicon as waveguide core allows for tunable circuits through its large thermo-optic coefficient. However, in the SC regime, realization of devices with acceptable performance for telecom applications is prevented by the strong sensitivity of SC devices to sidewall roughness, dimensional variations and polarization state [1].

In the course of this work, we proposed optimal silicon waveguide [1] and microheater [2] designs for maximally-tunable filters, and demonstrated thermo-optically tunable microring-resonator filters in silicon with the largest full-FSR tuning range, exceeding 20nm, and a high tuning energy efficiency of  $30\mu\text{W}/\text{GHz}$  [2]. We also designed and demonstrated the first tunable high-order channel add-drop filters based on silicon microring resonators for chip-scale nanophotonic T/R-OADMs [3].

Thermo-optic tuning has been widely used in microring filters because it can induce large refractive index changes without optical loss. A large tuning range is necessary to enable microring filters to operate over the whole C-band. We designed novel heater structures that maximize tuning range by minimizing the temperature difference between the resonator and the heater at a distance that avoids optical loss (see Fig. 1a-c and Fig. 1d, inset). The heater

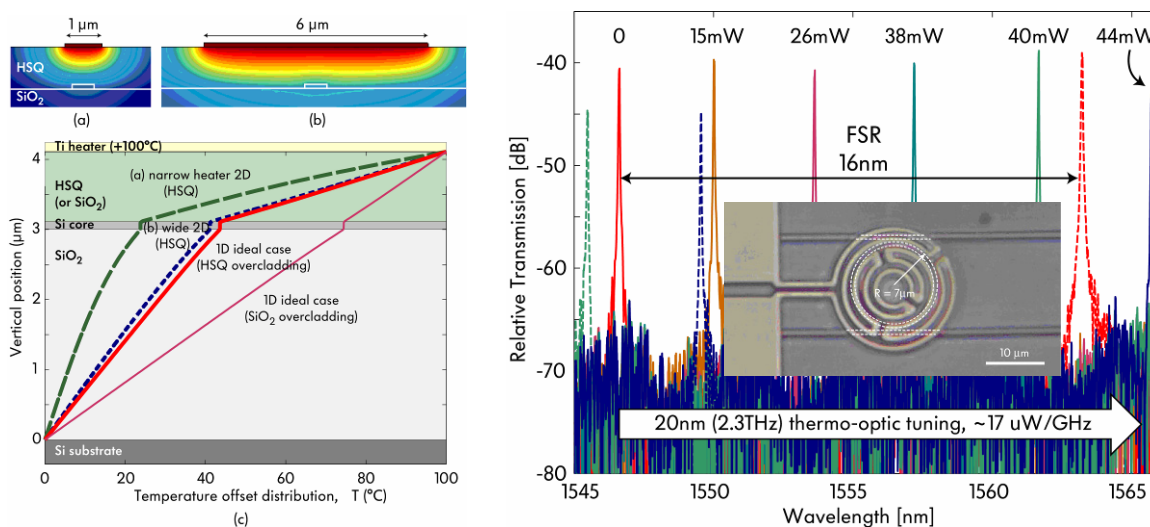


**Fig. 1.** A wide heater-trace cross-section allows a lower temperature drop from the heater to the silicon resonator’s waveguide core, enabling maximal thermo-optic tuning range [2].

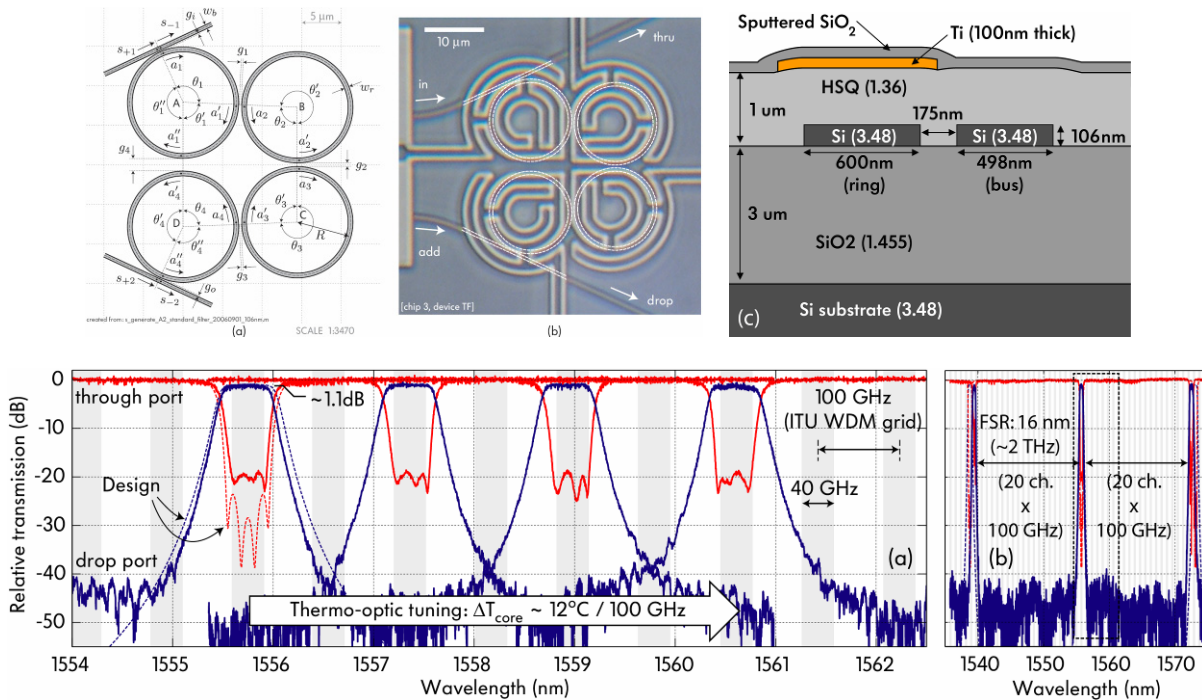


**Fig. 2.** Fourth-order, silicon microring-resonator filter layout, optical micrograph, and waveguide cross-section. Design and experimental responses match showing wide tuning of low-loss, sharp, flat-top tunable passbands [3].

temperature is the tuning limiting parameter. Metal heaters cannot be made arbitrarily thick due to fabrication constraints. Hence, current density cannot be decreased arbitrarily and electromigration sets a limit on the heater operating temperature.

A wide tuning range is achieved by making the heat injection surface (heaters) approximate a 1D heat flow in the vertical through-the-ring direction. As shown in Fig.1(a-b), a narrow heater provides a more "diffracting" heat flow than a wide heater. In Fig.1(c), we note that the quasi-1D heat flow of a 6 $\mu$ m-wide heater (blue dotted) enables a larger temperature at the waveguide for a given heater temperature than the narrow heater (green dashed). A hydrogen silsequioxane (HSQ) uppercladding was chosen in our devices for its excellent gap-filling and self-planarization capabilities. An SiO<sub>2</sub> uppercladding, however, can further enhanced the tuning efficiency by 80% due to the higher thermal conductivity of SiO<sub>2</sub> with respect to HSQ. Fig. 1d shows the experimental spectra demonstrating 20nm tuning of a silicon microring resonator with about 40mW electrical power in the microheater. The fabricated device is shown in Fig. 1d, inset.

Because silicon waveguides have large dimensional sensitivities, a novel, 6:1 aspect ratio, thin-core Si waveguide design was proposed and used that optimizes propagation loss, tolerances and tuning properties [1]. Based on this waveguide, we also demonstrated the first high (4th) order, tunable microring-resonator filters in silicon [3] (Fig. 2a-b), with about 1dB drop-loss and 2 THz FSR (Fig. 2d-e). For widely tunable filters, change of the filter passband shape with wavelength tuning is a concern, because the coupling between rings and waveguides in the filter is a function of both temperature and wavelength. We employed a design that balances the temperature and wavelength dependences, which are of opposite sign, to achieve an approximately tuning-independent filter shape [4]. Together with our previous work on integrated polarization diversity and hitless switching, these elements enable chip-scale fully reconfigurable OADMs.

## References

- [1] M.A. Popović, T. Barwicz, E.P. Ippen and F.X. Kärtner, "Global design rules for silicon microphotonic waveguides: sensitivity, polarization and resonance tunability," paper CTuCC1, *Conference on Lasers and Electro-Optics (CLEO)*, May 2006.
- [2] F. Gan, T. Barwicz, M.A. Popović, M.S. Dahlem, C.W. Holzwarth, P.T. Rakich, H.I. Smith, E.P. Ippen and F.X. Kärtner, "Maximizing the Thermo-Optic Tuning Range of Silicon Photonic Structures," Paper TuB3.3, *IEEE/LEOS Photonics in Switching Conference*, San Francisco, CA, Aug 2007.
- [3] M.A. Popović, T. Barwicz, M.S. Dahlem, F. Gan, C.W. Holzwarth, P.T. Rakich, H.I. Smith, E.P. Ippen and F.X. Kärtner, "Tunable, Fourth-Order Silicon Microring-Resonator Add-Drop Filters," Paper 1.2.3, *European Conference on Optical Communication (ECOC)*, Berlin, Germany, 2007.
- [4] M. Popović, Theory and design of high-index-contrast microphotonic circuits, Ph.D. Thesis, Dept. of Electrical Engineering and Computer Science, MIT, 2008.

## Loop-Coupled Resonators Enabling Optimally Sharp, Dispersionless Optical Filters and ‘Slow-Light’ Delay Lines

### Sponsors

Defense Advanced Research Project Agency (DARPA EPIC Program) W911NF-04-1-0431  
Pirelli Labs, Italy

### Project Staff

Miloš A. Popović, Tymon Barwicz, Peter T. Rakich, Marcus S. Dahlem, Charles W. Holzwarth, Fuwan Gan, Michael R. Watts, Prof. Henry I. Smith, Prof. Franz X. Kärtner and Prof. Erich P. Ippen

There is a continuing need to develop both highly spectrally efficient (sharp amplitude responses and linear phase) and compact-footprint resonant structures, motivated in part by emerging applications that demand spectral efficiency, like photonic networks on a microprocessor. Slow-wave structures for optical delay lines and nonlinear applications also require high bandwidth utilization to permit the greatest delays in pulse lengths and maximal resonant field enhancement. For both scenarios, series-coupled-cavity filters [1] give suboptimal, all-pole flat-top responses, and are highly dispersive over much of the passband as limited fundamentally by the Kramers-Kronig constraint.

In this work, a new class of resonant optical structures was proposed [2] and experimentally demonstrated [3]. It involves coupling resonators in a loop (Fig. 1a-b), which serves to give zeros in transmission responses at finite detuning from the passband either on the real frequency axis or in the complex-frequency plane. This serves to enable both optimally sharp amplitude responses, and simultaneously linear-phase and box-amplitude-shape spectral responses, demonstrated for the first time in any optical structure [2,4]. First, a new physical parameter – the loop-coupling phase (LCP) – was identified and shown to be directly related to control of transmission nulls. Second, it was shown that loop-coupled resonator geometries can be used to synthesize optimally sharp filters (Fig. 1c-e) and even simultaneously rectangular-amplitude and linear-phase filters that are not subject to the Kramers-Kronig amplitude-phase relationship/constraint. The proposed resonator geometry achieves optimal responses in a very compact footprint and is inherently robust to dimensional errors [2,4].

The new salient features of these structures are: (1) loop-coupling of resonators (Fig. 1a-b), (2) phase-sensitive (positive/negative/arbitrary-phase) coupling achieved through geometrical configuration and use of high-order resonances (Fig. 1b), (3) optional (weak) direct coupling between the input and output waveguides leading to response nulls, (4) existence of a direct mapping of optical parameters to synthesis of known linear-phase flat-top passband functions.

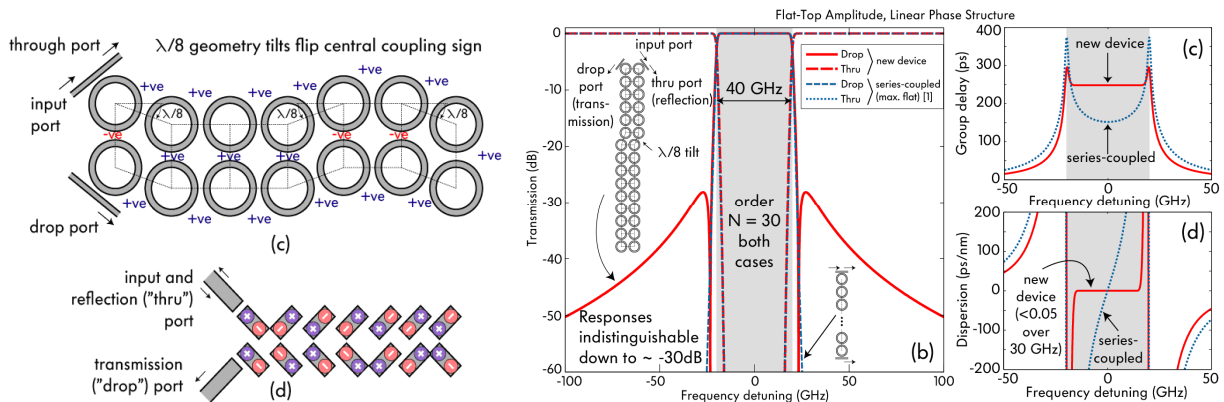


**Fig. 1.** Simultaneously dispersionless (linear-phase) and flat-top add-drop filters (or slow-light delay lines) based on the proposed loop-coupled resonator concept, applicable to microring or standing-wave cavity geometries [1].

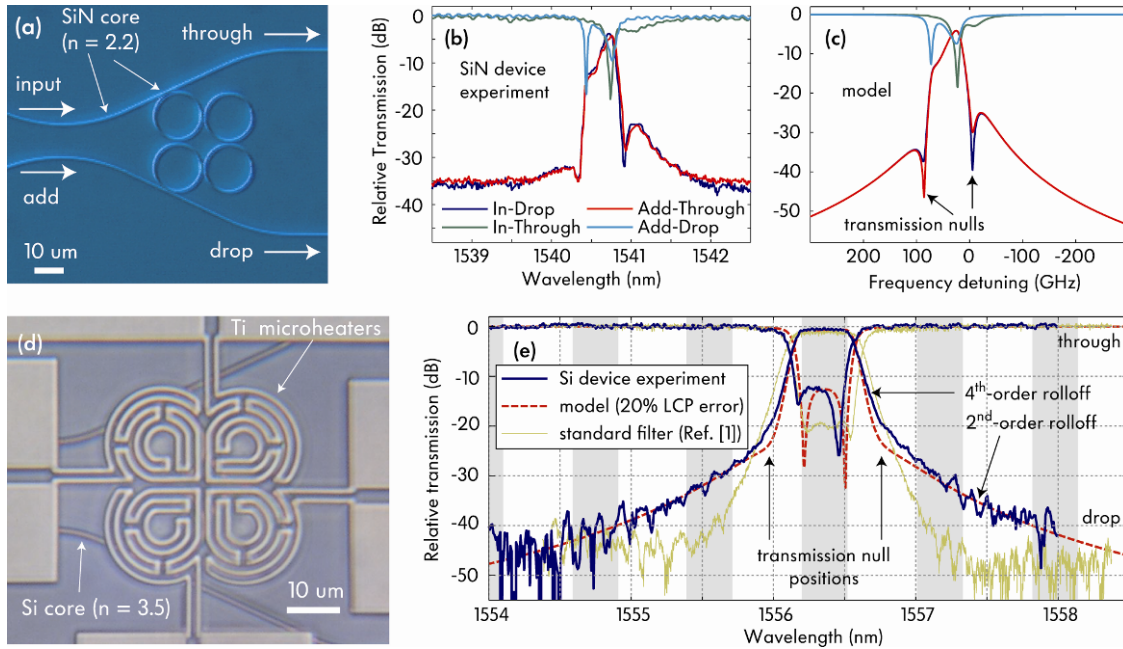


**Fig. 2.** Experimental demonstration of optimally-sharp 4<sup>th</sup> order microring filters in (a-c) SiN and (d-e) silicon microrings [3]. In (b-c), the characteristic transmission nulls are demonstrated and are consistent with theory.

Analogs of these devices are known in circuit theory and microwave design but these concepts have not yet been utilized in optics. Furthermore, optical structures based on traveling-wave resonators are more general, and enable a new class of optical responses not accessible in practical microwave structures.

We also show the first experimental demonstration of loop-coupled resonator filters, designed to provide an optimally sharp 4<sup>th</sup>-order add-drop filter, including the confirmation of transmission null interference mediated by the LCP. Two designs are used: a static microring filter in Si-rich SiN, and a thermally tunable Si microring filter. The Si filter is designed to give a 4<sup>th</sup>-order optimally sharp response with 2 zeros and a 65GHz 3dB bandwidth, while the SiN design has the same response design but with a 50 GHz bandwidth. The SiN filter is shown in Fig. 2(a). Fig. 2(b) shows the experimentally measured bar- and cross-state responses from both input ports, clearly demonstrating the sharp nulls on each side of the passband induced by the loop coupling and LCP. The device model in Fig. 2(c) shows that the reason for the distorted shape of the passband is that the ring cavities are misaligned in frequency by about 20 GHz left to right, and 40 GHz up to down in Fig. 1(a). Dose compensation in the electron-beam lithography was used to compensate for the various lithography and electromagnetically induced sources of resonance frequency misalignment.

The fundamental performance improvements enabled by the extra degrees of freedom (couplings and loop-coupling phase parameters) in the proposed loop-coupled resonator topology promise an important place for these structures in photonic circuits. They provide superior add-drop filter properties in comparison to standard linear coupled cavities at no cost in complexity or tolerances, simply by employing previously unused degrees of freedom. These structures may also play an important role in slow-light structures for optical pulse buffers and nonlinear devices, as well as in microwave photonics where signals may be more sensitive to phase linearity.

**References**

- [1] B.E. Little, S.T. Chu, H.A. Haus, J. Foresi, and J.P. Laine, "Microring-resonator channel dropping filters," *J. Lightwave Technol.* 15: 998-1005 (1997).
- [2] M.A. Popović, "Sharply-defined optical filters and dispersionless delay lines based on loop-coupled resonators and 'negative' coupling," paper CThP6, *Conference on Lasers and Electro-Optics (CLEO)*, May 6-11, 2007.
- [3] M.A. Popović, T. Barwicz, P.T. Rakich, M.S. Dahlem, C.W. Holzwarth, F. Gan, L. Socci, M.R. Watts, H.I. Smith, F.X. Kärtner and E.P. Ippen, "Experimental demonstration of loop-coupled microring resonators for optimally sharp optical filters," Paper CTuNN3, *Conference on Lasers and Electro-Optics (CLEO)*, San Jose, CA, May 4-9, 2008.
- [4] M. Popović, Theory and design of high-index-contrast microphotonic circuits, Ph.D. Thesis, Dept. of Electrical Engineering and Computer Science, MIT, 2008.

## Low-Loss Bloch Waves in Open Guided-Wave Structures for Efficient Nanophotonic Waveguide Crossings

### Sponsors

Defense Advanced Research Project Agency (DARPA Intrachip Program) W911NF-06-1-0449

### Project Staff

Miloš A. Popović, Prof. Erich P. Ippen and Prof. Franz X. Kärtner

Low-loss, compact, broadband silicon-waveguide crossing arrays and active structures are proposed based on periodicity-matched multimode focusing. Simulations show loss of 0.045dB/crossing and  $>200\text{nm}$  bandwidth in a typical example, a factor of 5-10 improvement over the state of the art. Correspondence to low-loss, structure-matched Bloch-waves is demonstrated. Strong-confinement (SC) waveguides based on high index contrast support dense photonic device integration, promising complex microphotonic circuits such as on-chip wavelength multiplexers or entire photonic networks on a microprocessor die. As device density and complexity increase in a planar photonic circuit, efficient waveguide crossings quickly become of paramount importance because the number of waveguide crossings required rises quickly and tolerable levels of loss and crosstalk per crossing accordingly drop to very small limits. Straightforward crossing of single-mode SC waveguides leads to strong diffraction losses, and a number of improvements have been proposed, promising 0.2-0.4dB of loss. While such losses may seem small, they are not acceptable in dense nanophotonic circuits where one may thus accumulate 10-20dB of loss after 50 crossings.

In this work, ultra-low loss waveguide crossing arrays are proposed by combining a multimode focusing concept with matching of the field pattern and dielectric structure periodicities to produce a low-loss Bloch wave. This crossing array is a unified structure (Fig. 1) that permits 10s or 100s of crossings at a dense pitch of only a few microns. Finite-difference time-domain (FDTD) simulations of an example silica-clad, Si-core waveguide crossing array show  $\sim 0.04\text{dB/crossing}$  (Fig. 1). This is 5-10 times lower loss than previously proposed designs in nearly identical waveguides and material systems. Since the designs are broadband, they are also expected to be tolerant to fabrication errors. This concept is not without previous analogue; in the 1960's Goubau and Schwering proposed so-called beam waveguides composed of a periodic array of confocal lenses in free space. In the proposed periodic structures, the crossing regions correspond to the free-space regions in the beam waveguide, and the waveguide regions correspond to the lenses. However, the microphotonic structure has virtually no reflection at each period and can approach very low losses, unlike the beam waveguide, where the lenses produce reflection loss.

Furthermore, use of multimode interference to create a low-loss mode beat pattern that “self-confines” may be useful for other novel devices, such as low-loss, low-contact-resistance modulators.

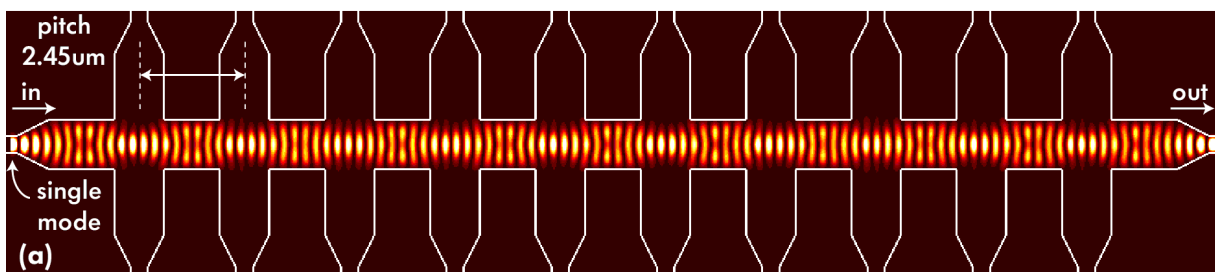


**Fig. 1.** Simulation of an ultra-low-loss waveguide crossing array for strong-confinement nanophotonic circuits, based on a periodicity-matched low-loss Bloch wave that simulates a periodically focusing field pattern [1].

**References**

- [1] 1. M.A. Popović, E.P. Ippen and F.X. Kärtner, "Low-Loss Bloch Waves in Open Structures and Highly Compact, Efficient Si Waveguide-Crossing Arrays," Paper MF5, *20th Annual Meeting of the IEEE Lasers and Electro-Optics Society (LEOS)*, Lake Buena Vista, Florida, Oct 2007.

## Super-Collimation in a 2-D Silicon Rod-Based Photonic Crystal

### Sponsors:

AFOSR Contracts FA9550-07-C-0005 and FA9550-07-1-0014

DARPA Contract 2003-IT-674

MARCO and its participating companies

NSF MRSEC under DMR 02-13282

ARO through the Institute for Soldier Nanotechnologies under contract No. W911NF-07-D-0004

### Project Staff:

Marcus S. Dahlem, Ta-Ming Shih, André Kurs, Dr. Gale S. Petrich, Prof. Marin Soljačić, Prof. Leslie A. Kolodziejski, Prof. Erich P. Ippen

Photonic crystals (PhCs) are engineered structures with peculiar dispersion characteristics that can control light at very small scales[1-9]. Careful design of such structures enables the propagation of optical beams without diffraction, referred to as super-collimation[2-6, 8, 9]. This linear effect is a natural result of the unique dispersive properties of PhCs. Centimeter-scale super-collimation in a large-area 2D silicon photonic crystal of air-holes has been reported[6, 8]. The complementary structure – silicon rods in air – presents a higher challenge, in both fabrication and characterization. In such structure, super-collimation occurs for TM-like radiation, resulting in weaker out-of-plane radiation (when compared to the inverse structure), harder to detect. In addition, the super-collimation bandwidth is shown to be narrower for the rods-based structure. We have recently fabricated and reported the first experimental demonstration of super-collimation in a 2D PhC of silicon rods in air[10].

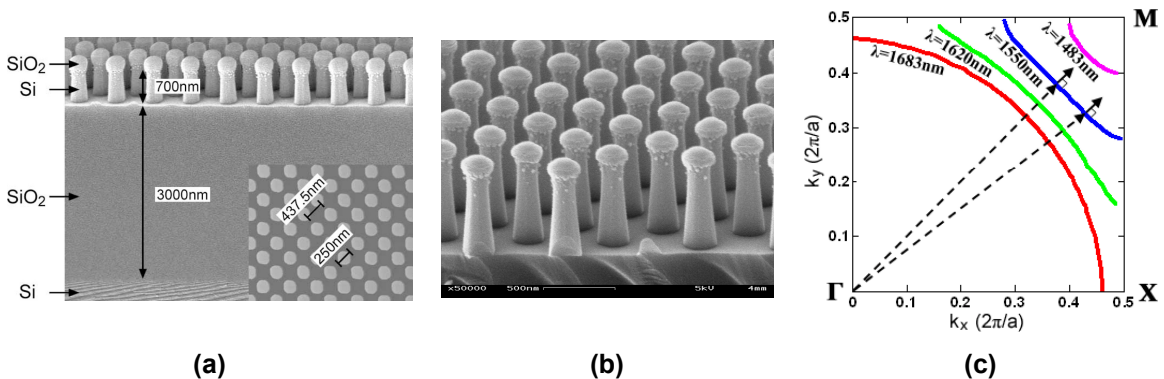


**Figure 1** – 2D Photonic crystal of silicon rods in air: **(a-b)** scanning electron micrographs (SEMs) of the fabricated large-area structure; **(c)** equifrequency contours of the PhC, showing flat regions in the  $\Gamma$ -M direction for wavelengths around 1550nm.

The 2D PhC was patterned with a square lattice of silicon rods in air – Figure 1(a-b). The structure was fabricated on a silicon-on-insulator (SOI) wafer with a 700nm-thick silicon layer over a 3 $\mu$ m-thick oxide layer, using interference lithography and reactive ion etching[11]. The lattice constant is  $a = 437.5\text{nm}$  and the rod radius is  $r = 125\text{nm}$ , resulting in a super-collimation wavelength around 1550nm for TM-like radiation (electric field perpendicular to the 2D plane), in the lowest energy band. The SEMs show that the rods are tapered, resulting in some deviation from the ideal case of perfectly cylinder rods. The projected band structure for the fabricated structure is shown in Figure 1(c). Around  $\lambda = 1550\text{nm}$ , the computed equifrequency contours are flat in the  $\Gamma$ -M direction and show little spatial dispersion in the transverse wavevector, leading to super-collimation.

When comparing the rod- and hole-based structures, there are three major differences that can influence the performance and/or application of both configurations: (i) the rod-based PhC have TM-like super-collimation eigenmodes, while the hole-based equivalent has TE-like; (ii) in the rod-based configuration, the mode is less confined in the silicon layer, resulting in higher sensitivity to index changes of the surrounding dielectric; and (iii) the wavelength bandwidth for the rod-based PhC is narrower than its counterpart. This bandwidth variation is illustrated in Figures 2(a-b). For a given initial beam waist, the range of wavelengths that return a large diffraction length (denoted by SC length) is narrower for the case of the rod-based structure.

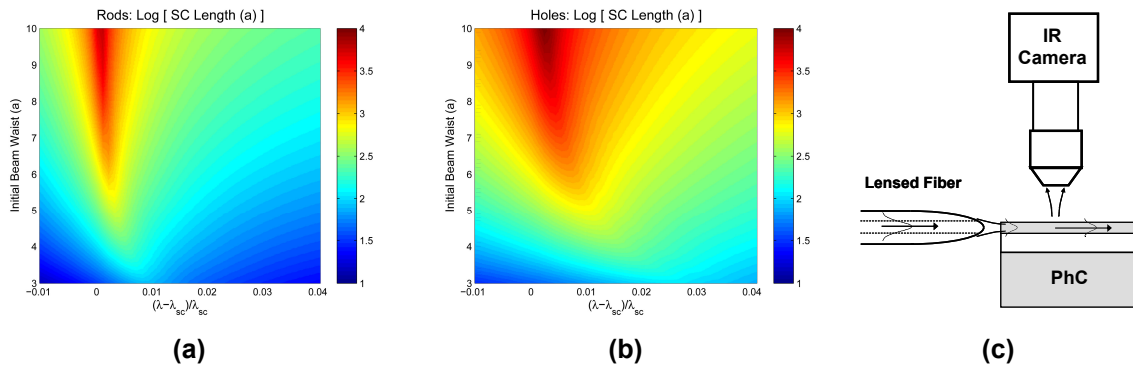


**Figure 2 – (a-b)** Sensitivity of the diffraction length SC to changes in the wavelength of the incident beam. The hole-based PhC is the one described in [8]; **(c)** Schematic of the experimental measurement apparatus.

Interference lithography enables fabrication of centimeter-scale samples, and the size of the tested PhCs varied from 2mm to 7mm. Light from a tunable laser source was coupled into the PhC sample through a high NA single-mode (SM) lensed fiber with a spot size of  $1.5\mu\text{m}$  full-width at half-maximum (FWHM) and a working distance of about  $8\mu\text{m}$ . The light scattered out of the plane was then detected with an infrared (IR) camera, as illustrated in Figure 2(c).

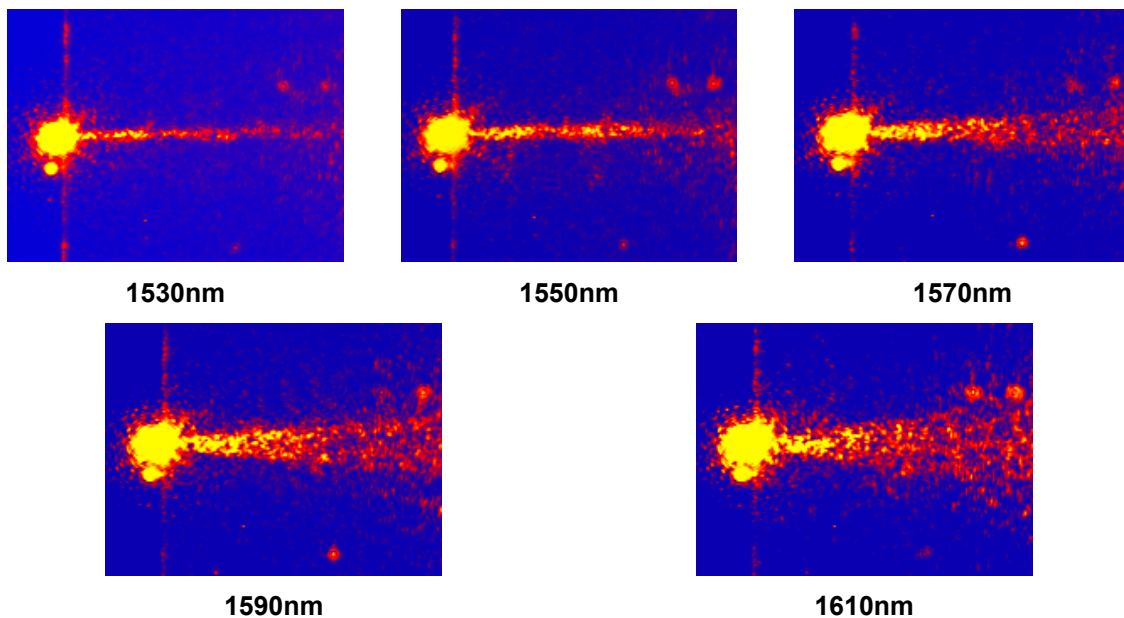


**Figure 3 – IR** images showing the wavelength dependence of the propagating beam inside the 2D PhC. Super-collimation is observed around  $\lambda = 1530\text{nm}$ , and the beam diffracts as the wavelength increases.

The experimentally observed wavelength for super-collimation was around 1530nm, and for different wavelengths the beam exhibits diffraction-like behavior. This is explained by the curvature of the equipfrequency contours. Figure 3 shows IR images of the wavelength dependence of the propagating beam inside the PhC. No accurate loss measurement was performed over the sample, but the bright out-of-plane scattering is indication of large loss. The images shown are about 125 $\mu$ m-long, but the effect was observed over  $\sim$ 0.5mm. A rough loss estimation return values of  $\sim$ 20dB/mm.

The discrepancy between the measured and simulated super-collimation wavelength is about 1%. The large value estimated for the loss is mainly due to short scale disorder, such as fabrication roughness. In addition to optical interconnects[8], super-collimation can be used to develop optofluidic technology[12]. In particular, the rod-structure is suitable for sensing applications due to its higher sensitivity to changes of the surrounding index of refraction.

### References

- [1] J. D. Joannopoulos, S. G. Johnson, J. N. Winn, and R. D. Meade, *Photonic Crystals: Molding the Flow of Light (Second Edition)*, Princeton University Press, 2008.
- [2] H. Kosaka, T. Kawashima, A. Tomita, M. Notomi, T. Tamamura, T. Sato, and S. Kawakami, "Self-collimating phenomena in photonic crystals," *Applied Physics Letters*, vol. 74, pp. 1212-1214, 1999.
- [3] H. Kosaka, T. Kawashima, A. Tomita, T. Sato, and S. Kawakami, "Photonic-crystal spot-size converter," *Applied Physics Letters*, vol. 76, pp. 268-270, 2000.
- [4] L. J. Wu, M. Mazilu, and T. F. Krauss, "Beam steering in planar-photonic crystals: From superprism to supercollimator," *Journal of Lightwave Technology*, vol. 21, pp. 561-566, 2003.
- [5] L. Wu, M. Mazilu, J.-F. Gallet, and T. F. Krauss, "Square lattice photonic-crystal collimator," *Photonics and Nanostructures - Fundamentals and Applications*, vol. 1, pp. 31-36, 2003.
- [6] M. Dahlem, "Optical Studies of Super-Collimation in Photonic Crystals," SM thesis, Department of Electrical Engineering and Computer Science, Massachusetts Institute of Technology, Cambridge, MA, 2005.
- [7] S. N. Tandon, M. Soljacic, G. S. Petrich, J. D. Joannopoulos, and L. A. Kolodziejski, "The superprism effect using large area 2D-periodic photonic crystal slabs," *Photonics and Nanostructures-Fundamentals and Applications*, vol. 3, pp. 10-18, 2005.
- [8] P. T. Rakich, M. S. Dahlem, S. Tandon, M. Ibanescu, M. Soljacic, G. S. Petrich, J. D. Joannopoulos, L. A. Kolodziejski, and E. P. Ippen, "Achieving centimetre-scale supercollimation in a large-area two-dimensional photonic crystal," *Nature Materials*, vol. 5, pp. 93-96, 2006.
- [9] D. W. Prather, S. Y. Shi, J. Murakowski, G. J. Schneider, A. Sharkawy, C. H. Chen, B. L. Miao, and R. Martin, "Self-collimation in photonic crystal structures: a new paradigm for applications and device development," *Journal of Physics D-Applied Physics*, vol. 40, pp. 2635-2651, 2007.
- [10] T. Shih, M. Dahlem, A. Kurs, G. Petrich, M. Soljacic, E. Ippen, L. Kolodziejski, K. Hall, and M. Kesler, "Supercollimation in Photonic Crystals Composed of Nano-scale Silicon Rods," CTuDD7, Conference on Lasers and Electro Optics (CLEO), 2008.
- [11] T.-M. Shih, "Super-Collimation in a Rod-Based Photonic Crystal," SM thesis, Department of Electrical Engineering and Computer Science, Massachusetts Institute of Technology, Cambridge, MA, 2007.
- [12] D. Psaltis, S. R. Quake, and C. H. Yang, "Developing optofluidic technology through the fusion of microfluidics and optics," *Nature*, vol. 442, pp. 381-386, 2006.

## Frequency Swept Lasers

### Frequency Swept Lasers and Fourier Domain Mode Locking (FDML)

#### Sponsors

National Institutes of Health – R01-CA75289-06, R01-EY11289-18

National Science Foundation – ECS-01-19452, BES-0119494

Air Force Office of Scientific Research – F49620-01-1-0186, F49620-01-01-0084

Natural Sciences and Engineering Research Council of Canada (NSERC Canada) – CGS D2-331643-2006

The Whitaker Foundation

#### Project Staff

Desmond C. Adler, Vivek J. Srinivasan, Shu-Wei Huang, Prof. James G. Fujimoto

### 1. Frequency-Swept Lasers and Fourier Domain Mode Locking (FDML)

Femtosecond lasers have found numerous applications as high performance light sources for biomedical imaging. Besides the use of their high pulse powers for non-linear imaging, their broad spectrum and short coherence length served as enabling tools for ultrahigh resolution optical coherence tomography (OCT - see the chapter dealing with Laser Medicine and Biomedical Imaging) [1-3]. Recently, efforts have been made to apply narrowband, rapidly frequency-tunable lasers for OCT imaging to achieve higher acquisition speeds and greater imaging sensitivity [4-13]. This concept is called “swept source / Fourier domain OCT,” or sometimes “optical frequency domain imaging (OFDI).” The measurement concept is similar to optical frequency domain reflectometry (OFDR), although the requirements for the laser are more demanding for OCT applications. The concept of swept source OCT imaging and the experimental imaging setup are described in the Laser Medicine and Biomedical Imaging chapter in detail. In this section, we will discuss progress in laser development for swept source OCT.

#### 1.1 Principles of Fourier Domain Mode Locking

Many different concepts and designs of narrowband tunable or swept laser sources have historically been investigated for numerous applications. None of these designs, however, could provide sufficient performance to meet the demands for swept source OCT. To be suitable for OCT imaging, the laser must operate within the “therapeutic window” where tissue absorption and scattering are low. For imaging epithelial tissues, a 1300 nm center wavelength is preferred for improved depth penetration. For ophthalmic imaging, a 1060 nm center wavelength is preferred to minimize losses from water absorption in the vitreous fluid. The imaging speed, axial resolution, and imaging depth of OCT systems are determined by the sweep rate, tuning range, and instantaneous linewidth of the laser, respectively. Therefore a tuning range of  $> 100$  nm, an instantaneous linewidth of  $< 0.1$  nm, and a sweep rate of 50,000 – 500,000 sweeps/sec (50 – 500 kHz) are simultaneously desired [11]. The resulting optical frequency sweep speeds are up to  $10^{19}$  Hz/s, and the required average output power is  $> 10$  mW.

Swept lasers incorporate a tunable intracavity wavelength-selective filter element in order to produce an output that varies in wavelength over time. In a conventional swept laser, the maximum sweep rate is usually limited by the time required for lasing to build up from the amplified stimulated emission (ASE) background of the gain medium. This time depends on the filter function, the ASE intensity, the saturation power, the laser gain, and the cavity roundtrip time. Sophisticated optical frequency shifting spectrometers, multi-detector balancing setups, or optoelectronic self referencing must be applied to reduce the problems with standard tunable lasers at higher sweep rates [9, 14]. Still, since imaging speeds of several hundred thousand axial

lines per second are required for three-dimensional OCT imaging (3D-OCT), conventional swept lasers cannot provide adequate performance for this application.

Fourier Domain Mode Locking (FDML) is a new swept laser technique that overcomes limitations in the maximum speed rate while simultaneously providing a broad tuning range, narrow instantaneous linewidth, and high output power. FDML lasers generate very low-noise frequency sweeps, equivalent to train of highly chirped laser pulses [15-18]. Figure 1 (left) shows a schematic representation of the FDML concept compared with a conventional swept laser. In the conventional laser, light from a broadband gain medium is spectrally filtered by a narrowband optical bandpass filter within the cavity and fed back to the gain medium. Only longitudinal modes with frequencies that are transmitted through the filter can lase at one point in time. When the passband of the filter is tuned during a sweep, lasing collapses and must build up from ASE at each new position of the filter. This significantly limits the performance and imposes a trade-off between sweep rate, instantaneous linewidth, tuning range, and output power [11].

In FDML lasers, as shown in Figure 1 (right), a dispersion managed delay line is incorporated into the cavity and the filter is tuned synchronously to the cavity round-trip time (or a harmonic of the round-trip time). This results in a quasi-stationary mode of operation. Light from one sweep propagates through the cavity and returns to the filter at the exact time when the transmission window of the filter is tuned to the position. Therefore, light from the previous round-trip is coupled back to the gain medium and lasing does not have to build up again from ASE. In other words, an entire frequency sweep is optically stored within the dispersion managed delay line in the laser cavity. Under ideal operation, sequential frequency sweeps have the same phase evolution and are mutually coherent.

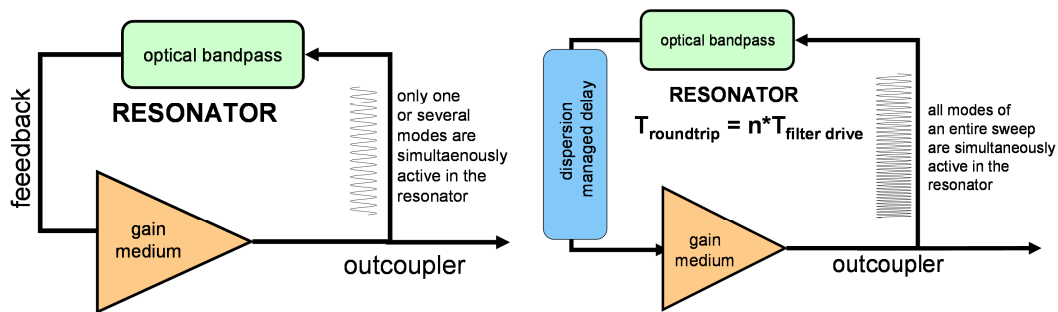


**Figure 1.** The concepts of conventional wavelength-swept lasers (left) and FDML lasers (right). In FDML, all modes are active within the cavity simultaneously, and quasi-stationary operation is achieved.

Figure 2 shows a schematic diagram of an FDML laser. The laser uses a fiber ring geometry with a semiconductor optical amplifier (SOA) as the gain medium and a fiber Fabry-Perot filter (FFP-TF) as the tunable, narrowband optical bandpass filter. Isolators (ISO) ensure that the laser operates in only one direction around the cavity. The FFP-TF is selected to have a free spectral range greater than the desired tuning range. The FFP-TF is driven with a sinusoidal waveform created by a high-precision digital function generator. The waveform is amplified by an electric power amplifier for driving the low-impedance capacitive load of the lead zirconate titanate (PZT) FFP-TF actuator. A fiber splitter acts as the output coupler, with the coupling ratio controlling the tradeoff between output power and tuning range. For OCT imaging, the laser output can be further amplified with a second SOA. The length of the dispersion-managed delay varies based on the desired sweep rate. For a 21 kHz drive frequency the delay should be 9.8 km, whereas for a 185 kHz drive frequency the delay should be only 1.1 km. Since the drive signal is sinusoidal, two wavelength sweeps are produced during each drive period as the FFP-TF is moved forward and backward. Therefore the effective sweep rate is twice the drive frequency.

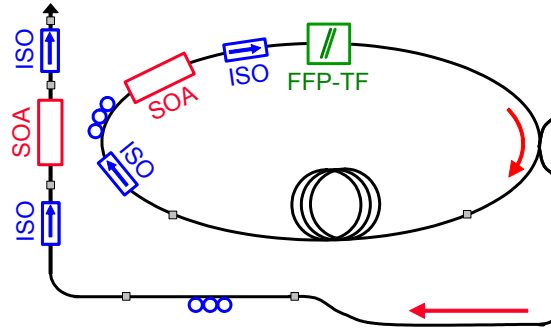


**Figure 2.** Schematic of an FDML laser. FFP-TF: fiber Fabry-Perot tunable filter.

## 2. Buffered FDML for Ultrahigh-Speed Operation

Despite the fact that both forward and backward sweep directions have approximately the same transient power characteristics in FDML lasers, as the effective sweep rate is increased beyond 300 kHz the two sweep directions begin to exhibit different noise characteristics. The “forward” sweep (short wavelengths to long wavelengths) typically exhibits poorer noise performance compared to the “backward” (long wavelengths to short wavelengths) sweep. Additionally, for OCT imaging applications it is desirable to produce unidirectional sweeps in order to reduce signal processing requirements. With bidirectional sweeping, for example, every second interference fringe must be reversed prior to Fourier transformation and image formation. Finally, it is not technically straightforward to achieve extremely high sweep rates ( $> 400$  kHz) simply by driving the FFP-TF at higher speeds due to the mechanical properties of the filter. An architecture called “buffered FDML” addresses these issues, enabling ultrahigh-speed sweeping and unidirectional operation.

Buffered FDML lasers use a cavity design that optically replicates the backward sweep and removes the undesired forward sweep by using a combination of time multiplexing and gain modulation. This concept is illustrated in Figure 3. In Figure 3 (left) the interference fringes produced by an asymmetric Michelson interferometer are shown, with the backward sweep circled in green and the forward sweep crossed out in red. The buffered FDML cavity is shown in Figure 3 (right). Two output couplers are placed at evenly-spaced locations within the cavity. Each output coupler extracts an optical copy of the propagating sweep, with the second coupler extracting a copy that is time-delayed by exactly one half of the cavity round-trip time. During the time normally occupied by the forward sweep, the intracavity SOA is modulated off. The two copies of the remaining backward sweep are combined outside of the cavity using a 50/50 fiber splitter and boosted by an external SOA. The result is a series of unidirectional, low-noise wavelength sweeps generated at twice the FFP-TF drive frequency, a record 370 kHz [16].

As previously mentioned, it is difficult to drive the FFP-TF at arbitrarily high frequencies due to a decrease in the mechanical response of the filter. Buffered FDML technology can be applied to multiply the effective sweep by adding additional output couplers and overdriving the FFP-TF near a mechanical resonance [19]. Near a mechanical resonant frequency, the FFP-TF undergoes a large physical translation for a relatively small amplitude drive signal. At these resonant points, the FFP-TF can be swept over a range larger than the desired total tuning range. This compresses the wavelength sweep into a smaller time window, allowing additional time-delayed copies to be extracted from the cavity. For every additional copy extracted, the effective sweep rate is further multiplied.

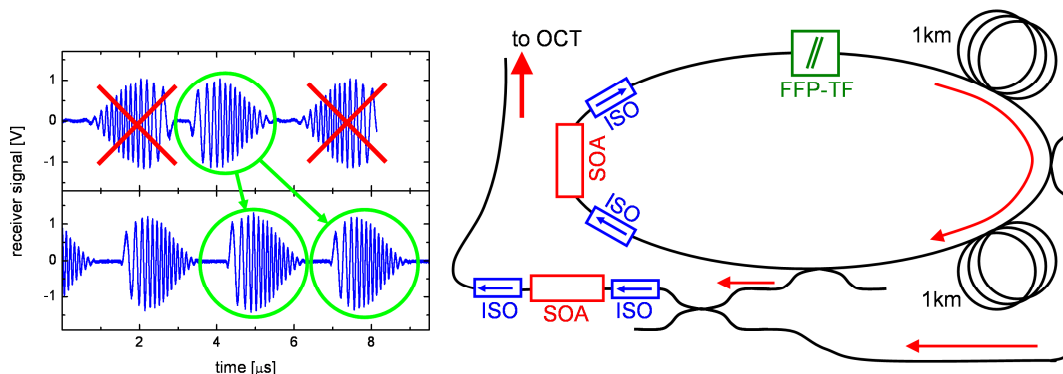


**Figure 3.** Buffered FDML lasers provide unidirectional sweeps at multiples of the cavity's fundamental frequency. Left: concept of buffered FDML with a two-tap cavity. The desired backward sweep is replicated, and the cavity SOA is turned off during the forward sweep. Right: Schematic of a buffered FDML cavity. SOA: semiconductor optical amplifier. ISO: optical isolator. FFP-TF: fiber Fabry-Perot tunable filter

The concept of higher-order buffering is shown in Figure 4. Two copies of the backward sweep are extracted from the cavity and then routed to a second external buffering stage. External buffering was recently demonstrated in an FDML laser operating at a center wavelength near 1050 nm for ophthalmic imaging [18]. In the external stage, four copies of the original sweep are created, time-shifted, and recombined in a final fiberoptic coupler. This arrangement quadruples the effective sweep rate compared to the FFP-TF drive frequency. The use of external buffering also minimizes power losses during recombination of the sweep copies. This concept can be extended by adding additional stages composed of a 50/50 splitter and fiber delay line to the external buffer. Each additional stage can further multiply the sweep rate without adding additional loss beyond the excess loss of the splitter and propagation loss of the fiber. To prevent temporal overlap of the sweep copies, the FFP-TF is driven with a high amplitude to reduce the amount of time required for each sweep. The duty cycle of the intracavity SOA is also correspondingly reduced. Double buffering has the added benefit of decreasing the portion of the sine wave used to generate the sweep, which improves the linearity of the frequency sweep.

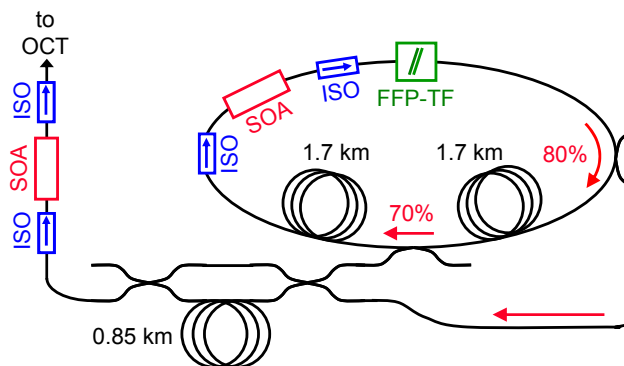


**Figure 4.** Double-buffered FDML laser, operating at a sweep rate of 240 kHz with a tuning range of 158 nm at a center wavelength of 1315 nm. Sweep rate is quadrupled by internal and external buffering stages. ISO, optical isolator. SOA, semiconductor optical amplifier. FFP-TF, fiber Fabry-Perot tunable filter.

The time-averaged output spectrum, measured using an optical spectrum analyzer, is shown in Figure 5(a). The total tuning range is 158 nm and the full width at half maximum

(FWHM) is 117 nm. The average output power is 62 mW with a duty cycle of 91%. OCT point spread functions (PSF's) measured at increasing ranging depths are shown in Figure 5(b). The sensitivity decreases by 5.5 dB at a ranging depth of 2 mm in air and by 23 dB at a ranging depth of 6 mm. This laser was used to study the detection of gold nanoparticle contrast agents using a novel photothermal modulation technique [19].

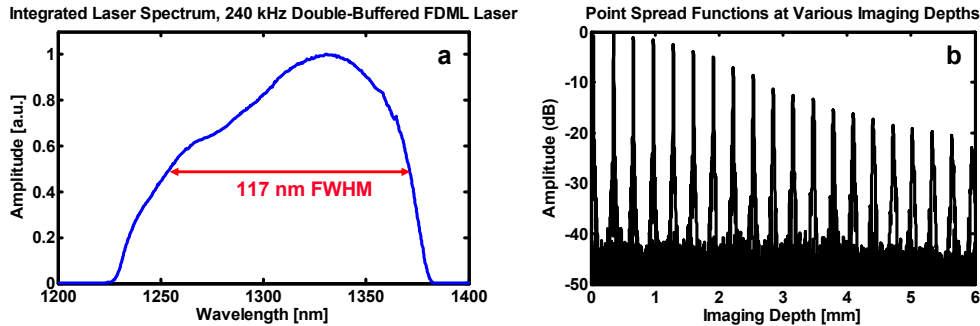


**Figure 5.** a, Integrated output spectrum for double-buffered FDML laser, with a tuning range of 158 nm and a full-width-half-maximum bandwidth of 117 nm. b, OCT point spread functions measured at increasing ranging depths.

### 3. FDML Operation with a Dispersive Cavity

FDML laser technology has achieved high power, wide bandwidth, and robust performance in ultrahigh speed 3D-OCT systems operating at 1310 nm [15, 20]. This wavelength range is well suited for imaging scattering tissues. However, to enable the use of FDML lasers for other high speed OCT applications such as ophthalmology, alternative wavelengths must be developed to avoid excessive loss water absorption. The 1060 nm wavelength range has recently emerged as an important wavelength for ophthalmic OCT imaging because it is in the transmission window for water with enhanced imaging depth in the choroid compared to 850 nm [21-23]. The 1060 nm range also has benefits for swept source OCM applications, since a smaller diffraction-limited spot can be achieved at shorter wavelengths and the transmission efficiency and performance of microscope objectives is better.

However, we currently have in operation a less matured fiber technology at 1060 nm compared to the telecommunication wavelengths at 1310 nm and 1550 nm. In particular, dispersion is a big issue for 1060 nm fibers since long lengths of fiber are used in FDML, and chromatic dispersion is more significant than better fabricated 1310 nm fibers. Another issue is the polarization effect of optical fiber. The wavelength dependent birefringence or chromatic birefringence arises from random imperfections and asymmetries in fiber. It cannot be compensated by adding retardation and will lead to modulations in the sweep spectrum. The polarization mode dispersion, which is a form of modal dispersion where two different polarizations of light in a waveguide travel at different speeds, may also affect the laser performance. It shall be noted that even for the more matured 1310 nm fiber technology, these dispersion effects still need to be taken into account, especially when long photon round trip delay is required and therefore the accumulated dispersion effects from kilometers of optical fiber cannot be ignored.

A typical FDML laser operating at 1060 nm has been developed in our group with a tuning range of 63 nm, supporting an axial resolution of 13.7  $\mu\text{m}$  in tissue [18]. This laser was demonstrated for 3D retinal imaging in human subjects at an axial line rate of 236 kHz and enables volumetric data to be acquired in only 1 to 2 seconds to improve the visualization of retinal features. The resolution axial resolution is, however, rather unsatisfactory compared to the 850 nm spectral / Fourier domain OCT, where 2-3  $\mu\text{m}$  resolution in tissue has been achieved [3, 24]. The limited system resolution can be attributed the imperfect dispersive fibers in the cavity, which present the

greatest hurdle for increasing FDML tuning ranges at 1060 nm central wavelength. Since cavity length is generally in the order of a few kilometers, dispersion produces a wavelength-dependent group delay in the fiber. The tunable filter sweep cannot be synchronized for all of the wavelengths in the cavity simultaneously. The timing mismatched portion of wavelengths, which is detuned from the synchronized wavelengths, results in a decrease in tuning bandwidth and increase in instantaneous line width. The axial resolution and the limited tuning bandwidth have to be improved for the optimum performance of swept source OCT technology using FDML laser.

To address these issues, our group has investigated novel methods to enhance laser performance using concepts similar to those demonstrated in short pulse fiber lasers. [25, 26] First, we have developed a “sigma ring” FDML cavity to compensate the chromatic birefringence and other polarization effects due to the long optical fiber. A circulator (CIRC) is used to form a linear portion and a ring portion of the cavity. The linear portion contains the fiber delay and a Faraday rotator mirror (FM). The Faraday mirror returns light in a polarization state orthogonal to its incident state so that birefringence variations are compensated for at every point in the branch, resulting in the cancellation of the polarization effects from the incoming trip of the light going through the same fiber. Secondly, we have plugged in an intracavity Mach-Zehnder component to form a dual cavity with two mismatched cavity lengths. This structure functions as a first order compensator for the light dispersion as the slower portion of the light will build laser oscillation through the longer cavity branch and the faster portion of the light will lase from the shorter cavity. Therefore, a larger bandwidth of light will be synchronically tuned with the same Fabry Perot driving frequency. This new laser design with a sigma ring cavity using the Faraday Mirror and circulator and the intracavity unbalanced Mach-Zehnder enables improved noise performance, stability, and image quality, as well as improved imaging speed and resolution.

Figure 6 A shows a schematic of the FDML laser used for this study. A fiber optic Fabry-Perot tunable filter (FFP-TF) with a linewidth of 0.08 nm is used to filter the light propagating in the cavity. A semiconductor optical amplifier is used as the gain element. 825 m of HI1060 fiber is used to set the cavity round trip time. The fiber is on a spool and the entire laser can be made compact. The filter is tuned at the round-trip frequency, which is approximately 124.5 kHz. As in our previous work [16], the SOA is turned off during the forward (short to long wavelength) sweep, and an extra-cavity unbalanced Mach-Zehnder is used to double the repetition rate. Using this novel laser scheme, we have achieved 8  $\mu\text{m}$  axial resolution, 91 dB sensitivity, with an eye illumination power of 1.2 mW. The 3dB FWHM bandwidth of the laser is about 68 nm, compared favorably to the 38 nm bandwidth in the standard FDML system [18] without polarization and dispersion management.

The axial resolution, although significantly enhanced from the earlier 13.7  $\mu\text{m}$ , still has room for improvement. The output power has been enough for retinal imaging while higher power is still needed to improve the sensitivity for tissue imaging such as in OCM applications. There are other methods which may further reduce the dispersion and improve the resolution. We will further investigate the use of dispersion compensating specialty fibers to cancel the normal fiber dispersion in the cavity. Higher-order mode fiber is a possible candidate since it can be fabricated in kilometer-scale lengths and has low loss. [27] Alternately, time and frequency division multiplexing can be used to selectively synchronize different wavelength regimes. The sweep can be split into a series of sub-bands using wavelength division multiplexing (WDM) couplers, or by placing SOAs with different gain center bandwidths in each parallel path. Dispersion can be compensated in a piecewise manner by setting the differential length of each path to correspond to the difference in roundtrip time of the wavelength sub-band.

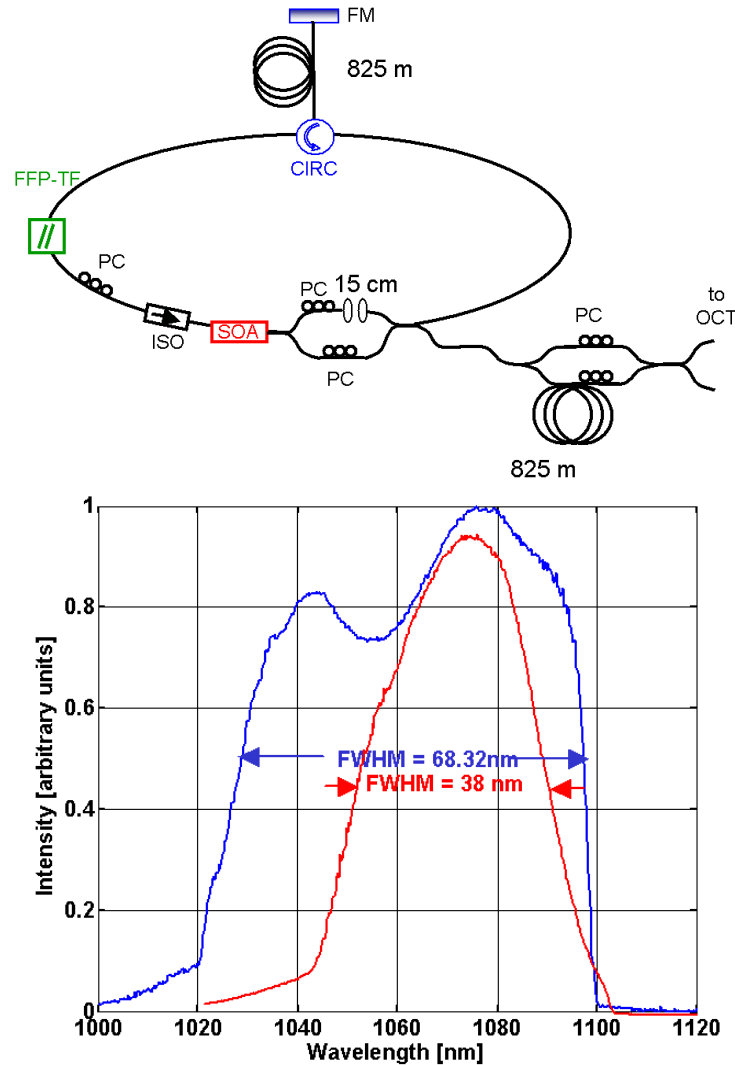


**Figure 6:** Upper: schematic for a 1070 nm “sigma ring” FDML laser with unbalanced intracavity Mach-Zehnder component for dispersion compensation. The laser also has an external buffering Mach-Zehnder stage to multiply the sweep rate to 249 kHz. Lower: average integrated output spectrum. Blue is spectrum from this dispersion compensated laser scheme where a 68 nm bandwidth and 8  $\mu\text{m}$  imaging resolution in the eye has been obtained. The red curve is from a regular FDML cavity without dispersion compensation. It has 38 nm bandwidth and a resolution of 13.7  $\mu\text{m}$  in the eye.

#### 4. Enhanced Phase Stability in FDML Lasers

FDML lasers have been demonstrated to provide an exceptional combination of sweep rate, tuning range, output power, and narrow instantaneous linewidth. This makes them excellent sources for high-speed OCT imaging, where the amplitude and frequency of interference fringes generated by a Michelson interferometer can be used to generate 3D maps of a sample’s microstructural architecture. With a laser that is highly phase-stable, however, it is possible to analyze the phase of the OCT interference fringes in order to detect picometer-scale surface displacements [28]. This technique is often referred to as OCT phase microscopy, or more generally, phase sensitive OCT. Phase-based techniques provide a complementary contrast mechanism to standard OCT analysis. Recently, our group has demonstrated that the quasi-stationary operating regime of FDML lasers makes them very well suited for phase-sensitive OCT imaging [17]. FDML lasers can detect surface features as small as 39 pm, comparable to the best

OCT phase microscopes previously demonstrated, but at speeds up to an order of magnitude faster. FDML lasers and phase-sensitive OCT imaging can also be used to detect small optical path changes associated with heating and cooling. This technique was recently applied to detect nanoparticle contrast agents using photothermal modulation [19].

FDML lasers operate in a quasi-stationary regime where each wavelength in the sweep has many characteristics of a narrowband continuous-wave laser. Our group demonstrated that FDML lasers achieve very high levels of phase stability by measuring the phase noise of a series of conventional swept lasers, standard FDML lasers, and buffered FDML lasers. A common path Michelson interferometer, where the front surface of a thin glass cover slip provides the reference reflection for the interferometer instead of a separate reference arm, was used for these measurements. A common path setup is advantageous for phase-based measurements since it eliminates phase noise arising from the different paths traveled by the sample and reference light in a typical Michelson interferometer. A sample, such as a biological tissue or photonic device, can be placed on the back surface of the coverslip.

The sensitivity of the system to surface displacement (displacement sensitivity) was measured by recording the phase at the back surface of a 210  $\mu\text{m}$  cover slip relative to the front surface. Phase information was obtained by Fourier transforming the interference fringes, isolating the back surface reflection, and finding the angle of its complex-valued peak. Buffered FDML lasers with sweep rates of 42, 117, and 370 kHz were constructed by varying the fiber length within the laser cavity. A non-buffered FDML laser operating at 42 kHz and a conventional swept laser [11] operating at 2 kHz were also tested. All lasers had a similar tuning range ( $\sim 110$  nm) and average output power ( $\sim 11$  mW) at a center wavelength of 1285 nm. The same FFP-TF and semiconductor optical amplifiers were used in all of the lasers. Optical path displacement  $\Delta z$  can be calculated from the measured phase  $\Delta\phi$  using the relationship  $\Delta z = \lambda_0 \Delta\phi / 4\pi n$ , where  $\lambda_0$  is the center wavelength and  $n$  is the sample refractive index [29]. The standard deviation of  $\Delta z$  over several hundred measurements gives the system displacement sensitivity. Differential displacement sensitivities and signal-to-noise ratio limits to displacement sensitivity were also calculated.

Table 1 summarizes the displacement sensitivity measurements for a conventional swept laser operating at 2 kHz (2,000 sweeps per second) and buffered FDML lasers operating at 42, 117, and 370 kHz. The buffered FDML lasers provide 2.2 – 5.8x better displacement sensitivity while operating at speeds that are 31 – 185x faster. All FDML lasers provide improved displacement sensitivities (DS in Table 1) compared to the conventional swept laser, even though the FDML sources operate at much higher sweep speeds. Comparing the non-buffered FDML laser at 42 kHz to the buffered FDML laser at 42 kHz, buffered FDML provides an additional 1.8x improvement in displacement sensitivity. This is because the buffered FDML laser produces alternating sweeps, in groups of two, that are virtual optical copies of each other. Since no filtering or amplification occurs between the two output couplers, the sweeps have increased phase correlation compared to non-buffered FDML lasers. As the sweep rates of the buffered FDML lasers are increased, displacement sensitivity degrades moderately from 39 pm at 42 kHz to 102 pm at 370 kHz. This compares favorably with previously reported displacement sensitivities of 25 pm at 29 kHz for spectrometer-based systems [30] and 475 pm at 16 kHz for conventional swept lasers [31]. For surface profilometry applications, where displacements of a single surface are measured, a buffered FDML laser could measure a continuous range between the displacement sensitivity (39 – 102 pm) and the laser coherence length ( $> 4$  mm), over  $\sim 8$  orders of magnitude.

Table 1, column 3 shows the SNR-limited displacement sensitivities calculated for each laser. Buffered FDML lasers come within 1.4 – 2.0x of the SNR limit, compared with 25x for the conventional swept source. Table 1, column 4 shows the measured differential displacement sensitivity for each laser. This shows the minimum displacement that can be measured between two consecutive axial scans by subtracting their phases. The performance of the conventional

swept laser and non-buffered FDML laser degrade by a factor of  $\sim\sqrt{2}$  compared to their respective single-measurement displacement sensitivity values. This is expected since the phase noise of these lasers is mainly additive white noise. For the buffered FDML lasers, however, the differential and single-measurement values are very similar. This enhancement is also the result of the multiple optical copies of the wavelength sweeps produced by buffered FDML lasers, and could significantly improve Doppler OCT measurements in the future.

Laser Type	DS [ $\mu\text{m}$ ]	SNR Limit [ $\mu\text{m}$ ]	DDS [ $\mu\text{m}$ ]
Conventional swept laser @ 2 kHz	226	9	361
FDML @ 42 kHz	71	26	115
Buffered FDML @ 42 kHz	39	22	43
Buffered FDML @ 117 kHz	52	38	56
Buffered FDML @ 370 kHz	102	50	119

**Table 1.** Displacement sensitivity (DS), signal-to-noise ratio (SNR) limited displacement sensitivity, and differential displacement sensitivity (DDS) for a conventional swept laser, a non-buffered FDML laser, and three different buffered FDML lasers. Buffered FDML lasers provide displacement sensitivities that are comparable to spectrometer-based OCT systems, but at speeds 1.5 – 12x higher.

The buffered FDML laser operating at 117 kHz was used to demonstrate high-sensitivity high-speed OCT phase microscopy for two different applications: the detection of nanometer-scale time-varying surface waves; and the detection of nanometer-scale spatially-varying surface features. For the first application, a gold mirror was mounted to a PZT transducer. The phase was measured at one point on the mirror as the PZT was actuated over  $\pm 3$  nm at a rate of 5 kHz. As shown in Figure 7 (left), the FDML laser and phase-sensitive OCT detection system were capable of clearly resolving this small, rapid surface motion. The slowly varying offset in the measured position is motion of the mirror mount relative to the reference surface.

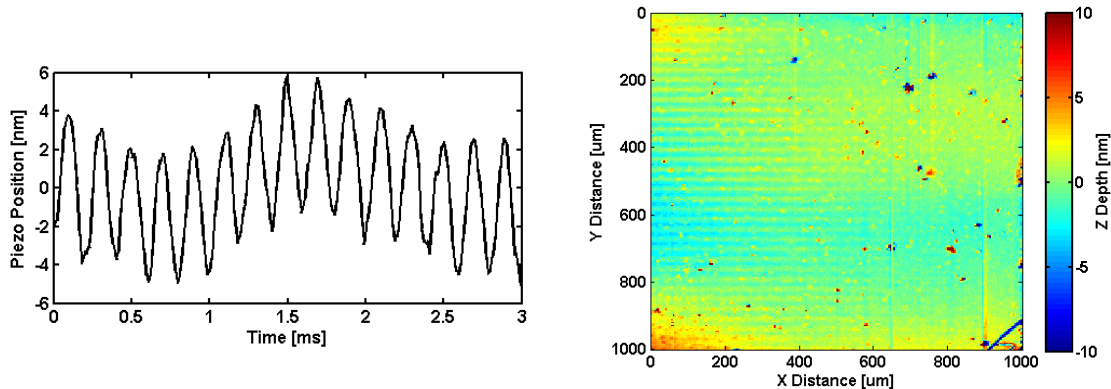


**Figure 7.** Left: mirror displacement measured using phase-sensitive OCT and a buffered FDML laser operating at 117 kHz. The mirror is actuated over  $\pm 3$  nm at 5 kHz. Right: 3D OCT phase microscopy image of a glass coverslip obtained using the same laser. Nanometer-scale grooves and pits are visible in the surface.

For the second application, a glass coverslip was placed in the sample arm. The phase of the back surface relative to the front surface was measured at each point in a  $1000 \times 1000 \mu\text{m}$  square region and displayed as an optical path difference in a false color image. The results of this 3D OCT phase microscopy experiment are shown in Figure 15 (right). Exceptionally low phase noise is evident in the resulting image. Nanometer-scale surface defects and grooves are

visible in this sample that is nominally “flat”, and nonlinear variations in sample thickness ( $\pm 2$  nm) or refractive index ( $\pm 1.4 \times 10^{-5}$ ) can be visualized. The 3D dataset consists of  $230 \times 230$  axial scans and was acquired in only 0.45 s. This demonstrates that buffered FDML lasers can perform 3D OCT phase microscopy with nanometer sensitivities at speeds significantly higher than other technologies.

In general, buffered FDML technology provides an exceptional combination of high phase stability and high sweep rates. This makes FDML lasers a good choice for phase-sensitive measurements, including OCT phase microscopy, Doppler flow imaging, and phase-based surface profilometry. Future improvements and new buffering concepts may further improve the displacement sensitivity and sweep rate, increasing the phase dynamic range and opening new areas of investigation.

## References

1. D. Huang, E. A. Swanson, C. P. Lin, J. S. Schuman, W. G. Stinson, W. Chang, M. R. Hee, T. Flotte, K. Gregory, C. A. Puliafito, and J. G. Fujimoto, "Optical Coherence Tomography," *Science* **254**, 1178-1181 (1991).
2. W. Drexler, U. Morgner, F. X. Kartner, C. Pitris, S. A. Boppart, X. D. Li, E. P. Ippen, and J. G. Fujimoto, "In vivo ultrahigh-resolution optical coherence tomography," *Optics Letters* **24**, 1221-1223 (1999).
3. W. Drexler, U. Morgner, R. K. Ghanta, F. X. Kärtner, J. S. Schuman, and J. G. Fujimoto, "Ultrahigh-resolution ophthalmic optical coherence tomography," *Nature Medicine* **7**, 502-507 (2001).
4. A. F. Fercher, C. K. Hitzenberger, G. Kamp, and S. Y. Elzaiat, "Measurement of Intraocular Distances by Backscattering Spectral Interferometry," *Opt Commun* **117**, 43-48 (1995).
5. F. Lexer, C. K. Hitzenberger, A. F. Fercher, and M. Kulhavy, "Wavelength-tuning interferometry of intraocular distances," *Appl Optics* **36**, 6548-6553 (1997).
6. B. Golubovic, B. E. Bouma, G. J. Tearney, and J. G. Fujimoto, "Optical frequency-domain reflectometry using rapid wavelength tuning of a Cr<sup>4+</sup>:forsterite laser," *Optics Letters* **22**, 1704-1706 (1997).
7. S. R. Chinn, E. A. Swanson, and J. G. Fujimoto, "Optical coherence tomography using a frequency-tunable optical source," *Optics Letters* **22**, 340-342 (1997).
8. S. H. Yun, G. J. Tearney, J. F. de Boer, N. Iftimia, and B. E. Bouma, "High-speed optical frequency-domain imaging," *Optics Express* **11**, 2953-2963 (2003).
9. M. A. Choma, M. V. Sarunic, C. H. Yang, and J. A. Izatt, "Sensitivity advantage of swept source and Fourier domain optical coherence tomography," *Optics Express* **11**, 2183-2189 (2003).
10. M. A. Choma, K. Hsu, and J. A. Izatt, "Swept source optical coherence tomography using an all-fiber 1300-nm ring laser source," *Journal of biomedical optics* **10**, no. 044009 (2005).
11. R. Huber, M. Wojtkowski, K. Taira, J. G. Fujimoto, and K. Hsu, "Amplified, frequency swept lasers for frequency domain reflectometry and OCT imaging: design and scaling principles," *Optics Express* **13**, 3513-3528 (2005).
12. J. Zhang, and Z. P. Chen, "In vivo blood flow imaging by a swept laser source based Fourier domain optical Doppler tomography," *Optics Express* **13**, 7449-7457 (2005).
13. Y. Yasuno, V. D. Madjarova, S. Makita, M. Akiba, A. Morosawa, C. Chong, T. Sakai, K. P. Chan, M. Itoh, and T. Yatagai, "Three-dimensional and high-speed swept-source optical coherence tomography for in vivo investigation of human anterior eye segments," *Optics Express* **13**, 10652-10664 (2005).
14. J. T. Oh, and B. M. Kim, "Artifact removal in complex frequency domain optical coherence tomography with an iterative least-squares phase-shifting algorithm," *Appl Optics* **45**, 4157-4164 (2006).
15. R. Huber, M. Wojtkowski, and J. G. Fujimoto, "Fourier Domain Mode Locking (FDML): A new laser operating regime and applications for optical coherence tomography," *Optics Express* **14**, 3225-3237 (2006).

16. R. Huber, D. C. Adler, and J. G. Fujimoto, "Buffered Fourier domain mode locking: unidirectional swept laser sources for optical coherence tomography imaging at 370,000 lines/s," *Optics Letters* **31**, 2975-2977 (2006).
17. D. C. Adler, R. Huber, and J. G. Fujimoto, "Phase-sensitive optical coherence tomography at up to 370,000 lines per second using buffered Fourier domain mode-locked lasers," *Optics Letters* **32**, 626-628 (2007).
18. R. Huber, D. C. Adler, V. J. Srinivasan, and J. G. Fujimoto, "Fourier domain mode locking at 1050 nm for ultra-high-speed optical coherence tomography of the human retina at 236,000 axial scans per second," *Optics Letters* **32**, 2049-2051 (2007).
19. D. C. Adler, S. W. Huang, R. Huber, and J. G. Fujimoto, "Photothermal detection of gold nanoparticles using phase-sensitive optical coherence tomography," *Optics Express* **16**, 4376-4393 (2008).
20. D. C. Adler, Y. Chen, R. Huber, J. Schmitt, J. Connolly, and J. G. Fujimoto, "Three-dimensional endomicroscopy using optical coherence tomography," *Nature Photonics* **1**, 709-716 (2007).
21. S. Bourquin, A. D. Aguirre, I. Hartl, P. Hsiung, T. H. Ko, J. G. Fujimoto, T. A. Birks, W. J. Wadsworth, U. Bunting, and D. Kopf, "Ultrahigh resolution real time OCT imaging using a compact femtosecond Nd : Glass laser and nonlinear fiber," *Optics Express* **11**, 3290-3297 (2003).
22. B. Povazay, K. Bizheva, B. Hermann, A. Unterhuber, H. Sattmann, A. F. Fercher, W. Drexler, C. Schubert, P. K. Ahnelt, M. Mei, R. Holzwarth, W. J. Wadsworth, J. C. Knight, and P. S. Russel, "Enhanced visualization of choroidal vessels using ultrahigh resolution ophthalmic OCT at 1050 nm," *Optics Express* **11**, 1980-1986 (2003).
23. A. Unterhuber, B. Povazay, B. Hermann, H. Sattmann, A. Chavez-Pirson, and W. Drexler, "In vivo retinal optical coherence tomography at 1040 nm-enhanced penetration into the choroid," *Optics Express* **13**, 3252-3258 (2005).
24. V. J. Srinivasan, B. K. Monson, M. Wojtkowski, R. A. Bilonick, I. Gorczynska, R. Chen, J. S. Duker, J. S. Schuman, and J. G. Fujimoto, "Characterization of outer retinal morphology with high-speed, ultrahigh-resolution optical coherence tomography," *Investigative ophthalmology & visual science* **49**, 1571-1579 (2008).
25. T. F. Carruthers, and I. N. Duling, "10-GHz, 1.3-ps erbium fiber laser employing soliton pulse shortening," *Optics Letters* **21**, 1927-1929 (1996).
26. J. W. Lou, T. F. Carruthers, and M. Currie, "Mode-locked multiple-wavelength erbium-doped fiber laser in a sigma configuration," *IEEE Photonics Technology Letters* **14**, 281-283 (2002).
27. S. Ramachandran, S. Ghalmi, J. W. Nicholson, M. F. Yan, P. Wisk, E. Monberg, and F. V. Dimarcello, "Anomalous dispersion in a solid, silica-based fiber," *Optics Letters* **31**, 2532-2534 (2006).
28. M. Sticker, M. Pircher, E. Gotzinger, H. Sattmann, A. F. Fercher, and C. K. Hitzenberger, "En face imaging of single cell layers by differential phase-contrast optical coherence microscopy," *Optics Letters* **27**, 1126-1128 (2002).
29. M. A. Choma, A. K. Ellerbee, S. Yazdanfar, and J. A. Izatt, "Doppler flow imaging of cytoplasmic streaming using spectral domain phase microscopy," *Journal of biomedical optics* **11**, - (2006).
30. C. Joo, T. Akkin, B. Cense, B. H. Park, and J. E. de Boer, "Spectral-domain optical coherence phase microscopy for quantitative phase-contrast imaging," *Optics Letters* **30**, 2131-2133 (2005).
31. B. J. Vakoc, S. H. Yun, J. F. de Boer, G. J. Tearney, and B. E. Bouma, "Phase-resolved optical frequency domain imaging," *Optics Express* **13**, 5483-5493 (2005).

## Publication

### Journal Articles, submitted for publication

V. J. Srinivasan, D. C. Adler, Y. Chen, I. Gorczynska, R. Huber, J. S. Duker, J. S. Schuman, and J. G. Fujimoto, "Ultra-high-speed Optical Coherence Tomography for Three-Dimensional and En Face Imaging of the Retina and Optic Nerve Head," submitted to *Invest. Ophthalmol. Vision Science*, 2008.

### Journal Articles

1. J. Kim, F. Ludwig, M. Felber, and F. X. Kärtner, "Long-term stable microwave signal extraction from mode-locked lasers," *Opt. Express*, 15(14): 8951-8959 (2007).
2. J. Kim, J. Chen, J. Cox, and F. X. Kärtner, "Attosecond-resolution timing jitter characterization of free-running mode-locked lasers," *Opt. Lett.* 32(24): 3519-3521 (2007).
3. A. Sennaroglu, F. X. Kärtner, and J. G. Fujimoto, "Low-threshold, room-temperature femtosecond Cr<sup>4+</sup>:forsterite laser," *Opt. Express*, 15(20): 13043-13048 (2007).
4. D.C. Adler, J. Stenger, I. Gorczynska, H. Lie, T. Hensick, R. Spronk, S. Wolohojian, N. Khandekar, J.Y. Jiang, S. Barry, A.E. Cable, R. Huber, and J.G. Fujimoto, "Comparison of three-dimensional optical coherence tomography and high resolution photography for art conservation studies," *Opt. Exp.* 15, 15972-15986, November (2007).
5. D.C. Adler, Y. Chen, R. Huber, J. Schmitt, J. Connolly, and J.G. Fujimoto, "Three-dimensional endoscopy using optical coherence tomography," *Nat. Photon.* 1, 709-716, December (2007).
6. U. Demirbas, A. Sennaroglu, A. Benedick, A. Siddiqui, F. X. Kärtner, and J. G. Fujimoto, "Diode-pumped, high-average power femtosecond Cr<sup>3+</sup>:LiCAF laser," *Optics Letters*, Vol. 32 Issue 22, pp.3309-3311 (2007).
7. M. W. Geis, S. J. Spector, M. E. Grein, R. T. Schulein, J. U. Yoon, D. M. Lennon, C. M. Wynn, S. T. Palmacci, F. Gan, F. X. Kärtner, and T. M. Lyszczarz, "CMOS-Compatible All-Si High-Speed Waveguide Photodiodes With High Responsivity in Near-Infrared Communication Band," *IEEE Photonics Technology Letters* 19:(3) pp.152-154 (2007).
8. M. W. Geis, S. J. Spector, M. E. Grein, R. T. Schulein, J. U. Yoon, D. M. Lennon, S. Denneault, F. Gan, F. X. Kärtner, and T. M. Lyszczarz, "All Silicon Infrared Photodiodes, Photo Response and Processing Temperature," *Opt. Express* 15:(25) pp. 16886-16894 (2007).
9. A. Gordon, Ch. Y. Wang, L. Diehl, F. X. Kärtner, A. Belyanin, D. Bour, S. Corzine, G. Höfler, H. C. Liu, H. Schneider, T. Maier, M. Troccoli, J. Faist, and Federico Capasso, "Multimode regimes in quantum cascade lasers: from coherent instabilities to spatial hole burning," *Physical Rev. A.* 75, 031802 (2007).
10. R. Huber, D.C. Adler, V.J. Srinivasan, I. Gorczynska, and J.G. Fujimoto, "Fourier domain mode locking at 1050 nm for ultra-high-speed optical coherence tomography of the human retina at 236,000 axial scans per second," *Optics Letters* vol. 32, pp. 2049-2051, July (2007).
11. J. Kim, J. Chen, J. Cox, and F. X. Kärtner, "Attosecond-resolution timing jitter characterization of free-running mode-locked lasers," *Opt. Lett.* 32(24): 3519-3521 (2007).
12. J. Kim, F. Ludwig, M. Felber, and F. X. Kärtner, "Long-term stable microwave signal extraction from mode-locked lasers," *Opt. Express*, 15(14): 8951-8959 (2007).
13. L.A. Kranendonk, X. An, A. Caswell, R.E. Herold, S.T. Sanders, R. Huber, J.G. Fujimoto, Y. Okura, and Y. Urata, "High speed engine gas thermometry by Fourier-domain mode-locked laser absorption spectroscopy," *Opt. Exp.* 15, 15115-15128, October (2007).

14. P.T. Rakich, M.A. Popović, M. Soljačić and E.P. Ippen, "Trapping, corralling and spectral bonding of optical resonances through optically induced potentials," *Nature Photonics* 1, 658-665 (2007).
15. A. Sennaroglu, F. X. Kärtner, and J. G. Fujimoto, "Low-threshold, room-temperature femtosecond Cr<sup>4+</sup>:forsterite laser," *Opt. Express*, 15(20): 13043-13048 (2007).
16. Tymon Barwicz, Michael A. Watts, Milos A. Popovic, Peter T. Rakich, Luciano Socci, Franz X. Kaertner, Erich P. Ippen and Henry I. Smith, "Polarization-Transparent Microphotonic Devices in the Strong Confinement Limit," *Nature Photonics*, 1, 57-60, 2007
17. T. Barwicz, H. Byun, F. Gan, C. W. Holzwarth, M. A. Popovic, P. T. Rakich, M. R. Watts, E. P. Ippen, F. X. Kärtner, H. I. Smith, J. S. Orcutt, R. J. Ram, V. Stojanovic, O. O. Olubuyide, J. L. Hoyt, S. Spector, M. Geis, M. Grein, T. Lyszczarz, J. U. Yoon, "Silicon Photonics for Compact, Energy-Efficient Interconnects," *J. Opt. Networking*, 6, 63-73, 2007
18. Jian Chen, Jason W. Sickler, Erich P. Ippen and Franz X. Kärtner, "High Repetition Rate, Low Jitter, Low Intensity Noise, Fundamentally Mode-locked 167 fs Soliton Er-fiber Laser," *Opt. Lett.* 32, 1566-1568, 2007
19. D.C. Adler, S.-W. Huang, R. Huber, and J.G. Fujimoto, "Photothermal detection of gold nanoparticles using phase-sensitive optical coherence tomography," *Opt. Exp.* 16, 4376-4393, March 17, (2008).
20. T. Barwicz, C.W. Holzwarth, P.T. Rakich, M.A. Popović, E.P. Ippen and Henry I. Smith, "Optical loss in silicon microphotonic waveguides induced by metallic contamination," *Appl. Phys. Lett.* 92, 131108 (2008).
21. J. Chen, J. Sickler, E.P. Ippen, and F.X. Kaertner, "Generation of low-timing-jitter femtosecond pulse trains with 2 GHz repetition rate via external repetition rate multiplication," *Optics Letters*, 33 (9): 959-961 (2008)
22. H. M. Crespo, J. R. Birge, E. L. Falcão-Filho, M. Y. Sander, A. J. Benedick, and F. X. Kärtner, "Nonintrusive phase stabilization of sub-two-cycle pulses from a prismless octave-spanning Ti:sapphire laser," *Opt. Lett.* 33(8): 833-835 (2008).
23. U. Demirbas, A. Sennaroglu, A. Benedick, A. Siddiqui, F. X. Kärtner, and J. G. Fujimoto, "Highly efficient, low-cost femtosecond Cr<sup>3+</sup>:LiCAF laser pumped by single-mode diodes," *Opt. Lett.* 33:(6), pp.590-592 (2008).
24. C. H. Li, A. J. Benedick, P. R. Fendel, A. G. Glenday, F. X. Kaertner, D. F. Phillips, D. Sasselov, A. Szentgyorgyi and R. L. Walsworth, "A laser frequency comb that enables radial velocity measurements with a precision of 1cm s<sup>-1</sup>," *Nature* 452(7187): 610-612 (2008).
25. O. Nohadani, J. R. Birge, F. X. Kärtner, and D. J. Bertsimas, "Robust chirped mirrors," *Appl. Opt.* 47(14): 2630-2636 (2008).
26. J. R. Birge and F. X. Kärtner, "Analysis and mitigation of systematic errors in spectral shearing interferometry of pulses approaching the single-cycle limit," *J. Opt. Soc. Am. B* 25(6): A111-A119 (2008). Invited Paper.
27. H. M. Crespo, J. R. Birge, E. L. Falcão-Filho, M. Y. Sander, A. J. Benedick, and F. X. Kärtner, "Nonintrusive phase stabilization of sub-two-cycle pulses from a prismless octave-spanning Ti:sapphire laser," *Opt. Lett.* 33(8): 833-835 (2008).
28. C. H. Li, A. J. Benedick, P. R. Fendel, A. G. Glenday, F. X. Kaertner, D. F. Phillips, D. Sasselov, A. Szentgyorgyi and R. L. Walsworth, "A laser frequency comb that enables radial velocity measurements with a precision of 1cm s<sup>-1</sup>," *Nature* 452(7187): 610-612 (2008).
29. S. Rausch, Th. Binhammer, A. Harth, N. Meiser, R. Ell, F. X. Kärtner, and U. Morgner, "Controlled Waveforms on the Single-cycle Scale from a Femtosecond Oscillator," Vol. 16 Issue 13, pp.9739-9745 (2008).

30. G.-R. Zhou, M. W. Geis, S. J. Spector, F. Gan, M. E. Grein, R. T. Schulein, J. S. Orcutt, J. U. Yoon, D. M. Lennon, E. P. Ippen, Th. M. Lyszczarz and F. X. Kärtner, "Effect of Carrier Lifetime on Forward-biased Silicon Mach-Zehnder Modulators," *Opt. Express* 16:(8), 5218-5226 (2008).
31. Paul W. Juodawlkis, Jason J. Plant, Joseph P. Donnelly, Ali Motamedi, and Erich P. Ippen, "Continuous-wave two-photon absorption in a Watt-class semiconductor optical amplifier," *Opt. Exp.* 16, 12387-96, 2008
32. Rafif E. Hamam, Mihai Ibanescu, Evan J. Reed, Peter Bermel, Steven G. Johnson, Erich Ippen, J. D. Joannopoulos and Marin Soljacic "Purcell effect in nonlinear photonic structures: A coupled mode theory analysis," *Opt. Exp.*, 16, 12523-37, 2008
33. J. Chen, J. Sickler, E.P.Ippen, and F.X. Kaertner, "Generation of low-timing-jitter femtosecond pulse trains with 2 GHz repetition rate via external repetition rate multiplication," *Optics Letters*, 33 (9): 959-961 (2008)
34. S.J. Spector, M.W. Geis, G.-R. Zhou, M.E. Grein, R.T. Schulein, F. Gan, M.A. Popović, J.U. Yoon, D.M. Lennon, E.P. Ippen, F.X. Kärtner and T.M. Lyszczarz, "CMOS-Compatible Dual-Output Wideband Silicon Modulator for Analog Signal Processing," *Optics Express*,16(15): 11027-11031 (2008).
35. T. Barwicz, C.W. Holzwarth, P.T. Rakich, M.A. Popović, E.P. Ippen and Henry I. Smith, "Optical loss in silicon microphotonic waveguides induced by metallic contamination," *Appl. Phys. Lett.* 92, 131108 (2008).
36. P.T. Rakich, M.A. Popović, M. Soljačić and E.P. Ippen, "Trapping, corraling and spectral bonding of optical resonances through optically induced potentials," *Nature Photonics* 1, 658-665 (2007).
37. A. Gordon, Ch. Y. Wang, L. Diehl, F. X. Kärtner, A. Belyanin, D. Bour, S. Corzine, G. Höfler, H. C. Liu, H. Schneider, T. Maier, M. Troccoli, J. Faist, and Federico Capasso, "Multimode regimes in quantum cascade lasers: from coherent instabilities to spatial hole burning," *Physical Rev. A.* **75**, 031802 (2007).
38. M. W. Geis, S. J. Spector, M. E. Grein, R. T. Schulein, J. U. Yoon, D. M. Lennon, C. M. Wynn, S. T. Palmacci, F. Gan, F. X. Kärtner, and T. M. Lyszczarz, "CMOS-Compatible All-Si High-Speed Waveguide Photodiodes With High Responsivity in Near-Infrared Communication Band," *IEEE Photonics Technology Letters* 19:(3) pp.152-154 ( 2007).
39. M. W. Geis, S. J. Spector, M. E. Grein, R. T. Schulein, J. U. Yoon, D. M. Lennon, S. Denneault, F. Gan, F. X. Kärtner, and T. M. Lyszczarz, "All Silicon Infrared Photodiodes, Photo Response and Processing Temperature," *Opt. Express* 15:(25) pp. 16886-16894 (2007).
40. U. Demirbas, A. Sennaroglu, A. Benedick, A. Siddiqui, F. X. Kärtner, and J. G. Fujimoto, "Diode-pumped, high-average power femtosecond Cr<sup>3+</sup>:LiCAF laser," *Optics Letters*, Vol. 32 Issue 22, pp.3309-3311 (2007).
41. G.-R. Zhou, M. W. Geis, S. J. Spector, F. Gan, M. E. Grein, R. T. Schulein, J. S. Orcutt, J. U. Yoon, D. M. Lennon, E. P. Ippen, Th. M. Lyszczarz and F. X. Kärtner, "Effect of Carrier Lifetime on Forward-biased Silicon Mach-Zehnder Modulators," *Opt. Express* 16:(8), 5218-5226 (2008).
42. U. Demirbas, A. Sennaroglu, A. Benedick, A. Siddiqui, F. X. Kärtner, and J. G. Fujimoto, "Highly efficient, low-cost femtosecond Cr<sup>3+</sup>:LiCAF laser pumped by single-mode diodes," *Opt. Lett.* 33:(6), pp.590-592 (2008).
43. S. Rausch, Th. Binhammer, A. Harth, N. Meiser, R. Ell, F. X. Kärtner, and U. Morgner, "Controlled Waveforms on the Single-cycle Scale from a Femtosecond Oscillator," Vol. 16 Issue 13, pp.9739-9745 (2008).

44. J. Kim, J. A. Cox, J. J. Chen, and F. X. Kärtner, "Drift-free femtosecond timing synchronization of optical and microwave sources over long distances with 10<sup>-19</sup> stability," submitted to Nature Photonics.
45. C. E. Cramer, C-H. Li, A. Benedick, A. G. Glenday, D. Phillips, D. Sasselov, A. Szentgyorgyi, F. X. Kärtner and R. Walsworth, "Astro-Comb: Revolutionizing precision spectroscopy in astrophysics," J. Mod. Opt. submitted.
46. J. Kim, J. A. Cox, J. J. Chen, and F. X. Kärtner, "Overcoming timing jitter constraints in analogue-to-digital conversion using optical pulse trains," submitted to Nature Photonics.
47. K. H. Hong, A. Siddiqui, J. Moses, J. Gopinath, J. Hybl, F. O. Ilday, T.Y. Fan and F. X. Kaertner, "Generation of 287-W, 5.5-ps pulses at 78-MHz repetition rate from a cryogenically-cooled Yb:YAG amplifier seeded by a fiber chirped-pulse amplification system," to appear in Optics Letters.
48. H. Byun, D. Pudo, J. Chen, E. P. Ippen and F. X. Kärtner, "High repetition rate, 491 MHz, femtosecond fiber laser with low timing jitter," to appear in Optics Letters
49. U. Demirbas, A. Sennaroglu, F. X. Kärtner, and J. G. Fujimoto, "Comparative investigation of diode pumping for low-cost Cr<sup>3+</sup>:LiCAF lasers," Submitted to JOSA B.
50. R. Huber, D.C. Adler, V.J. Srinivasan, I. Gorczynska, and J.G. Fujimoto, "Fourier domain mode locking at 1050 nm for ultra-high-speed optical coherence tomography of the human retina at 236,000 axial scans per second," *Optics Letters* vol. 32, pp. 2049-2051, July 2007.
51. R. Huber, D. C. Adler, and J. G. Fujimoto, "Buffered Fourier Domain Mode Locking (FDML):Unidirectional swept laser sources for OCT imaging at 370,000 lines per second," *Optics Letters*, vol. 31, pp. 2975-2977, 2006.
52. U. Demirbas, A. Sennaroglu, A. Benedick, A. Siddiqui, F. X. Kartner, and J. G. Fujimoto, "Diode-pumped, high-average power femtosecond Cr<sup>3+</sup>:LiCAF laser," *Optics Letters*, vol. 32, pp. 3309-3311, 2007.
53. U. Demirbas, A. Sennaroglu, F. X. Kartner, and J. G. Fujimoto, "Highly efficient, low-cost femtosecond Cr<sup>3+</sup>:LiCAF laser pumped by single-mode diodes," *Optics Letters*, vol. 33, pp. 590-592, 2008.
54. A. M. Kowalewicz, V. Sharma, E. P. Ippen, J. G. Fujimoto, and K. Minoshima, "Three-dimensional photonic devices fabricated in glass by use of a femtosecond laser oscillator," *Optics Letters* vol. 30, pp.1060-2, 2005.
55. K. Suzuki, V. Sharma, J. G. Fujimoto, and E. P. Ippen, "Characterization of symmetric [3x3] directional couplers fabricated by direct writing with a femtosecond laser oscillator," *Optics Express*, vol. 14, pp. 2335-43, 2006.
56. R. Huber, D.C. Adler, V.J. Srinivasan, I. Gorczynska, and J.G. Fujimoto, "Fourier domain mode locking at 1050 nm for ultra-high-speed optical coherence tomography of the human retina at 236,000 axial scans per second," *Optics Letters* vol. 32, pp. 2049-2051, July 2007.
57. R. Huber, D. C. Adler, and J. G. Fujimoto, "Buffered Fourier Domain Mode Locking (FDML):Unidirectional swept laser sources for OCT imaging at 370,000 lines per second," *Optics Letters*, vol. 31, pp. 2975-2977, 2006.
58. U. Demirbas, A. Sennaroglu, A. Benedick, A. Siddiqui, F. X. Kartner, and J. G. Fujimoto, "Diode-pumped, high-average power femtosecond Cr<sup>3+</sup>:LiCAF laser," *Optics Letters*, vol. 32, pp. 3309-3311, 2007.
59. U. Demirbas, A. Sennaroglu, F. X. Kartner, and J. G. Fujimoto, "Highly efficient, low-cost femtosecond Cr<sup>3+</sup>:LiCAF laser pumped by single-mode diodes," *Optics Letters*, vol. 33, pp. 590-592, 2008.

60. A. M. Kowalewicz, V. Sharma, E. P. Ippen, J. G. Fujimoto, and K. Minoshima, "Three-dimensional photonic devices fabricated in glass by use of a femtosecond laser oscillator," *Optics Letters* vol. 30, pp.1060-2, 2005.
61. K. Suzuki, V. Sharma, J. G. Fujimoto, and E. P. Ippen, "Characterization of symmetric [3x3] directional couplers fabricated by direct writing with a femtosecond laser oscillator," *Optics Express*, vol. 14, pp. 2335-43, 2006.

### Conference Proceedings

1. H. Byun, J. Sickler, J. Morse, J. Chen, D. Pudo, E. P. Ippen, and F. X. Kärtner, "Femtosecond passively mode-locked fiber lasers using saturable Bragg reflectors", Paper THU11c.1, Ultrafast Phenomena Conference 2008, Stresa, Italy, Jun 2008
2. M. Y. Sander, H. M. Crespo, J. R. Birge, and F. X. Kärtner, "Modeling of Octave-Spanning sub-two-cycle Titanium:sapphire Lasers: Simulation and Experiment, Paper THU11c.8, *Ultrafast Phenomena Conference 2008*, Stresa, Italy, Jun 2008.
3. J. Kim and F. X. Kärtner, "Low-Drift and Low-Jitter Microwave Signal Synthesis from Mode-Locked Lasers," Paper B3L-C4, *IEEE International Frequency Control Symposium 2008*, Honolulu, HI, May 2008.
4. J. Kim, J. Cox, J. Chen, and F. X. Kärtner, "Optical and Microwave Timing Transfer and Synchronization Using Optical Pulse Trains," Paper B4P-D8, *IEEE International Frequency Control Symposium 2008*, Honolulu, HI, May 2008.
5. J. Kim, J. Chen, J. Cox and F. X. Kärtner, "Attosecond-Resolution Timing Jitter Characterization of Free-Running Mode-Locked Lasers," **(Invited)** Paper CF14, *Conference on Lasers and Electro Optics (CLEO) 2008*, San Jose, CA, May 2008.
6. J. Kim, M. Park, M. H. Perrott, and F. X. Kärtner, "7-ENOB Resolution Photonic Analog-to-Digital Conversion of Narrowband Microwave Signals at 40 GHz," Paper CM11, *Conference on Lasers and Electro Optics (CLEO) 2008*, San Jose, CA, May 2008.
7. J. Kim and F. X. Kärtner, "Microwave Signal Regeneration from Mode-Locked Lasers with  $1.9 \times 10^{-19}$  Stability," Paper CML4, *Conference on Lasers and Electro Optics (CLEO) 2008*, San Jose, CA, May 2008.
8. J. Kim, "Large-Scale, Long-Term Stable Femtosecond Timing Distribution and Synchronization," **(Invited)** Paper FTuL1, *OSA Annual Meeting 2007*, San Jose, CA, Sep 2007.
9. J. Kim, F. Ludwig, J. Chen, F. Loehl, F. Wong, H. Schlarb, and F. X. Kärtner, "Large-Scale, Long-Term Stable Femtosecond Timing Distribution and Synchronization Systems," Paper TuC3.2, *IEEE/LEOS Summer Topical Meeting on Optical Frequency and Time Measurement and Generation 2007*, Portland, OR, Jul 2007.
10. J. Moses, O. D. Mücke, A. Benedick, E. L. Falcão-Filho, S. Huang, K. H. Hong, A. M. Siddiqui, J. R. Birge, F. Ö. Ilday and F.X. Kärtner, "2-micron Optical Parametric Chirped Pulse Amplifier for Long-Wavelength Driven High Harmonic Generation," Paper CTuEE2, *Conference on Lasers and Electro Optics (CLEO) 2008*, San Jose, CA, May 2008.
11. J. R. Birge, H. M. Crespo, M. Sander, and F. X. Kärtner, "Non-Intrusive Sub-Two-Cycle Carrier-Envelope Stabilized Pulses Using Engineered Chirped Mirrors," paper CTuC3, *Conference on Lasers and Electro Optics (CLEO)*, San Jose, CA, May, 2008.
12. F. X. Kaertner and J. Birge, "Two-Dimensional Spectral Shearing Interferometry (2DSI) of Few-Cycle Laser Pulses," **(Invited)** Paper FThD4, *Frontiers in Optics, OSA Technical Digest (CD) (Optical Society of America, 2007)*,.
13. A. Benedick, J. Birge, R. Ell, O. D. Mucke, M. Sander and F. X. Kaertner, "Octave Spanning 1 GHz Ti:Sapphire Oscillator for HeNe CH4-based Frequency Combs and Clocks," **(Invited)**

- paper CF3-1-MON, *Conference on Lasers and Electro Optics Europe (CLEO/Europe)*, Munich, Germany, June 2007.
14. H. Choi, V. M. Gkortsas, F. X. Kärtner, L. Diehl, C. Y. Wang, F. Capasso, D. Bour, S. Corzine, J. Zhu, G. Höfler, and T. B. Norris, "Femtosecond Resonant Pulse Propagation in Quantum Cascade Lasers: Evidence of Coherent Effects", Paper CTuP7, *Conference on Lasers and Electro Optics (CLEO) 2008*, San Jose, CA, May 2008
  15. J. Chen, J. Sickler, E. Ippen, and F.X. Kaertner, "Low Timing-Jitter High Repetition-Rate Femtosecond Pulse Trains via Locking to External Fabry-Perot Cavities," *Conference on Lasers and Electro Optics (CLEO) 2008*, San Jose, CA, May 2008
  16. J. Chen, J. W. Sickler, H. Byun, E. P. Ippen, S. Jiang, and F. X. Kärtner, "Fundamentally Mode-locked 3 GHz Femtosecond Erbium Fiber Laser," paper THU4.4, *International Conference on Ultrafast Phenomena (UP) 2008*, Stresa, Lago Maggiore, Italy, June 2008.
  17. T. Barwicz, M.A. Popović, C.W. Holzwarth, M.R. Watts, P.T. Rakich, F. Gan, M. Dahlem, F.X. Kärtner, E.P. Ippen and H.I. Smith, "Challenges in nanofabrication of strong-confinement photonic devices", **(Invited)** presented at the *Fifty-Second International Conference on Electron, Ion, and Photon Beams and Nanolithography (EIPBN)*, Portland, Oregon, May 27-30, 2008.
  18. F.X. Kärtner, R. Amatya, M. Aranghini, H. Byun, J. Chen, M. Dahlem, N.A. DiLello, F. Gan, C.W. Holzwarth, J.L. Hoyt, E.P. Ippen, A. Khilo, J. Kim, A. Motamedi, J.S. Orcutt, M. Park, M. Perrott, M.A. Popović, R.J. Ram, H.I. Smith, G.R. Zhou, S.J. Spector, T.M. Lyszczarz, M.W. Geis, D.M. Lennon, J.U. Yoon, M.E. Grein and R.T. Schulein, "Photonic Analog-to-Digital Conversion with Electronic-Photonic Integrated Circuits," **(Invited)** *SPIE Photonics West*, San Jose, CA, Jan 19-24, 2008.
  19. M.A. Popović, T. Barwicz, M.S. Dahlem, F. Gan, C.W. Holzwarth, P.T. Rakich, M.R. Watts, H.I. Smith, E.P. Ippen and F.X. Kärtner, "Hitless-Reconfigurable and Bandwidth-Scalable Silicon Photonic Circuits for Telecom and Interconnect Applications," **(Invited)** Paper OTuF4, *Optical Fiber Communication Conference (OFC)*, Feb 26, 2008.
  20. T. Barwicz, M.A. Popović, F. Gan, M.S. Dahlem, C.W. Holzwarth, P.T. Rakich, E.P. Ippen, F.X. Kärtner and H.I. Smith, "Reconfigurable silicon photonic circuits for telecommunication applications," **(Invited)** presented at Photonics West LASE2008, San Jose, CA, Jan 19-24, 2008.
  21. T. Barwicz, M.A. Popović, M.R. Watts, P.T. Rakich, C.W. Holzwarth, F.X. Kärtner, E.P. Ippen and H.I. Smith, "Strategies for the successful realization of strong confinement microphotonic devices," **(Invited)** presented at Photonics West OPTO2008, San Jose, CA, Jan 19-24, 2008.
  22. M.A. Popović, T. Barwicz, M.R. Watts, P.T. Rakich, M.S. Dahlem, F. Gan, C.W. Holzwarth, L. Socci, H.I. Smith, F.X. Kärtner, E.P. Ippen and H.I. Smith, "Strong-confinement microring resonator photonic circuits," **(Invited)** Paper TuCC3, *20th Annual Meeting of the IEEE Lasers and Electro-Optics Society (LEOS)*, Lake Buena Vista, Florida, Oct 2007.
  23. P.T. Rakich and M.A. Popović, "Generalized Treatment of Optically Induced Forces and Potentials in Optomechanically Variable Photonic Circuits," Paper ITuC6, *OSA Topical Meeting on Integrated Photonics and Nanophotonics Research and Applications (IPNRA)*, Boston, MA, July 15, 2008.
  24. S.J. Spector, M.W. Geis, G.-R. Zhou, M.E. Grein, R.T. Schulein, F. Gan, M.A. Popović, J.U. Yoon, D.M. Lennon, E.P. Ippen, F.X. Kärtner and T.M. Lyszczarz, "CMOS-Compatible Wideband Silicon Modulator," Paper IMC3, *OSA Topical Meeting on Integrated Photonics and Nanophotonics Research and Applications (IPNRA)*, Boston, MA, July 15, 2008.
  25. M.A. Popović, T. Barwicz, P.T. Rakich, M.S. Dahlem, C.W. Holzwarth, F. Gan, L. Socci, M.R. Watts, H.I. Smith, F.X. Kärtner and E.P. Ippen, "Experimental demonstration of loop-

- coupled microring resonators for optimally sharp optical filters,” Paper CTuNN3, *Conference on Lasers and Electro-Optics (CLEO)*, San Jose, CA, May 4-9, 2008.
26. C.W. Holzwarth, J.S. Orcutt, H. Li, M.A. Popović, V.M. Stojanović, J.L. Hoyt, R.J. Ram and H.I. Smith, “Localized Substrate Removal Technique Enabling Strong-Confinement Microphotonics in Bulk Si CMOS Processes,” Paper CThKK5, *Conference on Lasers and Electro-Optics (CLEO)*, San Jose, CA, May 4-9, 2008.
  27. J.S. Orcutt, A. Khilo, M.A. Popović, C.W. Holzwarth, B. Moss, H. Li, M.S. Dahlem, T.D. Bonifield, F.X. Kärtner, E.P. Ippen, J.L. Hoyt, R.J. Ram and V. Stojanović, “Demonstration of an Electronic Photonic Integrated Circuit in a Commercial Scaled Bulk CMOS Process,” Paper CTuBB3, *Conference on Lasers and Electro-Optics (CLEO)*, San Jose, CA, May 4-9, 2008.
  28. P.T. Rakich, M.A. Popović, M. Soljačić and E.P. Ippen, “Self-aligning ‘smart’ microcavities and picometer-scale optomechanical control through optical forces and potentials,” paper JMD2, *Conference on Lasers and Electro-Optics (CLEO)*, San Jose, CA, May 4-9, 2008.
  29. M.A. Popović, E.P. Ippen and F.X. Kärtner, “Low-Loss Bloch Waves in Open Structures and Highly Compact, Efficient Si Waveguide-Crossing Arrays,” Paper MF5, *20th Annual Meeting of the IEEE Lasers and Electro-Optics Society (LEOS)*, Lake Buena Vista, Florida, Oct 2007.
  30. F. Gan, T. Barwicz, M.A. Popović, M.S. Dahlem, C.W. Holzwarth, P.T. Rakich, H.I. Smith, E.P. Ippen and F.X. Kärtner, “Maximizing the Thermo-Optic Tuning Range of Silicon Photonic Structures,” Paper TuB3.3, *IEEE/LEOS Photonics in Switching Conference*, San Francisco, CA, Aug 2007.
  31. M.A. Popović, T. Barwicz, M.S. Dahlem, F. Gan, C.W. Holzwarth, P.T. Rakich, H.I. Smith, E.P. Ippen and F.X. Kärtner, “Tunable, Fourth-Order Silicon Microring-Resonator Add-Drop Filters,” Paper 1.2.3, *European Conference on Optical Communication (ECOC)*, Berlin, Germany, Sep 2007.
  32. A. Khilo, M. A. Popović, F. X. Kärtner, “Efficient Planar Fiber-to-Chip Coupler based on Two-Stage Adiabatic Evolution,” Paper IO2/VIII-1, *International Conference on Coherent and Nonlinear Optics*, Minsk, Belarus, May 28-June 1, 2007
  33. A. Khilo, J. R. Birge, F. X. Kärtner, “Adaptive Error Compensation for Photonic Analog-to-Digital Converters,” Paper CMII4, *Conference on Lasers and Electro-Optics (CLEO)*, San Jose, CA, May 4-9, 2008.
  34. J. Chen, J. W. Sickler, T. Wilken, P. Fendel, R. Holzwarth, T. W. Hänsch, E. P. Ippen and F. X. Kärtner, “Generation of High Repetition Rate Femtosecond Pulse Trains with a High Finesse External Fabry-Perot Cavity,” *IEEE/LEOS Summer Topical Meeting on Optical Frequency and Time Measurement and Generation 2007*, Portland, OR, Jul 2007
  35. U. Demirbas, A. Sennaroglu, F. Kaertner, J. G. Fujimoto, “Highly efficient, low cost, diode-pumped femtosecond Cr:LiCAF lasers”, *XVI International Conference on Ultrafast Phenomena Topical Meeting and Tabletop Exhibit*, paper MON5I.2, Stresa, Italy, June 9-13, 2008.
  36. U. Demirbas, A. Sennaroglu, F. Kaertner, J. G. Fujimoto, “High power diode-pumped modelocked Cr:LiCAF laser”, *Conference on Lasers and Electro-Optics (CLEO)*, paper CFI2, San Jose, California, May 4-9, 2008.
  37. U. Demirbas, A. Sennaroglu, A. Benedick, A. Siddiqui, Fr. Kaertner, J. G. Fujimoto, “High average-power diode-pumped femtosecond Cr:LiCAF laser”, *Advanced Solid-State Photonics Topical Meeting*, paper MC38, *Optical Society of America*, Nara, Japan, January 27-30, 2008.
  38. J. H. Chung, Y. Gu, and J. G. Fujimoto, “Submicron-Period Waveguide Bragg Gratings Direct Written by an 800-nm Femtosecond Oscillator,” *Conference on Lasers and Electro-Optics*, Baltimore, MD, May 2007

39. J. H. Chung, Y. Gu, and J. G. Fujimoto, "Microbend Gratings Fabricated in Glass Substrates via Direct Writing with Near-Infrared Femtosecond Pulses," *Conference on Lasers and Electro-Optics*, Baltimore, MD, May 2007.
40. Y. Gu, J. H. Chung, and J. G. Fujimoto, "Femtosecond laser fabrication of directional couplers and Mach-Zehnder interferometers" *Conference on Lasers and Electro-Optics*, Baltimore, MD, May 2007.

### Theses

1. J. Kim, High-Precision Optical and Microwave Signal Synthesis and Distribution, Ph.D. Thesis, MIT, 2007.
2. J. Birge, A Preconditioned Newton-Krylov Method for Computing Steady-State Pulse Solutions of Mode-Locked Lasers, S.M. Thesis, MIT, 2008.
3. M. Popović, Theory and design of high-index-contrast microphotonic circuits, Ph.D. Thesis, Dept. of Electrical Engineering and Computer Science, MIT, 2008.
4. A. Khilo, Integrated Optical Analog-to-Digital Converter, S.M. Thesis, MIT, 2008.
5. M. Araghchini, Design and Fabrication of Efficient Fiber to Chip Couplers, S.M. Thesis, MIT, 2008.